ADVANCED STEEL CONSTRUCTION

An International Journal

Volume 2 Number 3

September 2006

CONTENTS

Technical Papers

ISSN 1816-112X

Website: *http://www.hkisc.org/*

ADVANCED STEEL CONSTRUCTION

VOL.2, NO.3 (2006)

ADVANCED STEEL CONSTRUCTION

an International Journal

ISSN 1816-112X

Volume 2 Number 3 *September 2006*

ISSN 1816-112X

Advanced Steel Construction
an international journal

General Information
Advanced Steel Construction, an international journal

Aims and scope

The International Journal of Advanced Steel Construction provides a platform for the publication and rapid dissemination of original and up-to-date research and technological developments in steel construction, design and analysis. Scope of research papers published in this journal includes but is not limited to theoretical and experimental research on elements, assemblages, systems, material, design philosophy and codification, standards, fabrication, projects of innovative nature and computer techniques. The journal is specifically tailored to channel the exchange of technological know-how between researchers and practitioners. Contributions from all aspects related to the recent developments of advanced steel construction are welcome.

Instructions to authors

Submission of the manuscript. Authors may submit three double-spaced hard copies of manuscripts together with an electronic copy on a diskette or cd-rom in an editable format (MS Word is preferred). Manuscripts should be submitted to the regional editors as follows for arrangement of review.

Asian Pacific , African and organizing editor :	Professor S.L. Chan
American editor :	Professor W.F. Chen
European editor :	Professor R. Zandonini

All manuscripts submitted to the journal are highly recommended to accompany with a list of four potential reviewers suggested by the author(s). This list should include the complete name, address, telephone and fax numbers, email address, and at least five keywords that identify the expertise of each reviewer. This scheme will improve the process of review.

Style of manuscript

General. Author(s) should provide full postal and email addresses and fax number for correspondence. The manuscript including abstract, keywords, references, figures and tables should be in English with pages numbered and typed with double line spacing on single side of A4 or letter-sized paper. The front page of the article should contain:

a) a short title (reflecting the content of the paper);
b) all the name(s) and postal and email addresses of author(s) specifying the author to whom correspondence and proofs should be sent;
c) an abstract of 100-200 words; and
d) 5 to 8 keywords.

The paper must contain an introduction and a conclusion. The length of paper should not exceed 25 journal pages (approximately 15,000 words equivalents).

Tables and figures. Tables and figures including photographs should be typed, numbered consecutively in Arabic numerals and with short titles. They should be referred in the text as Figure 1, Table 2, etc. Originally drawn figures and photographs should be provided in a form suitable for photographic reproduction and reduction in the journal.

Mathematical expressions and units. The Systeme Internationale (SI) should be followed whenever possible. The numbers identifying the displayed mathematical expression should be referred to in the text as Eq. (1), Eq. (2).

References. References to published literature should be referred in the text, in the order of citation with Arabic numerals, by the last name(s) of the author(s) (e.g. Zandonini, R.). References should be in English with occasional allowance of 1-2 exceptional references in local languages and reflect the current state-of-technology. Journal titles should be abbreviated in the style of the Word List of Scientific Periodicals. References should be cited in the following style.

Journal: Chen, W.F. and Kishi, N., “Semi-rigid steel beam-to-column connections, data base and modeling”, Journal of Structural Engineering, ASCE, 1989, 115(1), pp.105-119.

Book: Chan, S.L. and Chui, P.P.T., "Non-linear static and cyclic analysis of semi-rigid steel frames", Elsevier Science, 2000, pp.336.

Proceedings: Zandonini, R. and Zanon, P., “Experimental analysis of steel beams with semi-rigid joints”, Proceedings of International Conference on Advances in Steel Structures, Hong Kong, 1996, vol. 1, pp.356-364.

Proofs. Proof will be sent to the corresponding author to correct any typesetting errors. Alternations to the original manuscript at this stage will not be accepted. Proofs should be returned within 48 hours of receipt by Express Mail, Fax or Email.

Copyright. Submission of an article to “Advanced Steel Construction” implies that it presents the original and unpublished work, and not under consideration for publication nor published elsewhere. On acceptance of a manuscript submitted, the copyright thereof is transferred to the publisher by the Transfer of Copyright Agreement and upon the acceptance of publication for the papers, the corresponding author must sign the form for Transfer of Copyright.

Permission. Quoting from this journal is granted provided that the customary acknowledgement is given to the source.

Page charge and Reprints. There will be no page charges if the length of paper is within the limit of 25 journal pages. A total of 30 free offprints will be supplied free of charge to the corresponding author. Purchasing orders for additional offprints can be made on order forms which will be sent to the authors. These instructions can be obtained at the Hong Kong Institute of Steel Construction, Journal website: http://www.hkisc.org

The International Journal of Advanced Steel Construction is published quarterly by non-profit making learnt society, The Hong Kong Institute of Steel Construction, c/o Department of Civil & Structural Engineering, The Hong Kong Polytechnic University, Hung Hom, Kowloon, Hong Kong.

Subscription inquiries and change of address. Address all subscription inquiries and correspondence to Member Records, IJASC. Notify an address change as soon as possible. All communications should include both old and new addresses with zip codes and be accompanied by a mailing label from a recent issue. Allow six weeks for all changes to become effective.

The Hong Kong Institute of Steel Construction
HKISC
c/o Department of Civil and Structural Engineering,
The Hong Kong Polytechnic University,
Hunghom, Kowloon, Hong Kong, China.
Tel: 852- 2766 6047 Fax: 852- 2334 6389
Email: *ceslchan@polyu.edu.hk* Website: *http://www.hkisc.org/*
ISSN 1816-112X

ISSN 1816-112X

Advanced Steel Construction
an international journal

VOLUME 2 NUMBER 3 SEPTEMBER 2006

Technical Papers

BOND FAILURE INVESTIGATION OF CFRP-STEEL ADHESIVE JOINTS

S. P. Chiew*, S. T. Lie, C. K. Lee and Y. Yu

School of Civil and Environmental Engineering
Nanyang Technological University, Singapore
**(Email: cspchiew@ntu.edu.sg Fax: +65- 6792 1650)*

ABSTRACT: To strengthen deteriorated steel structures, bonding carbon fiber reinforced polymer laminate externally to the steel surface is a promising method. For CFRP-strengthened steel structures, the bond performance between CFRP laminate and steel is a crucial consideration, which will directly influence strengthening effect and determine the final capacity of the strengthened structures. To investigate the bond failure mechanism of CFRP-bonded steel structures, tests for different types of CFRP-steel adhesive joints have to be conducted first. Besides the experimental studies, finite element analyses for the different types of joints are carried out to study in detail the stress and strain distributions along the bondline. It is found that for all joints with different geometries and loading conditions, the most important factors that influence the final bond failure are their peel and in-plane shear stress/strain components. Based on the test results and the finite element analyses, a bond failure model is proposed. With this bond failure model, the failure loads for the different joints can be predicted reasonably well compared to the experimental measurements.

Keywords: Carbon fiber reinforced polymer, adhesive joint and bond failure

1. INTRODUCTION

As an advanced composite material, carbon fiber reinforced polymer (CFRP) has been widely used to strengthen and repair structural concrete elements for years. The desirable characteristics of CFRP such as: high strength, high tensile modulus, light weight, installation facility and resistance to corrosion have all played a very significant role in creating this greater interest for structural repair and strengthening applications. In recent years, it has been found by some researchers that besides strengthening concrete structures, CFRP laminates can also be used to strengthen existing steel structures by external bonding (Miller et al [1], Tavakkolizadeh and Saadatmanesh [2], Jiao and Zhao [3]).

For CFRP-bonded steel structures, a very important concern is the potential bond failure between the CFRP laminate and steel surface. According to the past research results about structural bonded joints (Tong and Steven [4]), the dominant failure mode for composite-bonded metal joint is adhesive failure rather than adherend failure, which is totally different from the “rip-off” failure mode for CFRP-bonded concrete structures. For the later, the strength of the bond between CFRP laminate and concrete surface is generally larger than the failure strength of concrete. Therefore, in the rip-off failure the surface concrete comes off with CFRP. However, for CFRP-bonded steel structures, the failure strengths of steel and CFRP are both very large compared to that of the adhesive bond. Due to material discontinuity at the location of bond end or crack tip, the stress concentration in these areas may cause adhesive failure before steel and CFRP achieve their ultimate strengths. For this reason, the CFRP-steel bond property needs to be studied carefully. In recent years, some researchers have started to focus on this important issue through both experimental and theoretical investigations (Ono et al [5], El Damatty and Abushagur [6]).

Unfortunately, there is still no failure model for CFRP-bonded steel structures which can be used reliably with respect to different geometries and loading conditions.

In this current study, tests for different CFRP-steel adhesive joints are performed. Besides the experimental investigation, the finite element analysis (FEA) is conducted to explore the stress and strain distributions along the bondline. Through analyses of the numerical results of CFRP-steel adhesive joints with different geometries and loading conditions, a bond failure model composed of strain and strain energy components is proposed. The failure loads for the tested joints are well predicted by the proposed bond failure model.

2. EXPERIMENTAL INVESTIGATION

A total of four types of CFRP-steel adhesive joints with different geometries were constructed and tested under monotonic loading to investigate the bond failure behaviours.

2.1 Material Properties

The CFRP laminate used in the experiment is TYFO SCH-41S. This is a commonly used carbon fiber composite material composed of unidirectional carbon fibers with Aramid cross fibers. The adhesive material is TYFO-S saturant epoxy which is a two-component epoxy. The steel type is low carbon S275. The mechanical properties of carbon fiber and laminate are shown in Table 1. The mechanical properties of steel and epoxy are listed in Table 2 and Table 3, respectively.

Table 1. Material Properties of Carbon Fiber and Laminate

Material	Tensile Strength (N/mm^2)	Tensile Modulus (kN/mm^2)	Poisson's Ratio	Elongation (%)	Laminate Thickness (mm)
Carbon Fiber	3790	230.0	0.29	1.7	-
Laminate	876	72.4	0.31	1.2	1

Table 2. Material Properties of Epoxy

Yield Stress (N/mm^2)	Young's Modulus (kN/mm^2)	Elongation Percent	Poisson's Ratio
72.4	3.18	5%	0.35

Table 3. Material Properties of Steel

Yield Stress (N/mm^2)	Young's Modulus (kN/mm^2)	Ultimate Stress (N/mm^2)	Poisson's Ratio
280	200	420	0.3

2.2 Test Specimen

To obtain the bond strength of joints under different loading conditions, the following specimens are designed as: (a) Double-lap joint, (b) Single-lap joint, (c) T-peel joint and (d) Tubular joint. The configurations of the four types of joint specimens are illustrated in Figure 1. To investigate the bond strength under shear dominant loading case, double-lap joint specimens are employed as well as tubular joints. T-peel and single-lap joint specimens are respectively employed to investigate peel and mixed loading effects, respectively. The dimensions of the specimens mentioned above are

shown in Table 4. The four types of joints are abbreviated to: DL (double-lap), SL (single-lap), TP (T-peel) and TB (tubular). For each type of joints, Arabic numerals are used to indicate the sub-types (joints with same configurations but different dimensions). The thickness of adhesive layer is around a constant value of 0.15mm for all the joints.

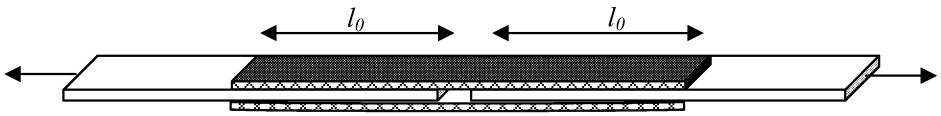

(a) Double-lap joint

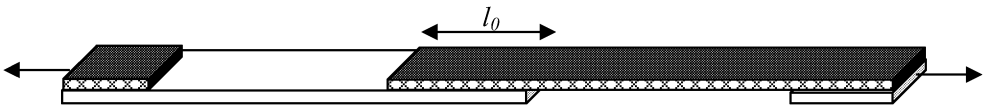

(b) Single-lap joint

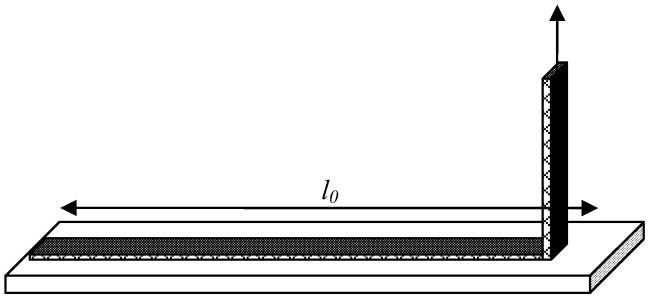

(c) T-peel joint

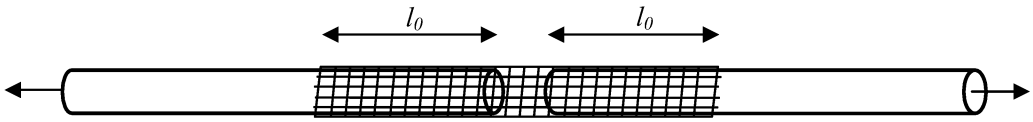

(d) Tubular joint

Figure 1. Joint specimen configurations

Table 4. Specimen Dimensions and Average Failure Loads of Bond Tests

Specimen Type	Number of Specimens	Thickness of Steel Adherend (mm)	Bond Length (mm)	Bond Width (mm)	Average Failure Load (kN)
DL1	3	2.0	12.7	25.4	3.9
DL2	1	2.0	50.8	50.8	22.5
DL3	1	2.0	100.0	50.8	27.5
DL4	1	2.0	150.0	50.8	27.8
DL5	1	2.0	200.0	50.8	25.8
SL1	3	2.0	25.4	25.4	3.1
SL2	1	2.0	50.8	50.8	4.2
TP1	3	6.0	100.0	25.4	0.2
TP2	3	6.0	100.0	50.8	0.4
TB1	3	2.2	200.0	188.4	77.4
TB2	2	2.2	400.0	188.4	92.6

2.3 Specimen Preparation

To guarantee the bond quality, the steel plates are manually grinded with sand paper and the steel tubes are treated with sand blast. This process is to make the steel surface free of protrusions or cavities, which may cause voids in the bondline. Before bonding the CFRP laminates, steel surfaces are cleaned with acetone. The epoxy is mixed of 100 parts of component A and 42 parts of component B by volume. While the CFRP laminates being bonded, they are carefully pressed with special rollers to ensure that there is no air hump remained. After the laminates are adhered, no extra pressure is exerted during curing. The extra epoxy are cut off carefully and removed from the specimens after a curing period of 72 hours. For tubular specimens, a steel solid bar is welded on each end of the tube for clamping purpose.

For each double and single plate joint, two strain gauges are placed on the steel and CFRP adherend respectively to monitor the strain increment in the loading process. For the 200mm tubular joint, nine strain gauges are placed on the CFRP adherend to investigate the strain variation along the axial direction. The positions of the strain gauges are illustrated in Figure 2.

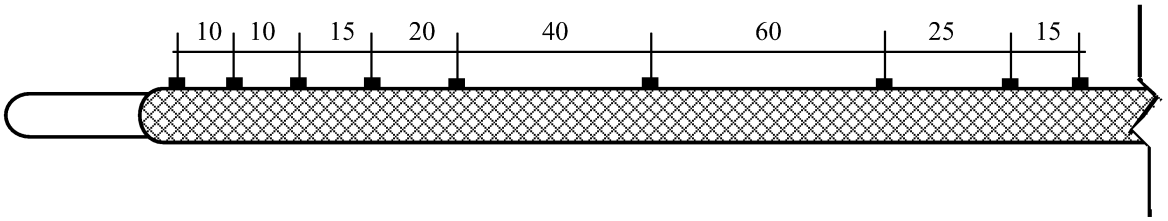

Figure 2. Illustration of the positions of strain gauges on CFRP laminate (unit: mm)

2.4 Test Procedure and Results

Two types of universal testing machines are used as loading equipment. For double-lap, single-lap and T-peel joints, the Instron 5500 universal electro-mechanical testing system is used. The loading speed for these specimens is 0.01mm/s. For tubular joints, the Instron 5590 universal hydraulic testing system is employed to satisfy the requirement of larger dimensions and higher forces. A loading speed of 0.02mm/s is employed. As expected, the failure mode of all the specimens is adhesive bond failure. The CFRP and steel adherends separate under failure load without damage in

the CFRP laminate. The pictures of intact and damaged typical specimens are shown in Figure 3. The average failure load of each type of specimen is listed in Table 4.

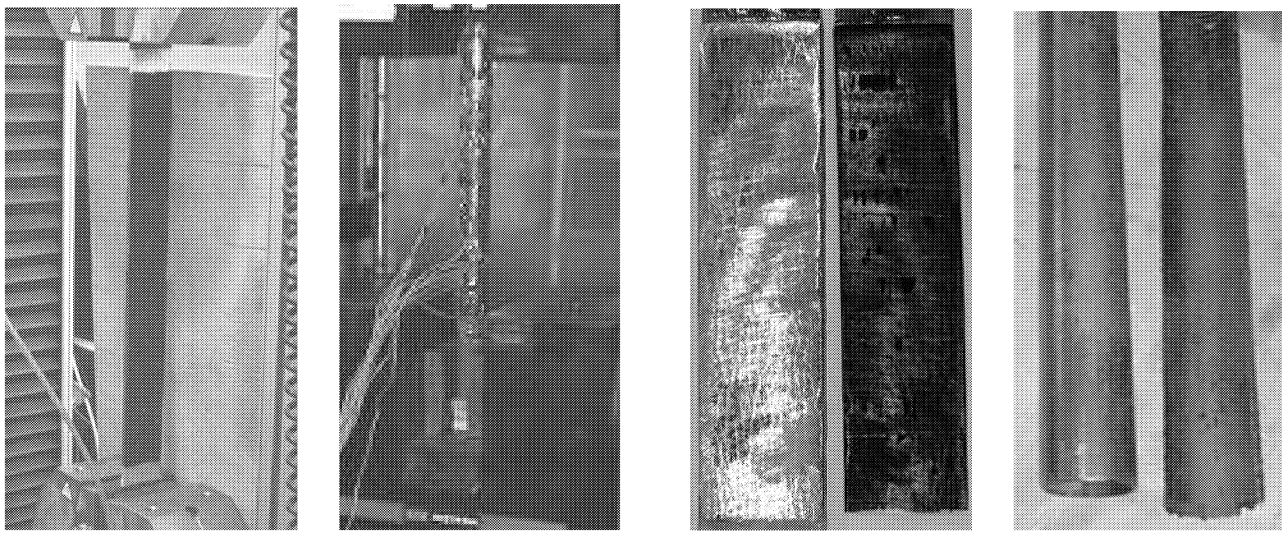

(a) Before failure (b) After failure

Figure 3. Typical specimens before and after failure

For the joints under in-plane loading, i.e. double-lap and tubular joints, the bond strengths are not proportional to the bond lengths. For double-lap joint specimens, the strength in unit length is defined as,

$$S = P/(2b) \tag{1}$$

where P is the ultimate load for the specimen and b is the plate width. For tubular joints, the strength in unit length is defined as following,

$$S = P/(2\pi R) \tag{2}$$

The bond strength varying trend is shown in Figure 4. The longer the bond length is, the more slowly the bond strength increases. When the bond length is large enough, the strength increase with the rising length tends to be unnoticeable. This phenomenon is quite similar with what exists in the adhesively bonded metal joints (Sheppard et al [7]).

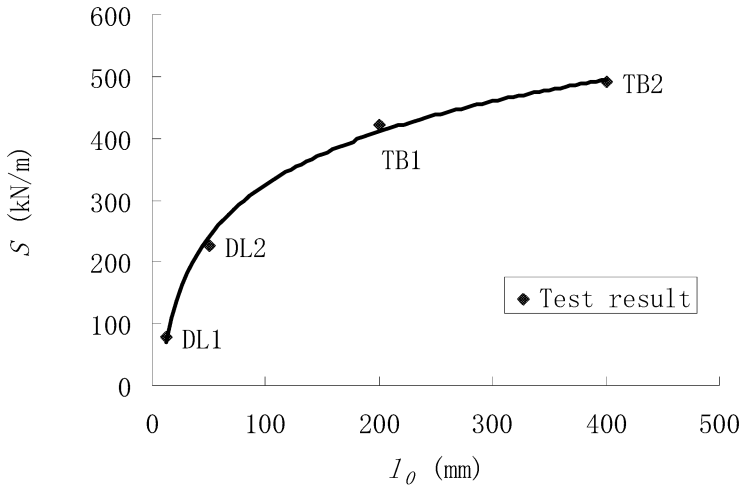

Figure 4. Relationship between bond strength and bond length

In Figure 5 the strain distribution in the CFRP laminate is shown. L is the distance from the end of the laminate. It can be seen in the major part of the CFRP laminate the strain distributes evenly, while at the CFRP and steel ends the strain varies sharply, especially at the later one. Because the cross-section magnitude of stiffness of the internal steel tube is larger than that of the CFRP laminate, more loads is shared by steel than CFRP in the middle region where CFRP and steel bear together. At the end of the steel tube, load transferred into CFRP laminate is much more than that at the CFRP end, so the stress/strain in the CFRP laminate increases even faster.

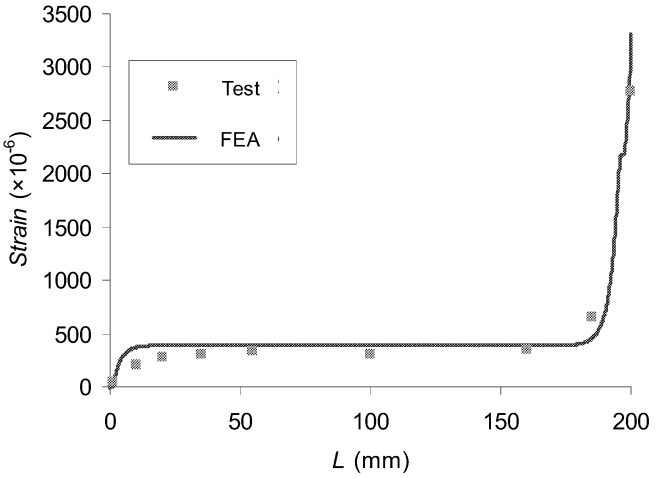

Figure 5. Strain distribution along the CFRP laminate for TB1

3. NUMERICAL ANALYSIS

3.1 Finite Element Modelling Technique

To analyze the adhesively bonded joints tested above, the FE software package ABAQUS (Version 6.4-1) is used in this study. Isoparametric, three-node and four-node plane strain elements are employed to model the joints. Material nonlinearity is also incorporated in the analysis to simulate the constitutive relationship of the adhesive and the steel adherend. The Von Mises yield criterion is used for both adhesive layer and steel adherend.

Both the adherends and the adhesive are modelled as separate parts and linked together. A pairs of nodes at each identical location exists at the material interfaces, one belonging to the adherend, the other to the adhesive. All degrees of freedom of the corresponding nodes are constrained to identical displacements. This approach is necessary to obtain accurate stress and failure ratio results at the interface, i.e. to obtain stress jumps at the interface due to the stiffness jumps between the different materials. Also, it is important to take the geometric nonlinearity into account. The relative displacement between CFRP and steel adherend changes the stress distributions in adherends and adhesive under loading. Hence, the stress distributions under at small loads often differ considerably from the distributions at high loads.

In the FE analysis of FPR-steel joints, what are of most concern are the stress and strain distributions in the adhesive layer, because the failure mode of the joints is adhesive failure. The adhesive layer is very thin compared with the thickness of the adherends but, to achieve reliable results, it is necessary to use fine mesh for the adhesive and the regions in the adherends close to the adhesive. Other further regions, such as the adherends outside the joint overlap, can be

modelled with a coarser mesh. On the other hand, too fine mesh may lead to rather high number of degrees of freedom, which is time-consuming and it further complicates the pre- and post-processing of the analysis. With reference to Sheppard et al. [7], the adhesive layer should be meshed in the dimension of adhesive thickness, and the consequent FE analysis results would be quite good. Accordingly, one layer of elements is used for the adhesive; and four to seven layers of elements are employed for the adherends.

3.2 Stress/Strain Distribution

In CFRP-retrofitted structures, the most significant role the adhesive play is stress transition. Generally, when the original structure is retrofitted by CFRP, the external loads do not exert on the laminates directly. The load in the longitudinal direction in CFRP comes from the original structure by the stress transfer through the adhesive layer. In this process the adhesive layer undergoes a large shearing deformation. Therefore, the shearing stress and strain distributions in adhesive should be given much attention. Hart-Smith [8] discussed that only for very short overlap test coupons is the strength a function of the bond area. For long overlap bonded joints the strength is uniform, with the great majority of the load carried by the plastic adhesive zones separated by the lightly loaded elastic trough. The width of these plastic zones is constant regardless of the overlap. However, if one of the adherends had been less stiff than the other, the load transfer would not have been balanced and the adhesive could be critically strained at one end (from which the softer adherend extended) before a significant load transfer had developed at the other end.

To illustrate the point discussed above, the shearing stress in the adhesive layer and the tension stress in the midline of steel and CFRP are plotted in Figure 6. In the graph, x is the normalized distance from the end of the CFRP laminate. It can be seen that from left to right, the stress in steel drops from maximum value to zero. To keep the section load balanced, the stress in CFRP increases so that the load transfers gradually from steel to CFRP laminate. The major part of load transfer happens in the area near the joint ends, while in the middle section of the joint the stresses are stably distributed according to the stiffness of steel and CFRP. Therefore, the value of shearing stress in the adhesive end is very large as a result of stress transfer between steel and CFRP. In the middle section where the stresses in steel and CFRP are more stable, the shearing stress in adhesive is close to zero.

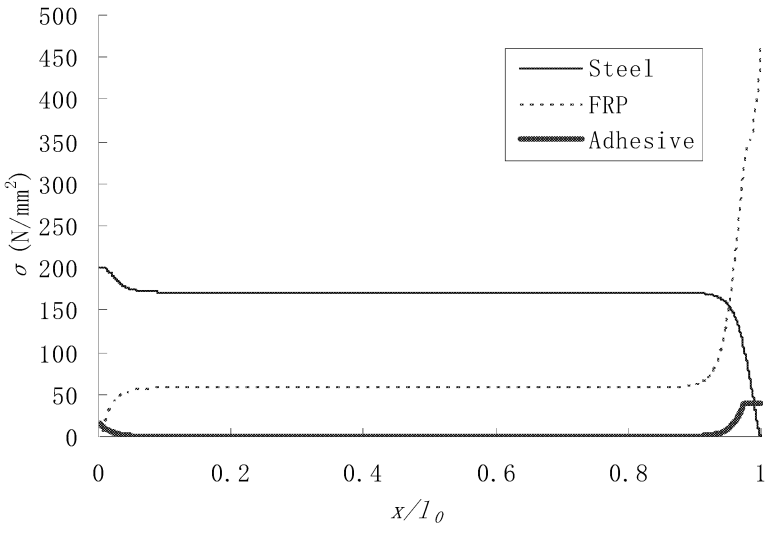

Figure 6. Stress distributions in adherends and adhesive for TB1

Based on the FE analysis of double-lap and tubular joints with different bond lengths, the shearing stress distributions in the adhesive layers are shown in Figure 7. It can be seen that for the joint with relatively short bond length, the maximum stress in the joint end does not reach the maximum shearing stress of the adhesive at the moment the joint fails, and the stress in the middle section of the joint is of high value. With increasing bond length, the stress in the joint end goes up. For the joint with 200mm bond length, the maximum shearing stress has been attained in the joint end before the joint fails. The stress in the middle section keeps relatively low value till the joint fails. This is similar to the stress distribution of conventional symmetric double-lap metal joints. Compared to the conventional symmetric double-lap metal joints, an essential difference of the CFRP-steel joint is that the stress values are not equal in each end of the joint. It is shown that the stress value at the left end of the joint is two more times less than that at the right. This phenomenon is caused by the stiffness difference between the upper and lower adherends. Since the CFRP laminate is less stiff than steel, the stress at the joint end where the steel adherend terminates is much higher than the stress at the other end. Therefore, the bond failure initiates from the end where the steel adherend terminates. This conclusion agrees with the test observation.

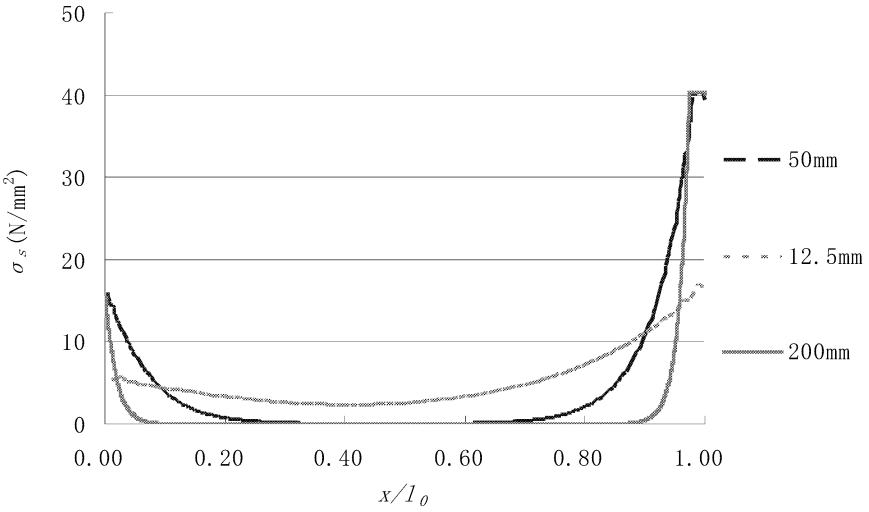

Figure 7. Comparison of stress distributions along the bondlines

In the adhesive layer, the normal stress and strain at the joint ends are not negligible. Generally the magnitude of peel stress and strain is much less than that of relevant shearing components for in-plane loaded joints. However, for adhesive materials, the volume deformation capacity is not as good as shape deformation capacity, which means the normal strain to cause the adhesive failure could be much smaller compared to the shearing strain.

Generally, the failure of adhesive joints always initiate from the joint end no matter what the joint geometry is. By FE analysis of different joints, the typical shearing and normal strain distributions in the double-lap, single-lap and T-peel joints are illustrated in Figures 8 to 10. It is clear that both shearing and normal strains in the adhesive layer have prominent high values at the joint ends. Also, it can be seen that the adhesive failure of all the joints is the result of the synergetic effect of shearing and normal stresses.

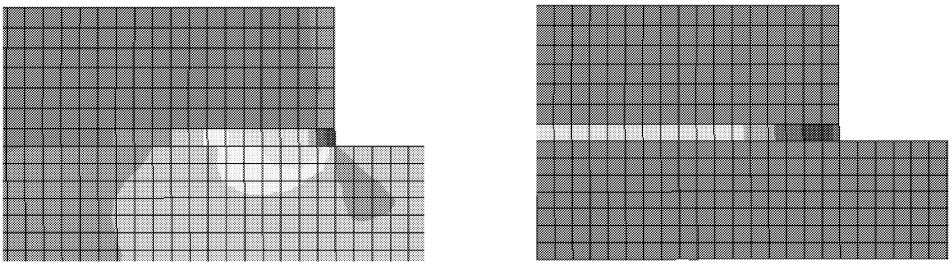

(a) Normal strain (b) Shear strain

Figure 8. Normal and shear strain at the end of typical double-lap or tubular joint

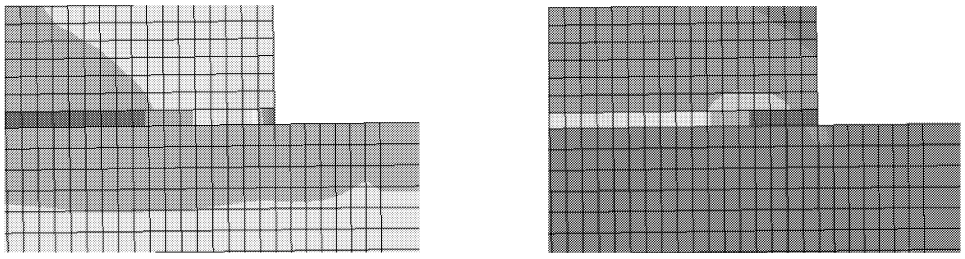

(a) Normal strain (b) Shear strain

Figure 9. Normal and shear strain at the end of single-lap joint

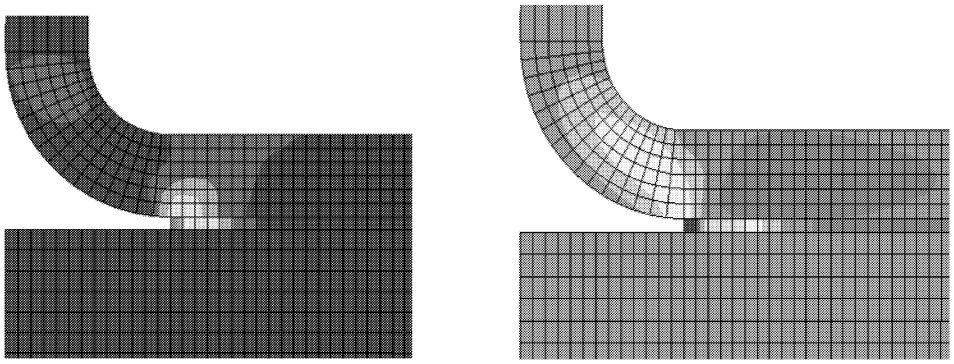

(a) Normal strain (b) Shear strain

Figure 10. Normal strain and shear strain at the end of peel joint

4. BOND FAILURE MODEL

4.1 Stress Investigation

The possibility of employing stress components as failure criterion is studied first. Based on the stress analysis of all the tested joints, different stress components such as shear, normal, deviatoric and hydrostatic stress have been analyzed. In Figure 11, the deviatoric and hydrostatic stress components for the joints are plotted. It is found that, for the joints with different bond lengths or geometries, the adhesives at the joint ends may have very close stress values, while the strains are quite different. This is mainly because the epoxy used in this study is a not an elastic material. Therefore, the stress components are not sensitive enough to be used as the failure indices.

Further more, it was observed by Lee and Kong [9] that the maximum principle stress zone

criterion proposed by Clark and McGregor [10] was not satisfied in the case of adhesively bonded joints composed of dissimilar adherend materials. Due to these reasons, the stress components are not suitable for failure criterion construction.

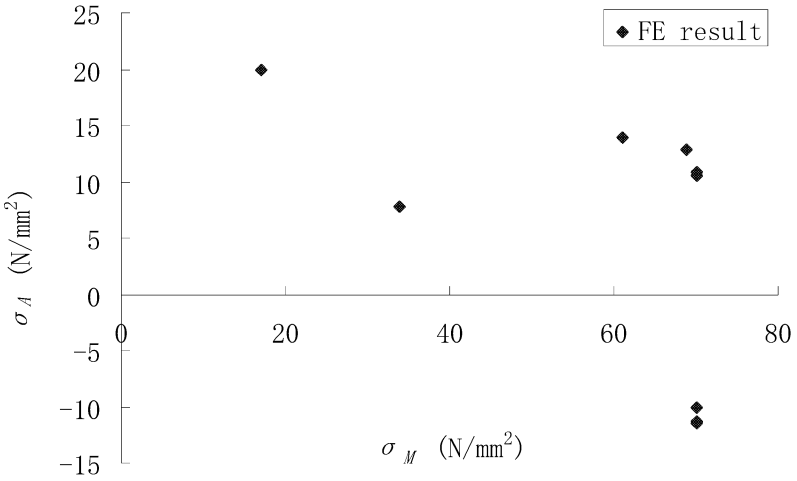

Figure 11. Relationship between deviatoric and hydrostatic stress components

4.2 Strain Investigation

As far as strain components are studied, in-plane shear and normal strain tensors are of most concern since they play a dominant role in adhesive failure mechanism. Based on the experimental and numerical results, the relationship between normal strain and shear strain at failure load of each type of specimen can be obtained. In the region where normal strain is negative, there tends to be a linear relationship between these components as shown in Figure 12.

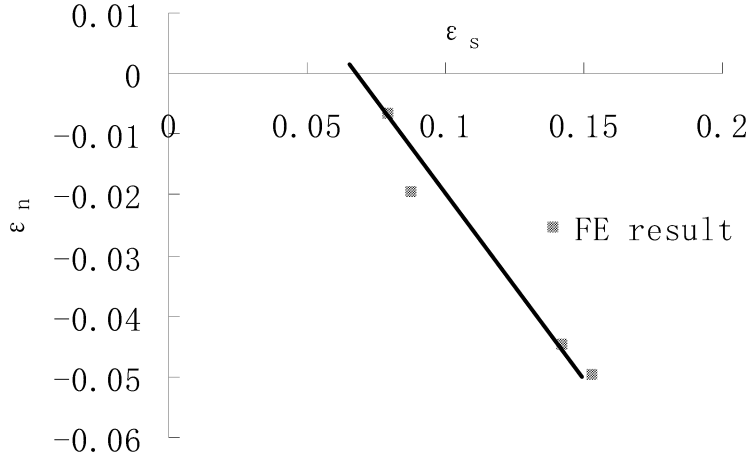

Figure 12. Linear relationship between negative normal and shear strain

This linear tendency is quite similar to the conclusion of Oh et al [11]. In their study, in the region where normal stress is negative, a linear relationship of normal and shearing components is proposed based on the experimental result. Consequently, it is reasonable to employ a linear equation with respect to normal strain and shear strains as the failure criterion in the region with negative normal strain. Therefore, the adhesive failure model in the region with negative normal strain can be proposed as,

$$\frac{\varepsilon_s}{\varepsilon_{sc}} + \frac{\varepsilon_n}{\varepsilon_{nc}} = 1 \tag{3}$$

where ε_n is normal strain, ε_s is shear strain, and ε_{sc} and ε_{nc} are the critical value of shear and normal strain, respectively. From Figure 5, their values are derived as 0.07 and 0.05.

4.3 Strain Energy Density Investigation

For the specimens in which the peel components play a relatively dominant role in the adhesive failure process, the linear equation of normal and shearing strain is not suitable any more. According to Tong and Steven [4], the mixed-mode failure criterion for solid fracture can be expressed in a linear equation with respect to energy release rates, which is a quadratic variable with respect to stress or strain. Therefore, in this study, a quadratic variable about strain is then taken into consideration, which is strain energy density. The general expression of strain energy density is,

$$w = \int_0^{\varepsilon_{ij}} \sigma_{ij} d\varepsilon_{ij} \tag{4}$$

where σ_{ij} and ε_{ij} are stress and strain tensors, respectively. In this study, the relationship between shear strain energy and peel strain energy of the peel strain involved specimens is shown in Figure 13.

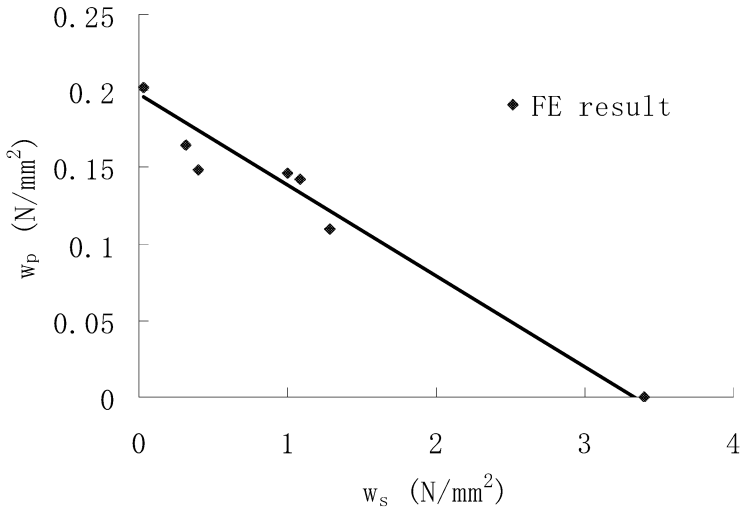

Figure 13. Linear relationship between peel and shear strain energy density

It is clear that the relationship of these two variables can be approximately formulated by a linear equation. So, when the normal strain is positive, the adhesive failure model is proposed as

$$\frac{w_s}{w_{sc}} + \frac{w_p}{w_{pc}} = 1 \tag{5}$$

where w_{sc} is the critical shear energy density, and w_{pc} is the critical peel energy density. The shear strain energy density is defined as

$$w_s = \int_0^{\varepsilon_s} \sigma_s d\varepsilon_s \tag{6}$$

where σ_s is shear stress. Similarly, the peel strain energy is defined as follow:

$$w_p = \int_0^{\varepsilon_p} \sigma_p d\varepsilon_p \tag{7}$$

where σ_p is peel stress, and ε_p is peel strain. The value of the critical shear strain energy density is deduced as 3.55 and for peel strain energy density that value is 0.2.

4.4 Failure Prediction for CFRP-Steel Joints

With the adhesive failure criterion proposed above, the failure loads of the tested specimens are predicted by the FE analysis. Failure is to occur in each joint when the adhesive shearing and normal strain index reaches the critical value or when the strain energy density criterion is satisfied. Table 5 shows the failure load comparison of experimental and numerical results for each type of the CFRP-steel adhesive joints. It is argued that due to the wide range of bonded joint types, the accuracy of the failure predictions is reasonably good.

Table 5. Comparison of Experimental and Numerical Bond Strengths

Model	Failure Load from Test P_{av} (kN)	Failure Load from FEA P_n (kN)	Load Difference ΔP (kN)	Comparative Load Difference $\lvert\Delta P\rvert / P_{av}$
DL1	3.9	3.9	0.0	0.00
DL2	22.5	25.3	2.8	0.12
DL3	27.5	27.5	0	0.00
DL4	27.8	27.5	-0.3	0.01
DL5	25.8	27.5	1.7	0.07
SL1	3.1	3.5	0.4	0.13
SL2	4.2	5.1	0.9	0.21
TP1	0.2	0.2	0.0	0.00
TP2	0.4	0.4	0.0	0.00
TB1	77.4	78.4	1.0	0.01
TB2	92.6	85.8	-6.8	0.07

5. CONCLUSION AND FUTURE WORK

For CFRP-steel adhesive joints, debonding failure is a very important consideration. Bond failure between CFRP laminate and steel surface is the only failure mode for the four types of joints discussed in this paper. For joint with bondline parallel to the loading direction, the bond failure load increases with the bond length. The longer the bond length, the smaller is this increment. When the bond length reaches a certain value, the strength increment tends to be insignificant with correspondingly increasing bond length. As a result of the high stress/strain concentration, debonding failure for all joints initiates from the end of bondline.

A bond failure model composed of strain and strain energy criteria is proposed for the CFRP-steel adhesively bonded joints. When this bond failure model is incorporated in the numerical analysis, the bond failure loads for the different CFRP-steel adhesive joints can be predicted. The numerical prediction for the bond failure loads agree reasonably well with the experimental measurements.

REFERENCES

[1] Miller T.C., Chajes M.J., Mertz D.R. and Hastings J.N., "Strengthening of a steel bridge girder using CFRP plates", Journal of Bridge Engineering, ASCE, 2001, 6(6), pp. 514-522.

[2] Tavakkolizadeh M. and Saadatmanesh H., "Fatigue strength of steel girders strengthened with carbon fiber reinforced polymer patch", Journal of Structural Engineering, ASCE, 2003, 129(2), pp. 186–196.

[3] Jiao, H. and Zhao, X. L., "CFRP strengthened butt-welded very high strength (VHS) circular steel tubes", Thin-Walled Structures, 2004, 42(7), pp. 963-978.

[4] Tong L. and Steven G.P., "Analysis and Design of Structural Bonded Joints", Kluwer Academic, Boston, USA, 1999.

[5] Ono K., Sugiura K., Sasaki A., Wakahara N. and Komaki H., "Bond characteristics of carbon fiber reinforced plastics to structural steels", High Performance Materials in Bridges: Proceedings of the International Conference, Kona, Hawaii, 2001, pp. 34-43.

[6] El Damatty A.A. and Abushagur M., "Testing and modeling of shear and peel behavior for bonded steel/CFRP connections", Thin-Walled Structures, 2003, 41(11), pp. 987–1003.

[7] Sheppard A., Kelly D. and Tong L., "A damage zone model for the failure analysis of adhesively bonded joints", International Journal of Adhesion & Adhesives, 1998, 18(6), pp. 385–400.

[8] Hart-Smith, L. J., "Adhesive bond of aircraft primary structures", High-Performance Adhesive Bond, Dearborn, Michigan, USA, 1980, pp. 1-17.

[9] Lee, K.Y. and Kong, B.S., "Theoretical and experimental studies for the failure criterion of adhesively bonded joints", Journal of Adhesion Science and Technology, 2000, 14(6), pp. 817-832.

[10] Clarke J.D. and McGregor I.J., "Ultimate tensile stress over a zone: a new failure criterion for adhesive joints", Journal of Adhesion, 1993, 42(3), pp. 227-245.

[11] Oh, B. H., Cho, J. Y. and Park, D. G., "Failure behaviour and separation criterion for strengthened concrete members with steel plates", Journal of Structural Engineering, ASCE, 2003, 129(9), pp. 1191-1198.

Notations

b	=	Width of adherend
L	=	Distance from the end of laminate
l_0	=	Bond length
P	=	Ultimate load from test
P_n	=	Ultimate load from FEA
ΔP	=	Difference between ultimate loads from test and FEA (P_n-P)
R	=	Outer radius of steel tube
S	=	Bond strength in unit length
w	=	Strain energy density
w_p	=	Peel strain energy density
w_{pc}	=	Critical peel strain energy density
w_s	=	Shear strain energy density
w_{sc}	=	Critical shear strain energy density
x	=	Normalized distance from the end of laminate
π	=	Circular constant
ε_{ij}	=	Strain tensor
ε_n	=	Normal strain
ε_{nc}	=	Critical normal strain
ε_p	=	Peel strain
ε_s	=	Shear Strain
ε_{sc}	=	Critical shear strain
σ	=	Stress
σ_A	=	Hydrostatic stress
σ_{ij}	=	Stress tensor
σ_M	=	Deviatoric stress
σ_p	=	Peel stress
σ_s	=	Shear stress

NUMERICAL MODELLING OF TUBE AND FITTING ACCESS SCAFFOLD SYSTEMS

R. G. Beale*[1] and M. H. R. Godley[2]

[1]*Department of Mechanical Engineering, Oxford Brookes University, Gipsy Lane, Headington, Oxford, OX3 OBP, UK*
[2]*Slender Structures Group, OCSLD, School of the Built Environment, Gipsy Lane, Headington, Oxford Brookes University, Oxford, OX3 OBP, UK*
**Corresponding author, email: rgbeale@brookes.ac.uk, tel (44) 1865 483354, fax (44) 1865 483637*

ABSTRACT: This paper describes numerical modelling of tube and fitting access scaffold structures according to the new European standard EN12811. Firstly simplified one- and two-dimensional models are described. The results from these analyses are compared with the output from three dimensional finite element buckling and non-linear elastic analyses with good agreement. Buckling analyses show that effective lengths of tube and fitting scaffolds are strongly influenced by the pattern of ties to the building façade and in many cases much greater than those currently assumed in design being approximately equal to vertical tying increments and not the lift height. As a result of the analyses the authors recommend that the maximum vertical tying increments for large tube and fitting scaffolds should not be greater than every two levels. Wind loads parallel to façade were shown to generate uplift on some windward legs of façade braces which could cause premature failure of the scaffold. Current UK design practice which largely ignores the effects of wind loads is unconservative for large scaffolds. Recommendations for improved practice are made.

Keywords: semi-rigid connections, buckling analysis, scaffold structures, finite element analysis.

1. INTRODUCTION

The authors have made studies of the behaviour of proprietary scaffolding systems and of the behaviour of semi-rigid connections of the type used in scaffolds (Beale and Godley [1], Godley and Beale [2] and [3]). Previous work on the behaviour of tube and fitting systems was undertaken by Lightfoot et al [4] where the emphasis was on the importance of the behaviour of the connection.

The commonest type of scaffold within the UK is the tube and fitting scaffold which has over 80% of the scaffold market, proprietary and pre-formed scaffolds being more commonly used in specialised areas. Tube and fitting scaffolds are particularly popular in the erection of scaffolds around existing irregularly shaped buildings and for small domestic buildings. In the UK the design of tube and fitting scaffolds is regulated by BS 5973 [5]. This code uses linear analyses combined with the buckling lengths of the standards to take account of non-linear buckling effects. BS 5973 [5] implicitly suggests that the buckling length should be taken to be the same as the storey or lift height, irrespective of the position and frequency of any ties to the facade. The position and frequency of ties is determined by custom and practice and by the presence of wind loading due to sheeting. The arrival of a new European standard, EN12811-1 [6] means that current practice has had to be reviewed and that changes became necessary to design practice. The UK National Access and Scaffolding Confederation (NASC) commissioned the authors to develop a new design practice guide for tube and fitting scaffolds which conforms to the European standard [7]. One and two-dimensional models which were developed to produce the design guide and their verification by non-linear three-dimensional finite element analyses are reported in this paper.

2 SCAFFOLD COMPONENTS

2.1 Introduction

Tube and fitting scaffolding structures are erected against the façade of a building in order to provide access for the purposes of maintenance and repair. The shape and form of buildings commonly varies quite radically away from the regular and hence an efficient scaffolding system is one which, amongst its other attributes, can be arranged to accommodate a very large variety of configurations.

In the UK the traditional way of doing this is to construct the scaffold from tubes and connectors, called fittings. The tube is normally 48.3 mm diameter with a wall thickness of 4mm, manufactured from steel with a yield stress of 235N/mm^2.

The fittings come in a variety of styles but the most common types in use are the right angle coupler which connects two tubes at 90^o, the swivel coupler which allows the angle between the two connected members to vary, and the putlog coupler which connects tubes at right angles, but which has limited strength. Examples of these fittings are shown in Figure 1. A full description of these components is given in Godley and Beale [8].

2.2 Scaffold types

There are two primary types of access scaffold built from tubes and fittings. The first but less common type is the Putlog scaffold. This is shown in Figure 2 and comprises a line of columns or standards connected together at each level using right angle couplers by horizontal members called ledgers. This assembly is tied to the building façade at intervals by tie members. In addition putlog members which are tubes with flattened ends are fitted between the scaffold and the façade to provide a support for the timber scaffold planks which carry the load. The putlogs are connected to the ledgers with putlog couplers which leave the top surface of the putlog members flush to receive the timber planks. In-plane stiffness parallel to the façade is provided by façade bracing in the full height of the scaffold. For its stiffness normal to the façade the scaffold is dependent on the presence of the ties and their frequency.

The more common type of tube and fitting access scaffold is the independent tied scaffold shown in Figure 3. This scaffold is independent of the façade to the extent that it carries all the vertical loads and does not transfer any to the façade. There are two planes of standards and ledgers connected together with right angle couplers. They are linked together with transom members using putlog connectors and these transom members carry the scaffold boards. Diagonal bracing is installed in the plane parallel to the facade, but only in the front face of the scaffold. The rear face has no such bracing. Alternate pairs of standards are fitted with ledger bracing which is diagonal bracing in the plane normal to the façade. Independent tied scaffolds are tied to the façade at regular intervals, using a tie member connected to both standards. The tie member spans horizontally between the facade and the front braced face of the scaffold and thereby affords horizontal restraint to the rear face of the scaffold.

2.3 Scaffold Loading

The most recent European standard EN12811-1[6] defines the imposed loads for a number of scaffold classes. Unusually in a steel structure, self weight can be significant, particularly when the scaffold is boarded out at every level, and must be accounted for in the design. In the case of the

Putlog scaffold half of the imposed load is applied to the façade of the building.

Scaffolds are also exposed to wind loading. Wind loads can act parallel to the façade and normal to the façade. The intensity of the loading depends upon the wind speed and upon whether the scaffold is sheeted or unsheeted. In the direction normal to the facade, wind effects are not significant because they are usually reduced by the shielding effect of the façade, unless the façade is very permeable. When the façade is permeable, the wind loading induces bending in the members of the scaffold and may induce significant forces in the ties. In the unsheeted condition, wind loads parallel to the façade act on all the members of the scaffold. No shielding is allowed. These loads produce an overturning effect which induces an additional compressive force into the leeward members of the façade bracing panels. This is illustrated in Figure 4.

When the scaffold is sheeted, the area subjected to wind loads is much increased. When the wind blows parallel to the façade there is again a horizontal force which induces overturning effects and results in increased compression in the leeward leg of the bracing panels. This overturning effect is amplified by the effects of frictional drag on the sheeted face of the scaffold.

An additional effect of the wind blowing parallel to the façade is wind suction normal to the facade. This action puts the standards and ledgers into bending and induces significant loads into the ties to the facade. When the wind blows normal to the façade a sheeted scaffold on the windward face of the building will be subjected to considerable wind pressure. However, in the design of these structures, the assumption is that the rear face components such as the transoms and putlogs are in such close proximity to the facade that they will deflect into bearing with the facade. This action creates many points of support for the scaffold and thus reduces the bending moments induced into the members of the structure. When a scaffold is constructed on the leeward face of the building the wind forces are smaller but act in suction on the surface of the sheeting, inducing bending into the scaffold members and tension into the ties.

2.4 Structural characteristics of the couplers

In order to carry out this investigation the structural characteristics of the couplers had to be defined. A conservative approach would have been to assume that all connections were pinned and that no bending resistance was available in any of the joints. However, two connections offered the possibility of a significant cruciform bending stiffness and resistance, the right angle coupler and the putlog coupler. No experimental data was available to the authors on putlog connections. To obtain an estimate of their moment-rotation characteristics some preliminary cantilever tests were made at Oxford Brookes University on a typical right-angled coupler and on a putlog coupler. The results of these tests are shown in Figures 5 and 6. The solid lines in each figure are the results of individual experimental results and the dashed lines are the moment-rotation curves used in the analyses. As both putlog and right-angled connectors are manufactured by many different companies using forgings and pressings and hence have a range of stiffnesses and maximum moment capacities and as single values were required conservative values were used in the analyses. A research project is currently underway at Oxford Brookes University to obtain comprehensive design data.

In both cases the curves show the relationship between moment and rotation in cruciform bending of one side of the joint compared with the other about the Y axis in Figure 1(a). For both couplers, a stiffness and a design moment have been arbitrarily chosen below the experimental curves. The chosen characteristics are selected to allow for the statistical effects of determining the characteristic values that would have to be taken into account in a more formal assessment. In the case of the right angle coupler, this was a Type A coupler according to the designation of EN-74 [9].

The values chosen for the Type A coupler are 10kNm/radian and a characteristic moment of resistance of 0.4kNm. For the putlog coupler there are no figures available in British or European standards; the figures chosen here are 2kNm/radian and 0.06kNm for the characteristic moment of resistance. Apart from these values all other connections are assumed to be pinned.

2.5 Tie positions

The positions of ties which link the scaffold to the facade are crucial in any study of the buckling behaviour of an access scaffold. There are a very large number of possible tie patterns that can be used. In practice only regular patterns are of interest and those which represent the worst case. The critical parameters affecting structural behaviour are the vertical and horizontal intervals between ties. In this paper it is assumed that alternate pairs of ledger braced standards (or alternate pairs of single standards in the case of Putlog scaffolds) are tied and that the ties are in vertical rows and not staggered. In Figures 2 and 3 such a tie pattern is shown with ties at every third lift. Staggered tie patterns are more effective at restraining the standards against buckling, but the effect is not great. The effects of different tie patterns have been discussed by the authors in a previous paper (see Godley and Beale [3]).

3 THE BUCKLING BEHAVIOUR OF ACCESS SCAFFOLDS

3.1 Introduction

The authors have carried out an investigation into the buckling behaviour of scaffolds in an attempt to confirm apparent assumptions made in current British Standards governing scaffold design and to establish a simple design approach that avoids the use of sophisticated software.

The current UK design approach [5] is to carry out a linear analysis of the scaffold and to deal with the non-linear effects of buckling by using the effective length concept. An alternative to this approach is to use the amplification method to deal with the non-linearity. In both cases knowledge of the buckling modes and the associated buckling loads is required. Neither approach is as accurate as a full second order analysis. In this paper the buckling behaviour is described in terms of effective lengths in order to simplify comparisons with current practice.

In order to determine the effective lengths of scaffolds under different tie patterns unit loads were applied to the top of each standard and the critical load P_{cr} determined. The effective length L_E was then calculated using the formula

$$L_e = \sqrt{\frac{\pi^2 EI}{P_{cr}}} \tag{1}$$

where EI is the effective rigidity of the standard.

3.2 Two dimensional models

In the case of the Putlog scaffold, buckling in the plane of the façade is restricted by the presence of the facade bracing so that the buckling length is equal to the storey height. All analyses were undertaken with the storey or lift height taken to be 2.0m except that the first lift could be either 2.0m or 2.7m above the ground. Buckling normal to the facade is much influenced by the position of the ties. The standard which is not directly tied to the façade is the least restrained. Its horizontal restraints are provided at each level by the ledgers. The ledgers are normally put into bending as the buckling mode develops and act as horizontal linear springs. Because of the repetitive nature of the

structure, for a putlog scaffold, the bucking may be represented by the two column model shown in Figure 7.

This model has one tied column and one free column. The tied column is restrained, for the example in Figure 7, at every third level and the free column is linked to it by linear springs with a stiffness k. If the springs are stiff enough, the free column and the tied column buckle together at a load corresponding to an effective length equal to the tie interval. In the case of the example in Figure 7, with stiff springs the effective length is 6m and the ledgers do not flex but remain straight. If the springs are not stiff enough for this mode of buckling, the free column will buckle independently of the tied column at a load corresponding to an effective length greater than the tie interval.

Figure 8 shows the relationship between the effective length produced by the two-dimensional model of Figure 7 and the stiffness of the restraining springs. It was produced using a linear eigenvalue program. From the graph it can be seen that for a tie interval of 6m, for example, log10(spring stiffness) must exceed 0.34 if the two columns are to buckle together.

The ledger is a continuous beam along the face of the scaffold at each lift. The lowest stiffness it can afford to the free standard occurs when alternate free columns buckle inwards and outwards and the ledger behaves as a simply supported beam as shown in Figure 9. From this figure the deflection, Δ is given by:

$$\Delta = \frac{P(2L_b)^3}{48EI} \tag{2}$$

in which EI is the flexural rigidity of the ledger, P the applied load and L_b is the bay width, the distance between the columns. Hence the required stiffness, k, can be found by:

$$P = \frac{48EI}{(2L_b)^3}\Delta = k\Delta \tag{3}$$

The value of the stiffness k is therefore

$$k = \frac{48EI}{(2L_b)^3} \tag{4}$$

In the case of normal Putlog scaffolds, the stiffness afforded by the restraining ledgers is always sufficient for the columns to buckle together, except when the tie interval is 2m. This is illustrated in Table 1, where the effective lengths for three different bay lengths are tabulated for simply supported ledgers.

The highest value of stiffness that can be generated by the ledger is when it behaves as a fixed ended beam as shown in Figure 10. In this case

$$\Delta = \frac{P(2L_b)^3}{192EI} \tag{5}$$

which implies that

$$P = \frac{192EI}{(2L_b)^3}\Delta = k\Delta \tag{6}$$

Hence in this case the stiffness is given by

$$k = \frac{192EI}{(2L_b)^3} \tag{7}$$

Something close to this situation occurs if one free column buckles in isolation from the remainder of the columns, perhaps because it is carrying an additional axial load as part of a bracing system such as that shown in Figure 4. The curve in Figure 8 is still valid, and in Table 1 the effective lengths are shown for the fixed end mode for three different bay lengths.

The results in Table 1 show that in nearly all cases the effective length can be taken as equal to the tie interval. This is because for most of the cases considered, the stiffness provided by the ledger is sufficient to ensure that the free standard buckles with the tied standard. In those cases where there are ties at every level, bucking occurs in a mode where each free standard buckles alternately towards and away from the façade.

In the case of independent tied scaffolds buckling normal to the façade takes place in a mode where alternate non-tied standards buckle in alternate directions. Consequently for this case the scaffold model in Figure 7 can be used, because the ledger bracing simulates ties normal to the façade at every lift, provided that there is at least one tie per ledger braced frame. In the direction parallel to the façade buckling of the front face is governed by the façade bracing and the buckled length is equal to the lift interval. For the rear plane of standards, the buckling load is strongly influenced by the tie positions, and conservatively it could be assumed to be equal to the tie interval. However, the semi rigid nature of the connection between the standard and the ledger reduces the buckling length. Figure 11, drawn for a scaffold tied at every other lift, presents a suitable single column model of the buckling of a rear standard. This model consists of a column with horizontal restraints at the tie levels and rotational restraints at all the intersections with the ledger. The rotational stiffness, k_φ, of this connection is calculated for ledgers in double curvature between standards as shown in Figure 12.

The rotation, θ, of the ledger is

$$\theta = \frac{M}{2}\frac{L_b}{2}\frac{1}{3EI} = \frac{ML_b}{12EI} \tag{8}$$

where EI is the flexural rigidity of the ledger, L_b is the bay width and M the restraining moment applied to the standard from the ledgers. The rotation, ϕ, of the right angle coupler connecting the ledger and the standard of cruciform stiffness, k_c, between ledger and standard is given by

$$\phi = \frac{M}{k_c} \tag{9}$$

Hence the total rotation between ledger and standard is

$$\theta + \phi = \frac{ML_b}{12EI} + \frac{M}{k_c} = M\left(\frac{L_b}{12EI} + \frac{1}{k_c}\right) \tag{10}$$

The equivalent rotational stiffness, k_φ, at the connection is therefore

$$k_\varphi = \frac{M}{\theta + \phi} = \frac{1}{\frac{L_b}{12EI} + \frac{1}{k_c}} = \frac{k_c}{1 + \frac{k_c L_b}{12EI}} \tag{11}$$

An analysis of this model shows that the buckling lengths are a little smaller than the vertical interval between ties.

3.3 Three-dimensional finite element analyses

To validate the column models three-dimensional finite element models of the scaffolds were created using the LUSAS program [10]. Examples of the models are shown in Figure 13. The models were based on the following assumptions:

- The standards and ledgers were initially modelled with 4 Kirchoff elements per lift. These elements are non-conforming, curved beam elements which have three rotational and three translational degrees of freedom at each end and in addition at the midside node degrees of freedom corresponding to incremental changes in translation and rotation. For the non-linear analyses described later the Kirchoff elements were replaced by co-rotational elements with three translational and rotational degrees of freedom at each end as these had improved non-linear capability. The second moment of area of the ledgers was taken to be 138000mm^4.

- Joint elements were used to connect the standards and ledgers. These elements have three translational and three rotational degrees of freedom. Milojkovic et al [11] have shown that the 50mm offset between ledger and standard in tube-and-fitting scaffolds can be ignored for scaffold assemblies and hence in this analysis the standards and ledgers were co-planar. Constraint equations were used to enforce the condition of zero horizontal and vertical translations between ledger and standard.

- The putlog connections from the standard to the façade or between front and rear faces in the transoms of the tied scaffolds were modelled using bar elements with translational degrees of freedom at each end for the buckling analyses. For non-linear analyses the transom connections were modelled by co-rotational beam elements with rotational releases at the ends. This change was introduced to allow for the possibility of transom buckling. For both types of scaffold the connection at the façade was restrained horizontally parallel to the façade and vertically. The connection was free to move in a direction normal to the façade. In practice there are small frictional resistances normal to the façade but these are not possible to quantify and hence were ignored.

- For the Putlog scaffold the ties were modelled as bar elements and pinned at each end. In the case of the independent scaffold the ties were considered to be beams connecting the two faces parallel to the façade and going into the façade. At the façade the tie was pinned. Connections between each tie and the front and rear standards were modelled in the buckling analyses by using joint elements with constraint equations to remove translational degrees of freedom. For the non-linear analyses translational degrees of freedom were removed by giving the joints large axial stiffnesses.

- Façade and ledger bracing elements were modelled using bar elements. To allow for the reduction in axial stiffness due to bending in the diagonal elements an effective area of 16mm^2 instead of the full area of 557mm^2 of the standards, putlogs and ledgers was used. An explanation of the derivation of this reduction in strength is given in Godley and Beale [3].

- Plan bracing was inserted into the model in every fourth lift, fourth bay as a horizontal diagonal bar element with an effective area of 16mm^2.

- The supports to the ground were pinned.

- The loading from the scaffold boards, live loads, and dead load was applied at nodal points. Wind loading was applied as a combination of point and distributed loads to all standards. The

live loads are applied to the top two levels only as vertical loads in agreement with the European standard EN 12811-1 [6].

Once a linear model was proved to be correct a linear eigenvalue buckling analysis was carried out. Convergence difficulties were encountered in obtaining buckling modes for load cases combining wind and live and dead loads. These were due to the range of different stiffnesses in the structure - very low joint stiffnesses in combination with relatively high beam stiffnesses. However, for the buckling analyses reported in this paper good converged results were obtained for loads applied at the top of the scaffold. Figure 13 gives examples of the buckling modes determined.

The tie arrangements are shown in Table 2. Tables 3 and 4 give the results of the analyses for different bay widths. Note that the tie pattern for load case 5 defined in Table 2 has ties at 2m intervals and the effective lengths correspond to those in the first line of Table 2. Load cases 6, 7 and 8 have ties at 4, 6 and 8m intervals and the results are close to the figures in Table 1. They are a little higher in the finite element model because the height of the scaffold in this model was not always a multiple of the tie interval (The top lift was always tied in the finite element model). In addition for the independent tied scaffold effective lengths were determined for cases where the ledger brace was omitted (Table 5). The results are given for buckling both parallel to and normal to the facade for the independent tied scaffold. For the putlog scaffold buckling always occurred normal to the facade. Buckling parallel to the facade is constrained by the facade bracing and therefore has an effective length of either the lift height or the bottom storey height, whichever is greater.

3.4 Discussion of buckling results

The first result to be noted from the results concerning different tie heights is that the effective length of the scaffold standards is governed by the distance between tied levels, and not the distance between lift heights - the assumption made in the current British Standard. For example the effective length of an independent tied scaffold with a bay width of 2.1m, an initial lift height of 2.0m, lifts at 2.0m intervals and tied every 6.0m (case 7) is 4.81m and not 2.0m.

For the Putlog scaffold, buckling parallel to the facade is restricted by the storey height because of the presence of the facade bracing. Buckling normal to the facade is influenced by the position of ties. The standard not directly tied to the facade is the least restrained. Its restraints normal to the facade are provided at each level by the ledgers. Three modes of buckling can occur. In the first, all standards buckle in the same direction. In the second, alternate untied standards buckle inwards and outwards, the tied standard being unbuckled. The third mode occurs when an isolated standard buckles. The first mode normally occurs for Putlog scaffolds and is shown in Figure 13(c). However, when there is significant side load applied to the scaffold, the leeward standard of the bracing panel resisting the overturning moment due to this side load is subject to increased compression and may buckle in isolation. This is the third mode of failure and is shown in Figure 13(a) for a scaffold tied at every lift. The reduction in capacity due to the effects of side load on this bracing panel was reported by Godley and Beale in 1997 (Godley and Beale, [2]). The second mode occurs when the Putlog scaffold is tied at every level, as in cases 1 and 5.

Buckling of an independent tied scaffold normal to the facade occurs in a mode where the untied standards buckle in alternate directions. This mode is shown in Figure 13(b). This mode occurs because, by virtue of the ledger bracing and the fact that all ties are assumed to be attached to the ledger braced standards, the braced standard is effectively tied at every level. Consequently the buckling lengths are very close to those of the putlog scaffold with ties at every level. This applies

irrespective of the actual tie interval, provided that there is at least one tie at each ledger braced frame. Buckling parallel to the facade for the front face is governed by the facade bracing and the buckling length is approximately equal to the lift height. For the rear plane of standards, however, buckling is strongly influenced by the tie positions, and conservatively it could be assumed to be equal to the tie interval. However, the semi-rigid nature of the connection between ledger and standard reduces the buckling length. Figure 13(d) shows the buckled mode for the scaffold with ties at every alternate lift. Table 5 shows that the absence of ledger bracing makes little difference on the buckling parallel to the facade but reduces the buckling load normal to the facade.

Due to the large effective lengths of the standards which occur when scaffolds are tied at vertical intervals greater than every two lifts the authors recommend that all tube and fitting scaffolds should be tied at vertical intervals not greater than 4.0m. This recommendation was used in all the non-linear analyses. It is also to be noted that the buckling analyses have shown that the current UK standard BS5973 [5] which implicitly assumes an effective length equal to the maximum lift height yields unconservative results.

4 NON-LINEAR ANALYSES

4.1 Introduction

Non-linear elastic geometric analyses were performed with reasonable correspondence between the results from the three-dimensional analyses and the one- and two-dimensional analyses. Material non-linearity was considered by use of the interaction formulae given below.

In conformance with the European standard EN12811-1 [6] a load factor of 1.5 was applied to all loads. The following load combinations were considered for every scaffold analysed:

Load case 1: Self weight plus service imposed load plus frame imperfection load normal to the facade plus a horizontal load equal to 0.3kN in each bay normal to the facade at the working lift. The horizontal load is given in EN12811-1 [6] as a horizontal load to be applied when no wind load is applied.

Load case 2: Self weight plus service imposed load plus frame imperfection load normal to the facade plus service wind load normal to the facade.

Load case 3: Self weight plus out-of-service imposed load plus frame imperfection load normal to the facade plus out-of-service wind load normal to the facade.

Load case 4: Self weight plus service imposed load plus frame imperfection load parallel to the facade plus a horizontal load equal to 0.3kN in each bay parallel to the facade at the working lift.

Load case 5: Self weight plus service imposed load plus frame imperfection load parallel to the facade plus service wind load parallel to the facade.

Load case 6: Self weight plus out-of-service imposed load plus frame imperfection load parallel to the facade plus out-of-service wind load parallel to the facade.

Frame imperfections were ignored for the early buckling analyses which only considered point loads at the top of the scaffold. For the non-linear analyses these were represented by horizontal

loads directly proportional to all vertical loads with the constant of proportionality, ϕ, given by the formula

$$\phi = \phi_0 \left(0.5 + \frac{1}{n_c}\right)^{0.5} \left(0.2 + \frac{1}{n_s}\right)^{0.5} \tag{12}$$

in which n_c = the number of fully loaded standards (= no of bays)
n_s = the number of lifts
ϕ_0 = 0.01 (corresponding to the erection tolerance set in BS5973 [5])

These loads were applied either normal or parallel to the facade depending upon the load case being considered.

The non-linear analyses started from 10% of the design load and increments were made until either the structure was unable to carry further load or three times the design load was achieved.

The following analyses were made to each scaffold considered:

(i) A linear analysis to check structural loads and structural geometry including restraints.

(ii) A buckling analysis.

(iii) A non-linear analysis including geometrical $P-\delta$ non-linearity. This started from 10% of the design load and increments were made until either the structure was not able to carry further load or three times the design load was achieved.

(iv) A Fortran program was written to process the output of each load increment in the non-linear analysis. The following checks were incorporated:

$$\left(\frac{N_{Sd}}{P_c} + \frac{M_{xSD} + M_{zSd}}{M_{Rd}}\right) 1.1 = k \quad \text{(for compressive axial loads)} \tag{13}$$

$$\left(\frac{N_{Sd}}{Af_y} + \frac{M_{xSD} + M_{zSd}}{M_{Rd}}\right) 1.1 = k \quad \text{(for tensile axial loads)} \tag{14}$$

$$\frac{M_{coupler} \cdot 1.35}{400} = m_{test} \tag{15}$$

where N_{Sd} is the design axial load, M_{xSd} is the design bending moment about the xx axis, M_{zSd} is the design bending moment about the zz axis, P_c = 48kN for 2m lift and M_{Rd} =1.85kNm (plastic moment of resistance of a 4mm thick scaffold tube with f_y = 235N/mm^2). k and m_{test} are limit state values with values less than 1.0 implying that the test is satisfied and values greater than 1.0 implying that the element of the structure has failed. $M_{coupler}$ is the characteristic moment for the coupler. Initial checks of coupler and joint slippage were made but as the forces in the connections were low these checks were not made for all analyses. The use of a partial safety factor of 1.35 for the coupler test is always conservative. During the process of conducting the analyses it was suggested that the partial safety factor for the coupler test should be reduced to 1.1. However, throughout the analyses, the original moment test was always satisfied and so no change was made. Failure was deemed to have occurred when the limit state values exceeded 1.0 for any element in

the scaffold.

4.2 Loading

All dead loads were applied as point loads at the appropriate lift position. Different load distributions were made for tied scaffolds with and without cantilevered boards at the rear. For the independent tied scaffold an allowance was made for the diagonal brace in the plane normal to the façade but not for the diagonal brace parallel to the façade. To simplify loading data the loss of weight when ledger bracing was removed was ignored. This produced slightly conservative results. The weights of individual components are given in Table 6. These weights are in conformance with the weights given for these components in BS5973:1993 [5]. The mass of a coupler in this code is said to range from 1.1 to 2.25kg. The value of 1.8kg was an assumed median value.

For the non-linear analyses the imposed loads were uniformly distributed loads for Classes 1, 2, 3 and 4. For the service condition this load was applied to the top lift with 50% of the intensity applied to the second lift. In the out-of-service condition corresponding to the maximum load that the scaffold could carry under storm conditions this load was applied to the top lift only, reduced by the factor given in column 3 of Table 7.

Service wind load intensity was taken to be 200 N/m^2 on every element. For the out-of-service or storm wind load the intensity, q, was given by

$$q = a\ln(h) + b \tag{16}$$

where the values of the coefficients a and b were derived by regression from Table 4 of BS6399 part 2 [12], for different town and country distances (denoted by the abbreviations T and C in Table 8) and wind velocity factors (S). h is the height of the scaffold above ground level. In accordance with EN12811-1 [6] rules for temporary structures the out-of-service wind pressures were reduced to 70% of the values calculated by the above formula.

The direction of the wind load normal to the facade was such as to put the ties into tension. The compressive direction was not considered as it was assumed that the scaffold would deflect into bearing with the facade, this improving its stability.

For unsheeted scaffolds the wind load on standards, ledgers and transoms was applied as distributed line loads. The loads on toe boards and guard-rails were applied as point loads on the standards at the appropriate levels. The guard-rail wind load on the top lift was exceptionally applied at the top lift due to the model not including standards above the top lift level.

For sheeted scaffolds the following was applied:

Winds normal to the facade: pressure coefficient 0.5 normal to the facade, no load on the end of the facade
Winds parallel to the facade: pressure coefficient 1.0 on the ends parallel to the facade, 0.5 (suction) normal and 0.01 (friction) parallel to all front elements along the front of the facade.

For debris netted scaffolds the following was applied:

Winds normal to the facade: pressure coefficient 0.25 normal to the facade, no load on the end of the facade
Winds parallel to the facade: pressure coefficient 0.5 on the ends parallel to the facade, 0.25

(suction) normal and 0.03 (friction) parallel to all front elements along the front of the facade.

To calculate the equivalent wind loads for both sheeted and debris netted scaffolds the load was applied to each bay and lift panel as shown in elevation in Figure 14. The areas of each subsection were calculated and the total load on the panel distributed to the ledgers and standards in proportion to the area of each subsection.

A small correction was made to the bottom lift where it was assumed that the wind load was only applied to the ledger above the panel and to the adjacent standards. The trapezoidal distribution was applied to the largest element of either the standard or the ledger. The effect of wind loads acting on the guard-rails was ignored as it would have meant two different loading distributions for boarded and unboarded scaffolds.

For the in-service wind condition the trapezoidal and triangular loads were modelled accurately as the program was able to apply distributed multi-linear constant loads. For the out-of-service load condition the assumption was made that the logarithmic wind distribution could be approximated to the rectangle by applying the appropriate height pressure at nodal points and using linear interpolation. For a 20m high scaffold the error in this assumption was shown to be less than 0.1%. In addition as the program could not handle trapezoidal and triangular loads with variable magnitudes these loads were modelled by uniformly distributed loads with the same total force on the sides of each panel. The resulting total load applied to the scaffold by LUSAS was within 0.5% of the total load calculated by integration using a symbolic algebra package.

4.3 Results and Discussion

Table 8 summarises the scaffolds analysed. For these analyses the scaffolds had all lifts including the first at 2.0m height and alternative pairs of standards tied at lifts at heights 4.0m, 8.0m, 12.0m, etc. The top lift was always tied. Note that partial ledger bracing cases required two sets of full analyses - one with the bottom two ledger braces removed and one with the top two ledger braces removed. The cantilevered cases included one board cantilevered behind the rear face, adjacent to the facade. Further details of the loads applied to each scaffold are given in Beale & Godley [8]. Three different face bracing patterns were analysed – one bay every five bays, two adjacent bays every five bays and full diagonal bracing, repeating every five bays. The scaffold dimensions were chosen to verify the two-dimensional model. They were the tallest scaffolds which the one and two-dimensional models calculated that would support the required Class of Load under the action of its corresponding wind load.

The results of the analyses are summarised in Table 9 with sample ultimate modes of failure given in Figure 15. The method of applying load in LUSAS is by use of a load parameter called T_λ. A value of $T_\lambda = 1$ is the design load. The value of the limit state k defined by the maximum value of the tests described in Eqs. (13) or (14) shows if the scaffold successfully passes the test. If k is less than 1 the scaffold passed the test. The coupler moment test (Eq. (15)) was never critical in any of the analyses and hence is not shown.

From Table 9 it can be seen that all the Putlog scaffolds were capable of carrying the design load, with the proviso that the six lift, class 1, unboarded, two bays in five braced scaffold (reference number 2) developed a 2kN uplift force and the nine lift, class 2, unboarded, five bays in five braced scaffold (reference number 6) developed a 5.4kN uplift force in the windward leg of the facade brace. In both cases this was under the out-of-service wind load combination parallel to the facade. Most of the tied scaffolds were capable of handling the design loads. Certain results must

be commented upon, however. Firstly, the cantilevered, unsheeted, 8 lift scaffold with partial ledger bracing (reference number 7) had high moments in the tie connecting the third pair of standards to the facade at the fourth lift level under the condition of out-of-service wind parallel to the face. These moments, whilst being individually acceptable, caused high values in the interaction formula. For example at $T_\lambda = 1$, for this element $M_z = 1.69$kNm. Secondly, the Class 4, 17 lift tied scaffold (reference number 8) marginally failed to carry the design load due to the same cause under the same wind load. However, it is felt that this result demonstrates that the approximate two-dimensional analysis accurately predicts maximum failure loads. In addition it is unlikely that this marginal failure would ever be observed, due to the simplifications made in the analysis which have all been designed to be conservative. Thirdly, the 8 lift, debris netted, boarded scaffold (reference number 9) demonstrated significant bending in the rear ledgers under both out-of-service wind load conditions. In addition the model generated significant tensile forces in the rear ledger members. This is thought to be due to the boundary conditions applied to the ties which allowed high horizontal reactions to develop. Modifications to the computer model were made where horizontal springs were introduced at the end of each tie. These springs reduced the values of the horizontal reaction forces and hence reduced the axial forces in the rear ledgers. However, they made very little difference to the ultimate limit state which was governed by ledger failure.

5 CONCLUSIONS

One-, two- and three-dimensional numerical models of tube and fitting scaffolds have been developed which show agreement with respect to each other; the three–dimensional results confirming the approximate one- and two-dimensional results. The approximate models are adequate to predict scaffold behaviour and can easily be used in design.

Buckling analyses have shown that the effective lengths of tube and fitting scaffolds are approximately equal to the vertical tying intervals and not the lift height as assumed in the current UK standard. The authors recommend that the vertical tying increments for all access tube and fitting scaffolds should not be more than every two levels. Wind load effects parallel to the façade can cause uplift on the leeward legs of façade braces which could cause premature scaffold collapses and must therefore be considered when designing scaffolds. Current UK design practice based on BS5973 [5] which largely ignores wind loads can be unconservative, especially for large scaffolds.

6 REFERENCES

[1] Beale, R.G. and Godley, M.H.R., "The Analysis of Scaffolding Structures using LUSAS", Proceedings LUSAS 1995, Tewkesbury, 1995, pp.10-24.

[2] Godley, M.H.R. and Beale, R.G., "Sway Stiffness of Scaffold Structures", Structural Engineer, 1997, 75(1), pp. 4-12.

[3] Godley, M.H.R. and Beale, R.G., "Analysis of Large Proprietary Access Scaffold Structures", Proceedings Institution of Civil Engineers, Structures and Buildings, 2001, 146(1), pp. 31-40.

[4] Lightfoot, E. and Oliveto, G., "The Collapse Strength of Tubular Steel Scaffold Assemblies", Proceedings Institution of Civil Engineers, 1997, Part 2, pp. 311-329.

[5] BS 5973:1993, "Code of practice for access and working scaffolds and special scaffold structures", British standards Institution, London, 1993.

[6] EN 12811-1, "Temporary works equipment, Part 1: Scaffolds-Performance requirements and general design", European committee for standardisation, Brussels, 2003.

[7] NASC, "TG20:05 Guide to Good Practice for Scaffolding with Tubes and Fittings", National Access and Scaffolding Confederation, London, 2004.

[8] Godley, M.H.R. and Beale, R.G., "The Structural Behaviour of Tube and Fitting Access Scaffold Systems", Proceedings of the Seventh International Conference on Computational Structures Technology, Lisbon, Paper 251, 2004.

[9] EN74, "Couplers, Loose Spigots and Base-Plates for use in Working Scaffolds and Falsework made of Steel Tubes; Requirement and test procedures", British Standards Institution, London, 1988.

[10] LUSAS, "Lusas 13.4 User Manual", FEA Ltd, 2002.

[11] Milojkovic, B., Beale, R.G. and Godley, M.H.R., "Modelling Scaffold Connections", Proceedings of the Fourth ACME UK Annual Conference, Glasgow, 1996, pp. 85-88.

[12] BS 6399-2, "Loading for Buildings. Code of Practice for wind load", British Standards Institution, London, 1997.

FIGURE CAPTIONS

Figure 1. Three types of scaffolding coupler

Figure 1(a). (a) right-angle coupler
Figure 1(b). Swivel coupler
Figure 1(c). Putlog coupler

Figure 2. Typical Putlog Scaffold

Figure 3. Typical Independent Tied Scaffold

Figure 4. Bracing action under side loads

Figure 5. Moment-Rotation Characteristics for a Putlog Coupler

Figure 6. Moment–Rotation Characteristics for a Right Angle Coupler

Figure 7. Two column Putlog model for buckling normal to the facade

Figure 8. Variation of effective length with spring stiffness

Figure 9. Derivation of stiffness for 'pinned' ledgers

Figure 10. Derivation of stiffness for 'fixed' ledgers

Figure 11. Single column model for the rear face of a tied scaffold

Figure 12. Derivation of rotation stiffness for standard-ledger connection in double curvature

Figure 13. Examples of buckling modes

Figure 13(a). Buckling of leeward braced standard normal to the facade for a Putlog scaffold
Figure 13(b). Buckling of independent tied scaffold normal to the façade
Figure 13(c). Uniform buckling of Putlog scaffold normal to the facade
Figure 13(d). Buckling of tied scaffold parallel to the façade (only the rear face buckles)

Figure 14. Wind load distribution patterns

Figure 15. Examples of ultimate failure modes

Figure 15(a). Tied scaffold buckling normal to the facade
Figure 15(b). Putlog scaffold buckling normal to facade
Figure 15(c). Tied scaffold with rear face buckling parallel to facade
Figure 15(d). Tied scaffold buckling normal to facade with no ledger bracing in bottom two lifts

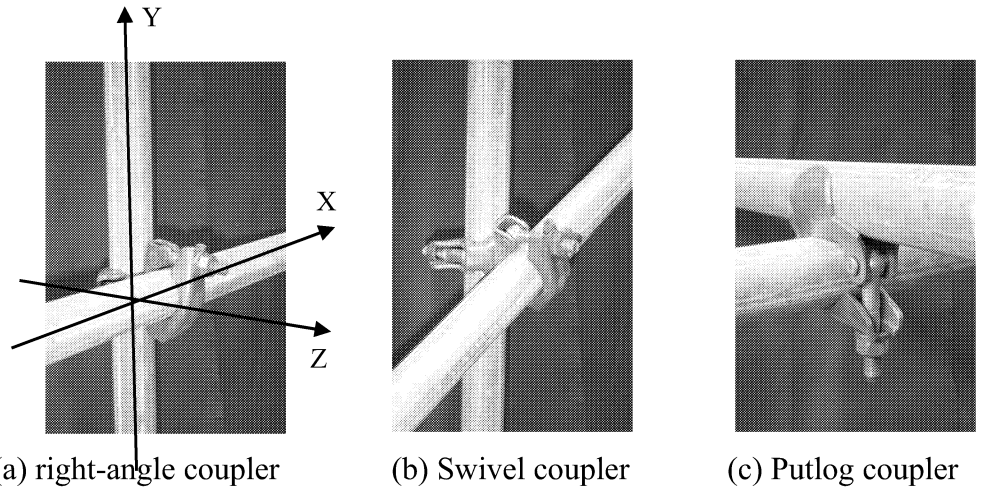

Figure 1. Three types of scaffolding coupler

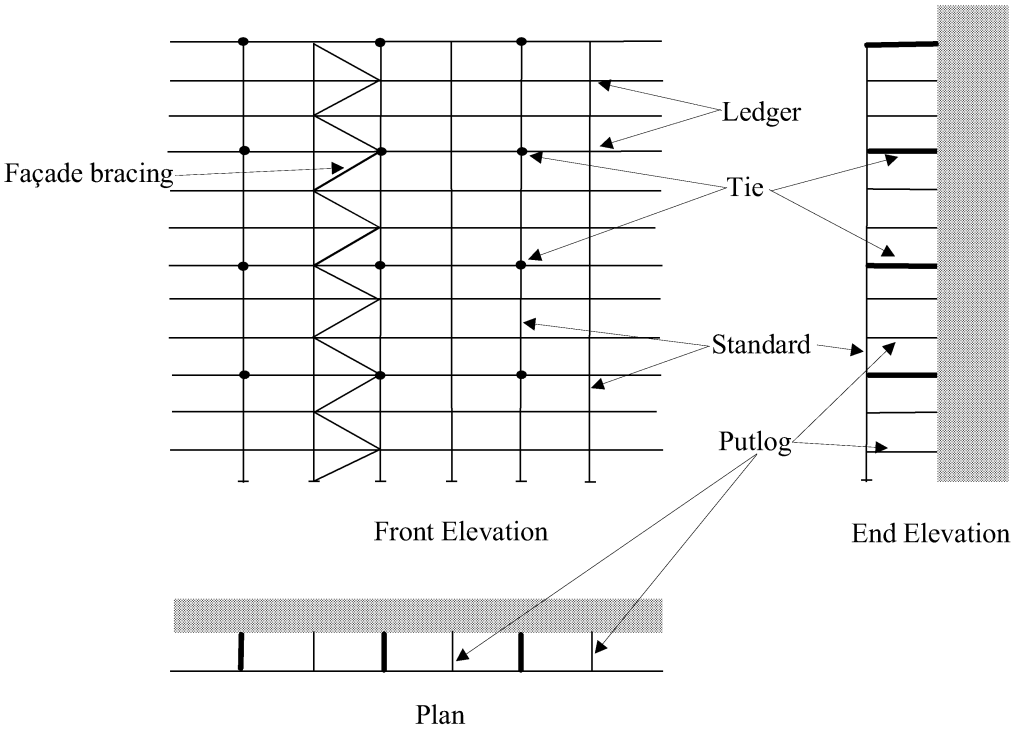

Figure 2. Typical Putlog Scaffold

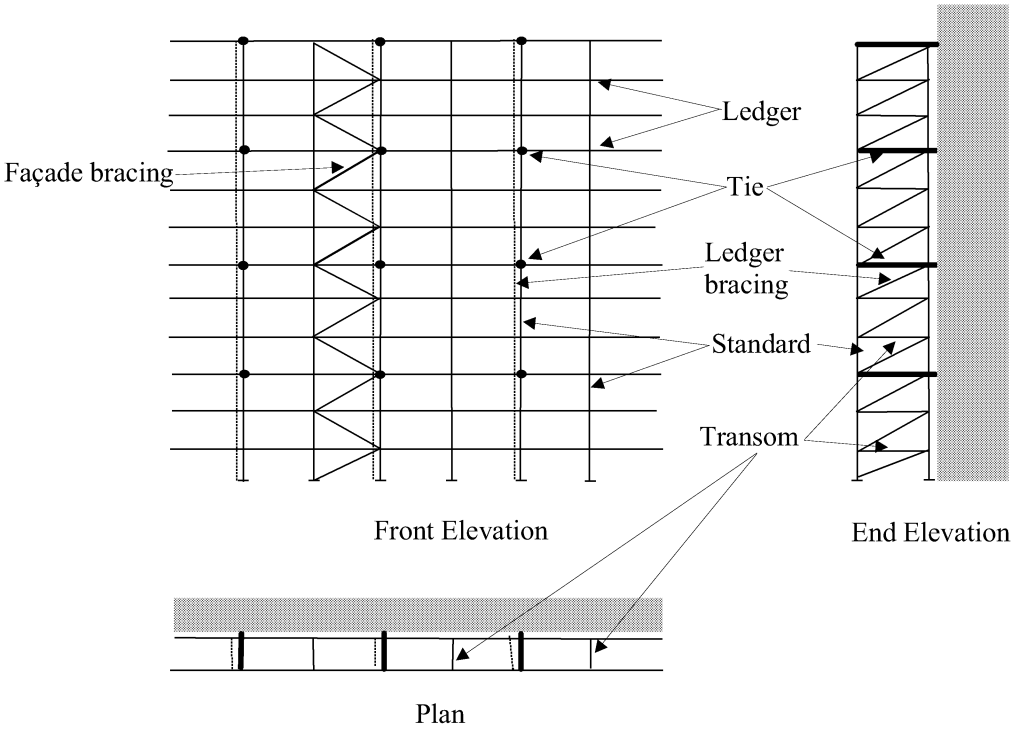

Figure 3. Typical Independent Tied Scaffold

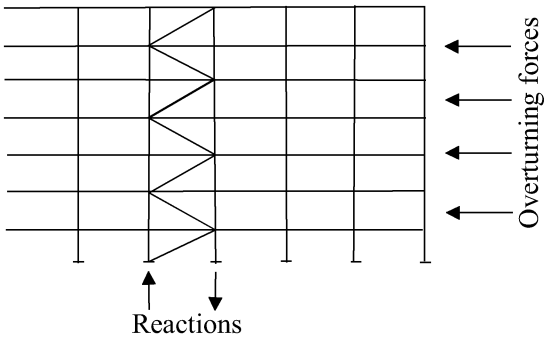

Figure 4. Bracing action under side loads

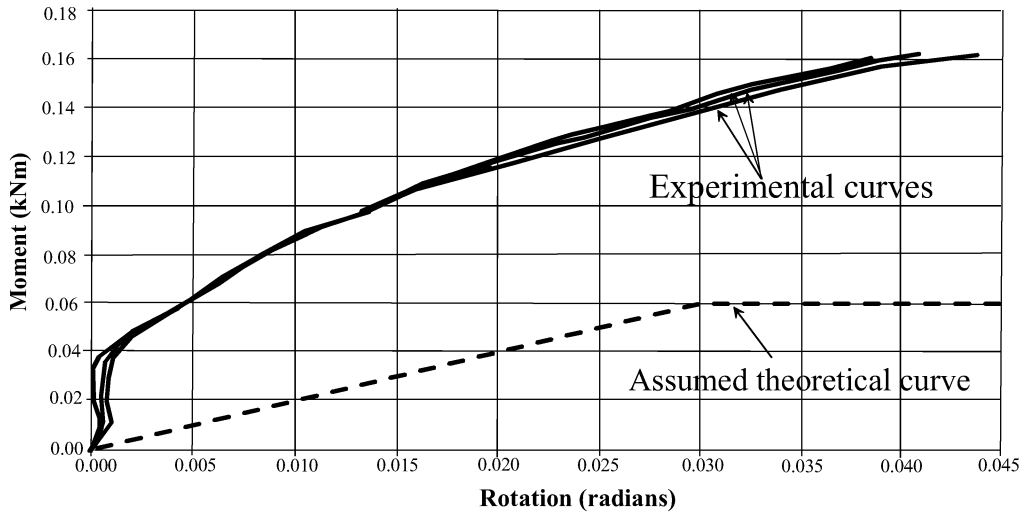

Figure 5. Moment-Rotation Characteristics for a Putlog Coupler

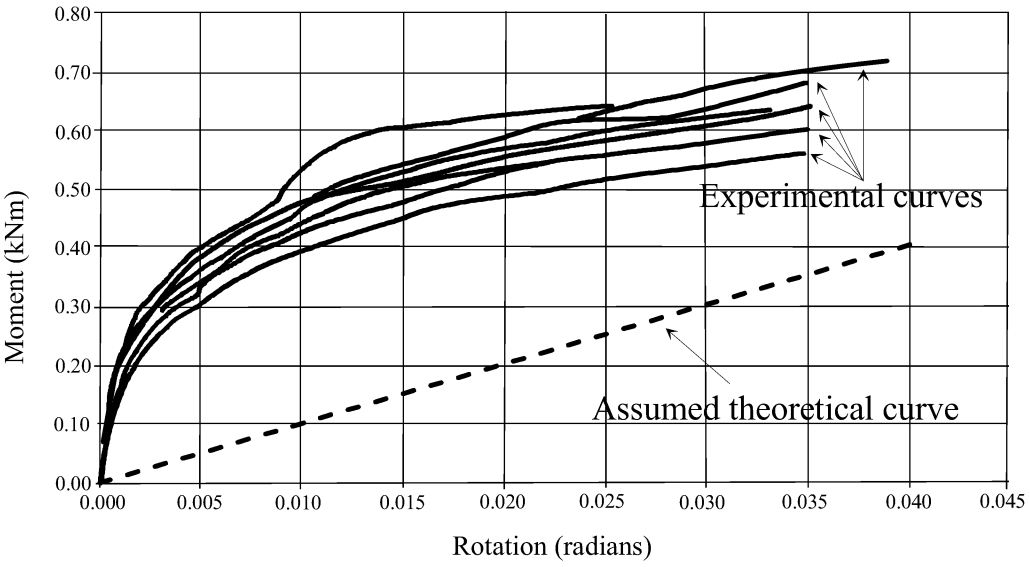

Figure 6. Moment–Rotation Characteristics for a Right Angle Coupler

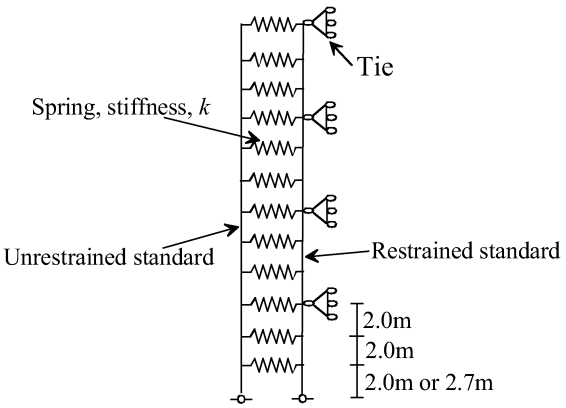

Figure 7. Two column Putlog model for buckling normal to the facade

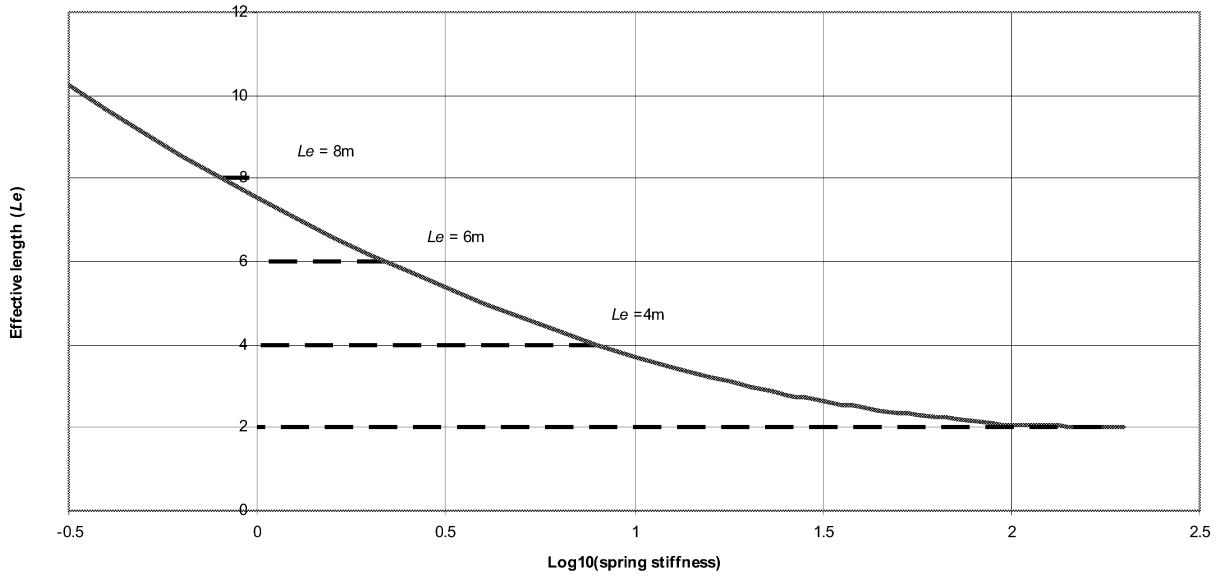

Figure 8. Variation of effective length with spring stiffness

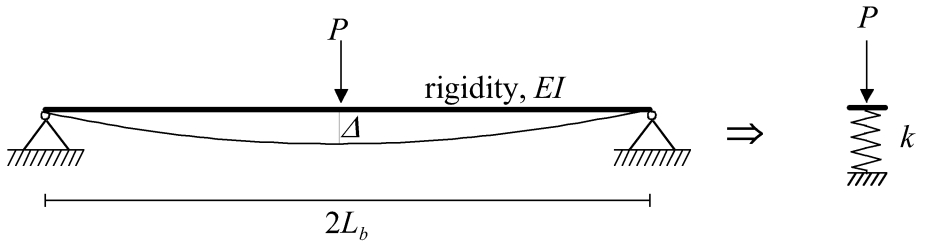

Figure 9. Derivation of stiffness for 'pinned' ledgers

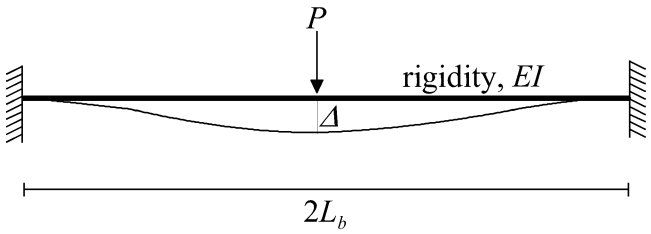

Figure 10. Derivation of stiffness for 'fixed' ledgers

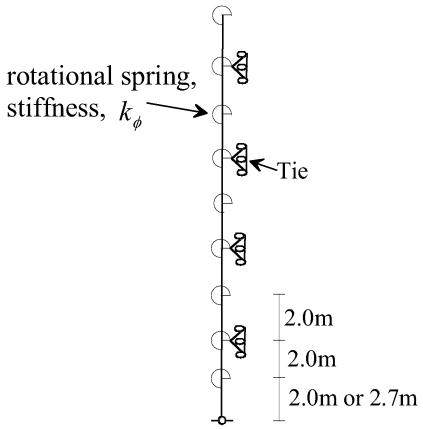

Figure 11. Single column model for the rear face of a tied scaffold

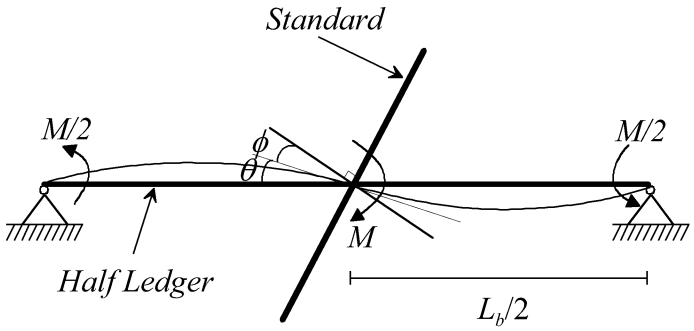

Figure 12. Derivation of rotation stiffness for standard-ledger connection in double curvature

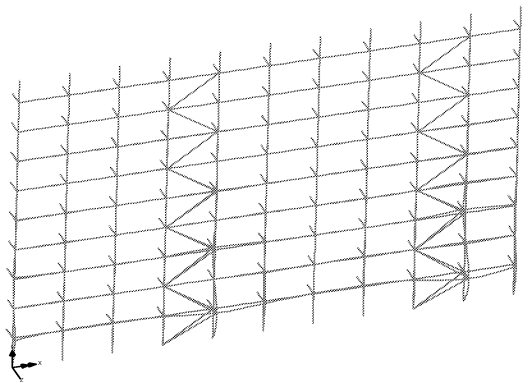

(a) Buckling of leeward braced standard normal to the facade for a Putlog scaffold

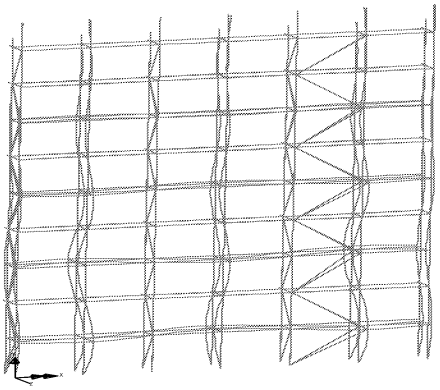

(b) Buckling of independent tied scaffold normal to the façade

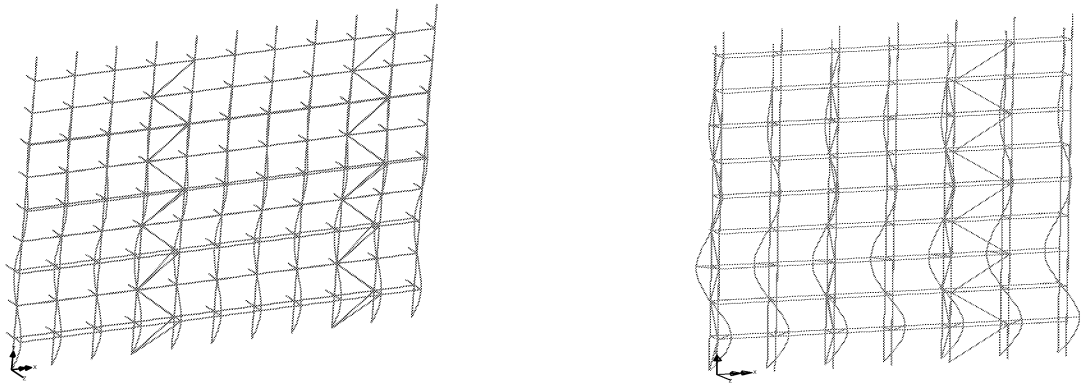

(c) Uniform buckling of Putlog scaffold normal to the facade

(d) Buckling of tied scaffold parallel to the facade (only the rear face buckles)

Figure 13. Examples of buckling modes

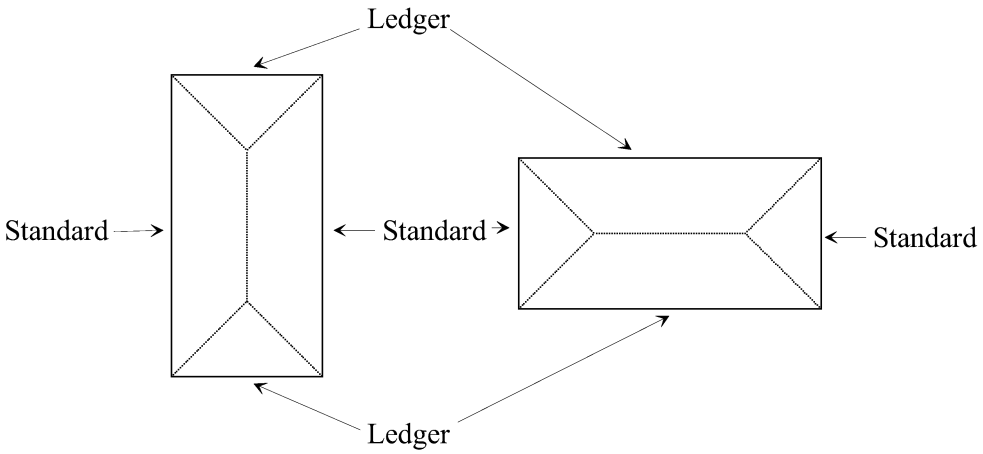

Figure 14. Wind load distribution patterns

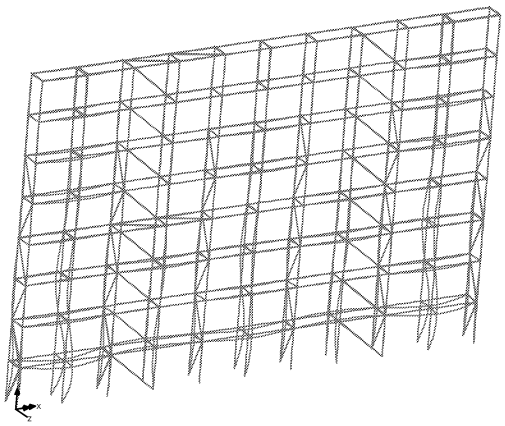

(a) tied scaffold buckling normal to facade

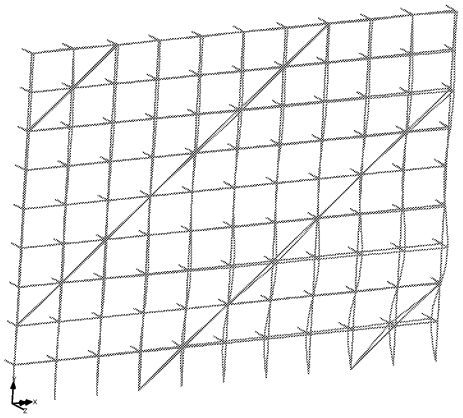

(b) Putlog scaffold buckling normal to facade

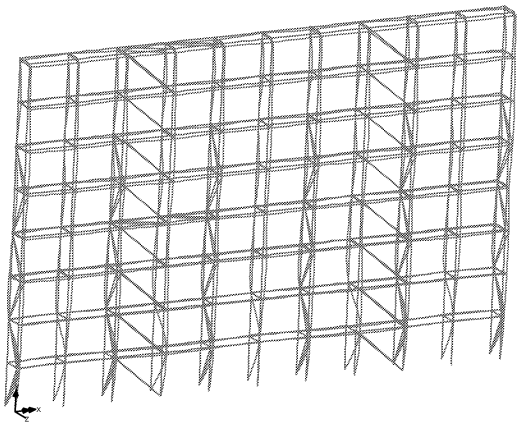

(c) tied scaffold with rear face buckling parallel to facade

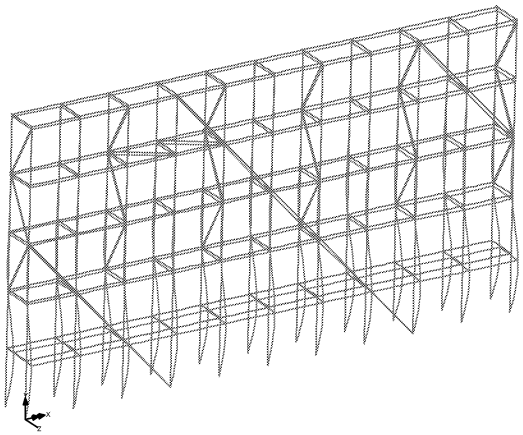

(d) tied scaffold buckling normal to facade with no ledger bracing in bottom two lifts

Figure 15. Examples of ultimate failure modes

Table 1. Effective lengths for Putlog scaffolds found from the two-dimensional model

	Tie Interval	Span = 2.7m	Span = 2.1m	Span = 1.8m
Simply Supported Ledgers	2m	3.94	3.17	2.77
	4m	4.06	4.00	4.00
	6m	6.00	6.00	6.00
	8m	8.00	8.00	8.00
Fixed Ended Ledgers	2m	2.64	2.18	2.02
	4m	4.00	4.00	4.00
	6m	6.00	6.00	6.00
	8m	8.00	8.00	8.00

Table 2. Tie Patterns

Case	Tie position above base (m)								
1	2.7	4.7	6.7	8.7	10.7	12.7	14.7	16.7	18.7
2	2.7		6.7		10.7		14.7		18.7
3	2.7			8.7			14.7		18.7
4	2.7				10.7				18.7
5	2.0	4.0	6.0	8.0	10.0	12.0	14.0	16.0	18.0
6		4.0		8.0		12.0		16.0	18.0
7			6.0			12.0			18.0
8				8.0				16.0	18.0
9	2.0		6.0		10.0		14.0		18.0
10	2.0			8.0			14.0		18.0
11	2.0				10.0				18.0

Table 3. Effective lengths of Putlog scaffolds for different bay widths buckling normal to the façade determined by the three-dimensional analysis

Case	1.8m	2.1m	2.7m
1	2.83	3.17	3.94
2	3.91	3.92	3.99
3	5.03	5.04	5.06
4	7.24	7.24	7.26
5	2.77	3.16	3.94
6	3.90	3.91	4.03
7	6.00	6.00	6.00
8	7.20	7.21	7.25
9	3.90	3.91	3.99
10	4.99	4.99	5.02
11	7.39	7.20	7.35

Table 4. Effective lengths of independent tied scaffold with full ledger bracing

	Parallel to façade			Normal to facade		
Case	1.8m	2.1m	2.7m	1.8m	2.1m	2.7m
1	2.39	2.29	2.29	2.83	3.17	3.94
2	3.42	3.42	3.43	2.85	3.19	3.95
3	4.16	4.16	4.18	2.87	3.21	3.95
4	5.03	5.04	5.01	2.90	3.27	4.01
5	1.90	1.90	1.90	2.77	3.16	3.94
6	3.56	3.56	3.56	2.78	3.18	3.95
7	4.81	4.81	4.83	2.90	3.25	3.98
8	5.55	5.57	5.57	3.29	3.18	3.96
9	3.40	3.41	3.41	2.84	3.19	3.95
10	4.12	4.13	4.13	2.86	3.21	3.95
11	5.00	5.02	5.04	2.90	3.26	4.01

Table 5. Effective lengths of independent tied scaffold with partial ledger bracing

		Parallel			Normal		
Description	Case	1.8m	2.1m	2.7m	1.8m	2.1m	2.7m
No bottom brace	2	3.46	3.47	3.47	3.21	3.37	3.57
	9	3.45	3.45	3.45	3.20	3.36	3.56
No brace in bottom two levels	2	3.46	3.47	3.47	3.21	3.38	3.57
	9	3.45	3.45	3.45	3.20	3.36	3.56
No brace in second and third levels from bottom	2	3.42	3.42	3.42	3.26	3.40	3.58
	9	3.40	3.41	3.41	3.22	3.37	3.56
No ledger brace	2	3.41	3.42	3.43	3.70	3.74	3.81
	6	3.56	3.56	3.56	3.75	3.77	3.81
	9	3.40	3.40	3.41	3.69	3.73	3.81

Table 6. Weights of scaffold components

Component	Weight
Coupler	1.8 kg
Ledger, standard, putlog, guard-rail	4.37 kg/m
Toe board	5.36 kg/m

Table 7. Table of loads

Class	Load intensity (kN/m^2)	Reduction factor	No. of Boards	Bay width (m)
1	0.75	0.00	3	2.7
2	1.50	0.25	4	2.4
3	2.00	0.25	5	2.1
4	3.00	0.50	5	1.8

Table 8. Scaffolds Analysed

Scaffold type	Ref. No.	Class	Sheeted or not	Boarded or not	Ledger bracing	Wind Storm param. **S**	T or C	Dist. to Sea	No of levels	Facade bracing
Putlog	1	1	not	yes	N/A	20	T	100	6	2 bays in 5
Putlog	2	2	not	not	N/A	24	C	0.1	9	5 bays in 5
Independent	3	2	not	yes	part	20	T	10	8	1 bay in 5
Independent	4	3	debris	not	full	24	C	10	17	2 bays in 5
Independent	5	4	sheeted	yes	part	28	T	0.1	5	5 bays in 5
Putlog	6	1	not	not	N/A	28	T	10	6	2 bays in 5
Independent	7	3 cant	not	yes	part	40	T	0.1	8	1 bay in 5
Independent	8	4 cant	not	not	full	40	C	100	17	5 bays in 5
Independent	9	1	debris	yes	full	32	T	0.1	8	2 bays in 5
Independent	10	4	sheeted	not	part	32	T	100	5	5 bays in 5

Table 9. Results of analyses

Ref. No.	Load case giving maximum limit state	Max k at T_λ =1	Max T_λ	Mode
1	Service wind, normal to façade	0.696	6.360	Buckling normal to façade
2	Service wind, normal to façade	0.375	2.130	Buckling normal to façade
3	Service wind, normal to façade	0.730	1.845	Buckling normal to façade
4	Service wind, parallel to façade	0.458	1.947	Buckling parallel to façade
5	Out-of-service wind, parallel to façade	1.006	2.641	Buckling normal to façade
6	Out-of-service wind, normal to façade	0.549	3.000	Not buckled, maximum increments exceeded
7	Out-of-service wind, parallel to façade	0.984	1.575	Not buckled, convergence failure
8	Out-of-service wind, parallel to façade	1.072	2.407	Not buckled, excessive bending in ledger
9	Out-of-service wind, parallel to façade	0.975	3.000	Not buckled, maximum increments exceeded
10	Out-of-service wind, parallel to façade	0.730	3.000	Not buckled, maximum increments exceeded

SEISMIC PERFORMANCE OF FRAMES WITH STEEL-CONCRETE COMPOSITE BEAMS: EXPERIMENTAL AND THEORETICAL INVESTIGATION

W.C. Xue[1], J. Li, L. Li and K. Li

[1]*Department of Building Engineering*
Tongji University, Shanghai, China
Email: xuewc@mail.tongji.edu.cn; Fax: +86-21-65986435; Tel: +86-21-65980418

ABSTRACT: This paper aims to study the seismic performance of moment-resisting frames consisting of steel-concrete composite beams subjected to reversed cyclic displacement. The failure patterns, failure mechanism, hysteretic model, deformation-restoring behavior, displacement ductility and energy dissipation capacity of the composite frames are discussed. Hinge is first formed at the composite beam ends. Failure of the two frames under low cyclic displacement reversals is finally governed by crushing and spalling of concrete at top and bottom of columns. Studies also show that the composite frames behave in a ductile manner, and the seismic performance of the composite frames can be significantly improved by the steel-concrete composite beams. In addition, a modified program is employed for full-range analysis of the composite frames.

Keywords: steel-concrete composite beam, frame, seismic performance, failure mechanism, hysteretic model, ductility, energy dissipation, full-range analysis

1. INTRODUCTION

The composite beams show good loading capacities due to composite action between concrete slabs and steel beams through shear connectors. In recent years, many studies focused on the moment resisting frames consisting of composite beams. Previous studies investigated the static behavior (Kennedy & Grace [1], Kocsis [2], Ayyub [3], Li et al [4], Nie & Shen [5], Asta & Dezi [6]) and seismic behavior of steel-concrete composite beams (Nie et al [7] and Xue et al [8]) and composite frames (Thermou et al [9] and Bursi et al [10]). However, few attentions have been paid to investigate the influence of prestressing in composite beams on the seismic performance of frames. This paper aims to investigate the seismic performance of frames with nonprestressed or prestressed composite beams according to low reversed cyclic loading tests and FEM analysis.

2. TEST SETUP

2.1 Design of specimens

Two frames were tested, in which one is fabricated with nonprestreesed steel-concrete composite beams (denoted as syf-1) and the other is fabricated with post-tensioned prestressed steel-concrete composite beams (denoted as syf-2). Details of the two frames are presented in Table 1 and Figure 1.

The two one-story one-bay frames were identical in dimensions, with beam span of 4800mm and column height of 1750mm. All composite beams have the span-to-depth ratio of 16 and depth of 300mm.

Table 1. Details of the two composite frames

Specimens	syf-1	syf-2
Externally prestressed tendons in steel beams	—	$6\phi^s5$
Unbonded tendons in slabs	—	$8\phi^s5$
Steel bars in slabs	Double 7Φ12	Double 7Φ10
Thickness of slabs (mm)	600	600
Spacing of stud connectors (mm)	100	100

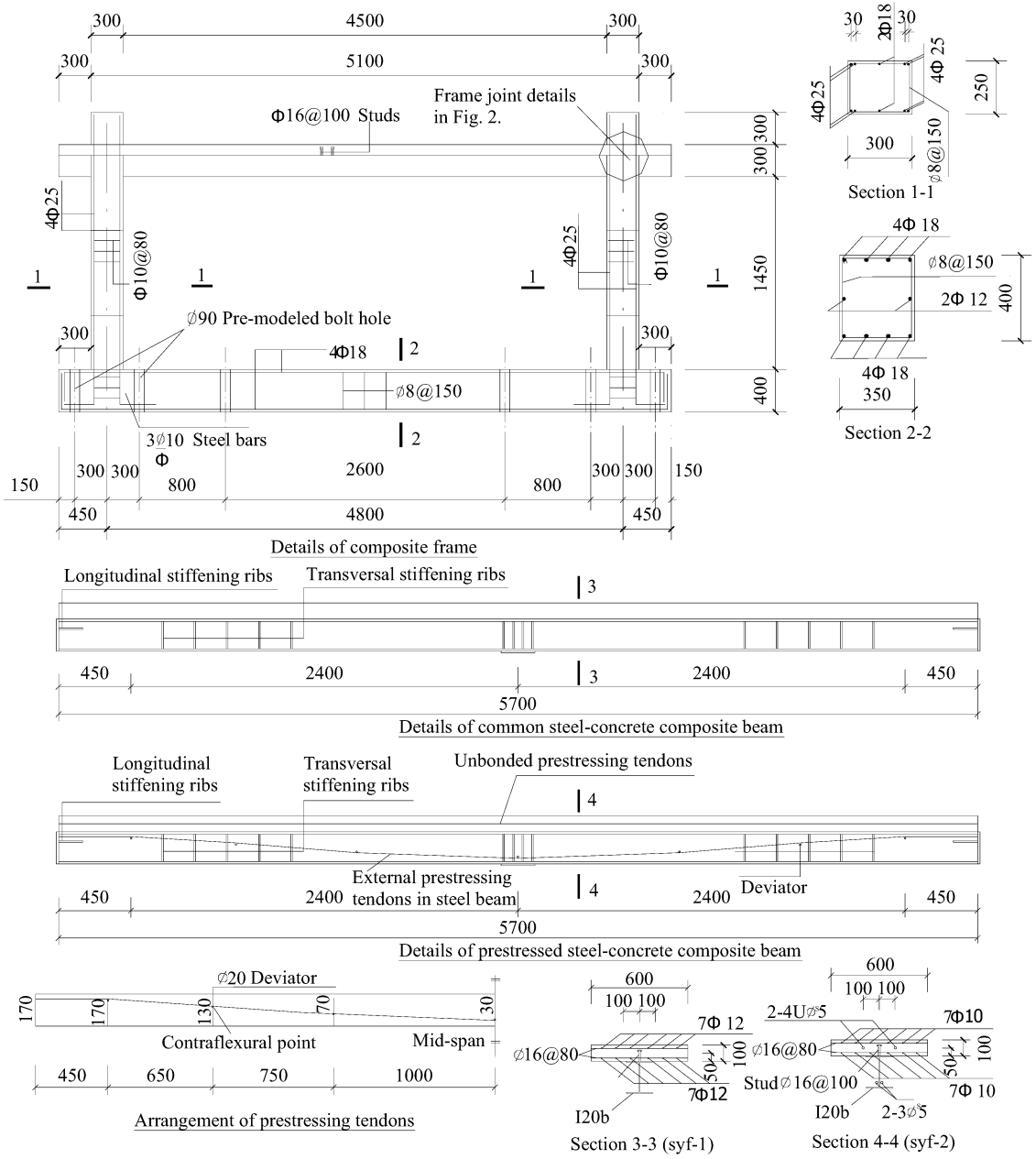

Figure 1. Details of the two composite frames

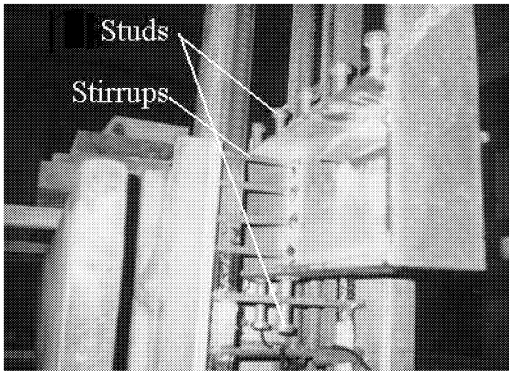

Figure 2. Details of the frame joint

Both frames were casted with C40 concrete. A3 steel was used for steel beams and 16Mn steel with yield stress of 480MPa was used for stud connectors. Steel tendons and five types of steel bars were also used. Mechanical properties of these materials were tested and presented in Table 2 and 3.

Table 2. Mechanical properties of reinforcing bars

Material Properties	A3 steel	Steel bars					Steel tendons
		Φ6	Φ10	Φ12	Φ18	Φ25	Φ^{s}5
Yield stress (f_y) (N/mm^2)	301.09	361	313	331	359	346	
Ultimate stress (f_u) (N/mm^2)	445.72	498	441	517	527	532	f_{ptk}=1824
Modulus of elasticity E_s (N/mm^2)	1.93 x10^5	2.11 x10^5	1.37 x10^5	1.48 x10^5	1.69 x10^5	1.73 x105	1.89 x10^5
Elongation (%)	27.8	22.3	22.5	24.8	21.6	19.8	13.2

Table 3. Mechanical properties of concrete

Mechanical properties	Cylinder compressive strength f_c (N/mm^2)	Cube compressive strength f_{cu} (N/mm^2)	Modulus of elasticity E_c (N/mm^2)
Concrete (C40)	33.94	50.36	3.36×10^4

2.2 Testing and Measurements

The two frames were tested under reversing lateral displacement and are shown in Figure 3. Axial compression ratios of columns and vertical loads of beams were determined in accordance with the construction practices. Here, the axial compression ratio is defined as

$$\mu_0 = \frac{N}{f_c \cdot A} \tag{1}$$

where μ_0 is the axial compression ratio, N is the axial load, f_c is the cylinder compressive strength of concrete and A is the area of column cross-section.

The lateral displacements, simulating seismic loads, were cyclically applied by using hydraulic actuators. All frames were loaded to failure. Figure 4 shows the loading history of the reversed cyclic load tests. The first cycle was load-controlled, in which frames were loaded until cracks were formed at top of columns. The load corresponding to the first cracking of frames was defined as P_{cr}. The subsequent cycles were displacement-controlled, in which beams were displaced to Δ_y for each cycle. Here, Δ_y is the yield displacement at top of columns, which corresponds to the yielding of the

composite frames. All frames were loaded three cycles in every levels of displacement. Thus, these displacements were arranged in successive sets of cycles, namely as $+1\Delta_y$、$-1\Delta_y$、$+2\Delta_y$、$-2\Delta_y$、$+3\Delta_y$、$-3\Delta_y$……, being multiples of Δ_y.

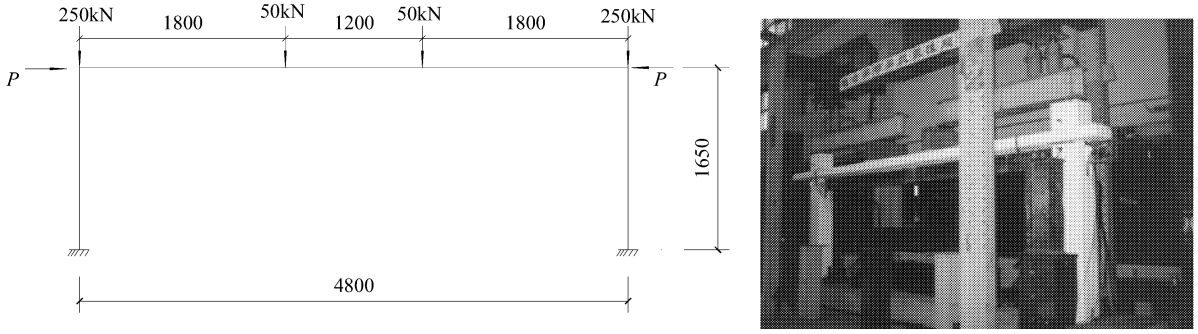

Figure 3. Loading of frames

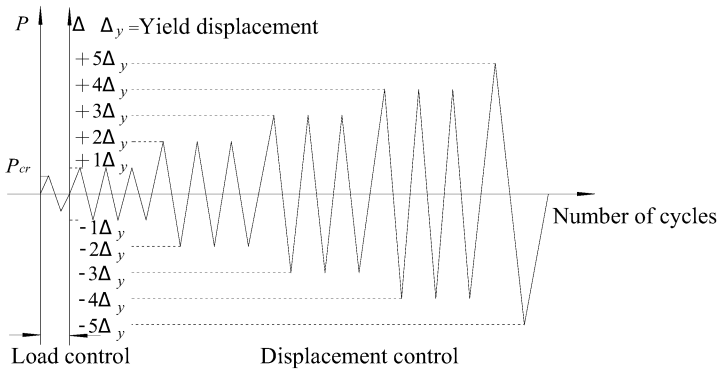

Figure 4. Loading history (Δ_y=H/400; H is the height of column)

The followings were measured and recorded: (1) the lateral load versus lateral drift curves (P-Δ curves); (2) strains of steel beams, longitudinal steel bars in beams and columns, externally prestressed tendons, unbonded prestressed tendons and stirrups in joint cores; (3) slippage between steel beams and concrete slabs; (4) strains of concrete at beam and column ends.

3. TEST OBSERVATIONS

First signs of failure in the two frames were the cracks at top of left columns (as shown in Figure 1) when the lateral load reached 89kN. Compared to specimen syf-1, fewer cracks could be observed in concrete slabs of specimen syf-2 due to the effect of prestressing. Local concrete crushed at bottom of columns in syf-1 when the lateral drift reached $8\Delta_y$, while concrete crushed at bottom columns of syf-2 when the lateral drift reached $10\Delta_y$. For specimen syf-1, concrete spalled at joint cores and column roots. Further slippage was observed between steel beams and concrete slabs. However, concrete spalled at joint cores in syf-2 when the lateral drift reached $14\Delta_y$. Conclusions could be drawn that the specimen syf-1 failed earlier than syf-2. Slippage of the steel beams from the concrete column in syf-1 was greater than that of in syf-2.

It can be observed that failure patterns of the two frames are characterized by first hinging in composite beam ends and then the column ends. Figure 5 and Figure 6 show failures of the two frames.

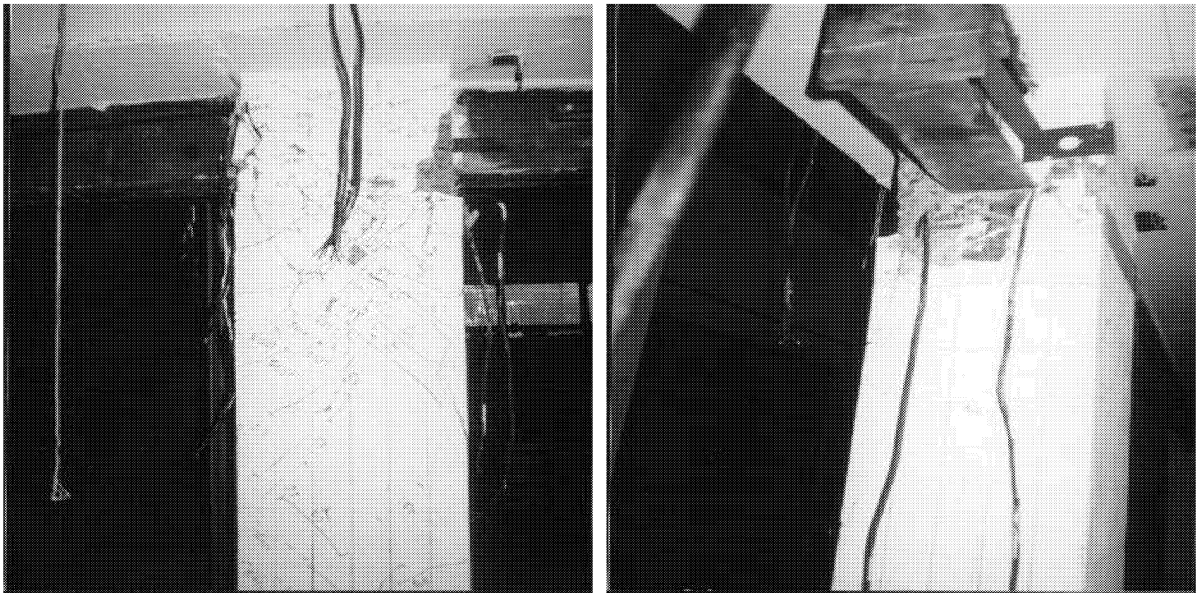

Figure 5. Failure of frame joints

Figure 6. Failure of frame columns

4. TEST RESULTS AND ANALYSIS

4.1 Hysteresis curves

Lateral load versus lateral drift (P-Δ) curves of the two frames are shown in Figure 7. Here, P and Δ are lateral load and lateral displacement at top of frames during testing. It could be observed that hysteresis curves of the two frames are quite similar. Relationship between lateral loads and lateral drift are basically linear before first cracking in frames. Very little residual deformation could be observed, displaying that the two frames are still in elastic ranges at this stage.

Hysteresis loops become curved after cracks occur in frames. Slopes of the two hysteresis curves degrade with increasing lateral drifts. The hysteresis areas become larger gradually. This is called the elasto-plastic stage of the two frames with stiffness degrading in both frames. One of the attributed factors to stiffness degradation is the cumulated damage during the cyclic displacement

reversals. The increasing speed of the lateral loads reduces with increasing lateral drifts. Shapes of hysteresis curves for the two frames in a single loading cycle are quite similar to parallelograms due to hysteretic characteristics of steel beams under cyclic loads.

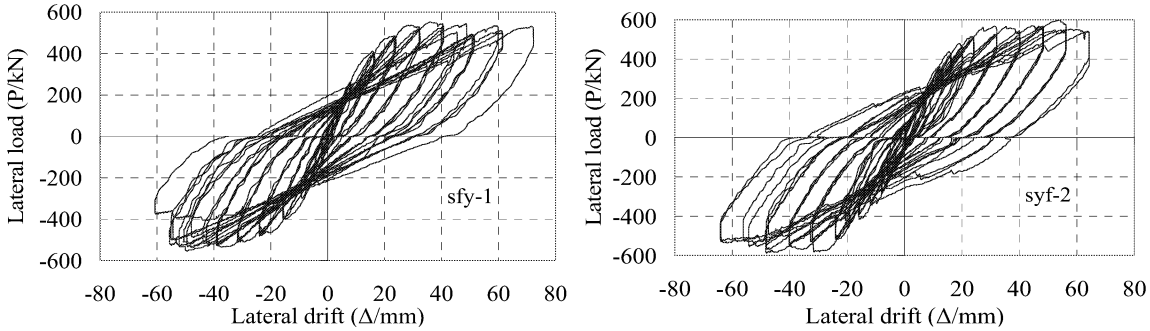

Figure 7. P-Δ curves of the two composite frames

4.2 Skeleton curves

As shown in Figure 8, the two specimens undergo the three point response when subjected to cyclic displacement reversals, namely they are the cracking point, the yield point and the maximum load point. Skeleton curves of both frames are basically linear before the first cracking in frames. After cracking, the load versus lateral displacement relationship becomes curved. This process continues until yielding of the frame, in which an obvious inflexion point could be observed in the skeleton curves. Stiffness of the frames degrades until curves reach the maximum load point. However, loads degrade gradually after the maximum load point.

Skeleton curves of the two frames are quite similar. The applied prestressing and the failure of composite beams have little effect on global seismic behavior of the frame, which can be attributed to the failure patterns of the two frames.

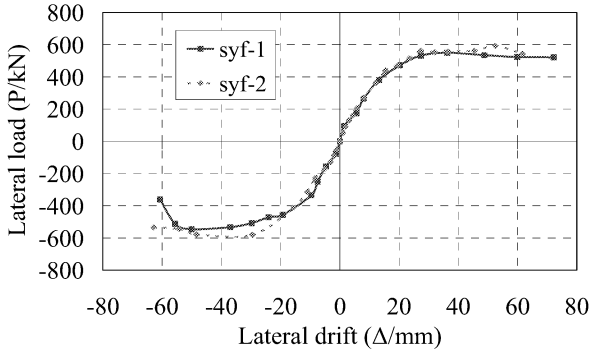

Figure 8. Skeleton curves of frames with composite beams

4.3 Hysteretic model

A four-linear hysteretic model with descending parts and pinching pivot points for hysteresis analysis of the composite frames is obtained on the basis of hysteresis curves, skeleton curves and characteristic loads of the two frames. Figure 9 shows the four-linear hysteretic model for the composite frames, which is characterized by the following hysteretic rules:

(1) The loading stiffness is set equal to the initial stiffness before yielding. Stiffness degradation and residual deformation are not taken into account during unloading.

(2) From the cracking point and the yield point, loading stiffness is assumed to be equal to the post-cracking stiffness and unloading points to the cracking point in the opposite direction.

Stiffness degradation and residual deformation are considered at this loading process.

(3) Between the yield point and the ultimate point, loading stiffness is set to be equal to the post-yield stiffness and assumed to be negative after the ultimate point. The unloading stiffness is taken as K by the reduction factor β. Here, K is the stiffness from the yield point to its corresponding cracking point at opposite direction of loading. The reduction factor is defined as:

$$\beta = (\frac{\Delta_y}{\Delta_m})^{\nu} \tag{2}$$

Where Δ_y is the yield displacement, Δ_m is the previous maximum displacement and ν is the factor obtained from the test results. Then the post yield stiffness K_{py} is defined as:

$$K_{py} = \beta \cdot K \tag{3}$$

(4) The reloading paths in the opposite direction of loading after post-yield unloading directly takes along a line which connects the point at which unloading was completed with the cracking point in the opposite direction of loading provided that the maximum previous displacement in the opposite direction of loading do not exceed the cracking displacement (Δ_{cr}). It can be observed that all load-displacement paths tend to cross at approximately the same point in two loading directions (the points corresponding to the loads P_1 and $-P_1$, as shown in Figure 9). We define these two points as the pinching pivot points. The reloading path takes along a line which connects the point at which unloading was completed with the pinching pivot point in the opposite direction of loading provided that the maximum previous displacement in the opposite direction of loading is between the cracking displacement (Δ_{cr}) and the displacement (Δ_1) corresponding to the pinching pivot point. Provided that the maximum previous displacement in the opposite direction of loading is greater than the displacement corresponding to the pinching pivot point, the reloading paths in the opposite direction of loading takes along a line which connects the following three points: the point at which unloading was completed, the pinching pivot in the opposite direction of loading and the point on the skeleton curve in the opposite direction of loading.

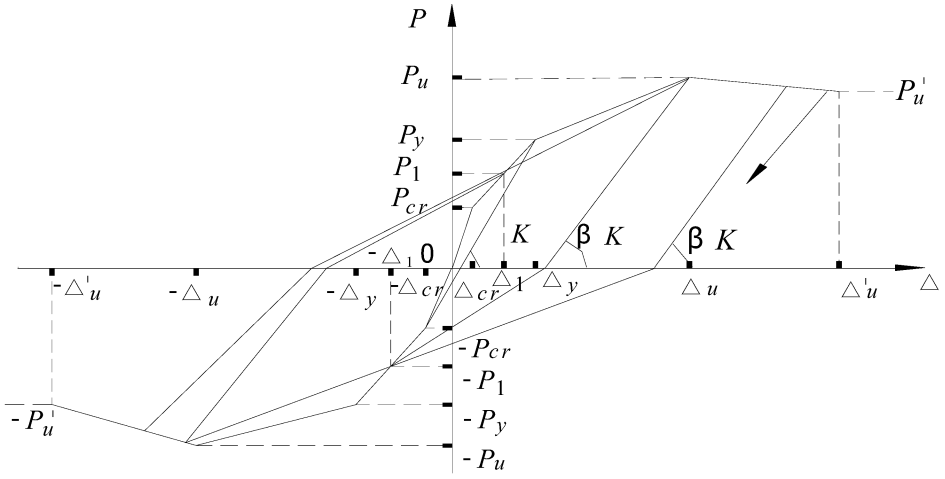

Figure 9. Hysteretic model for composite frames

4.4 Failure mechanisms

Failure of the two frames under cyclic displacement reversals is finally governed by crushing and spalling of concrete at top and bottom of columns. In comparison with the top of columns, the

column roots suffered more serious failure.

Figure 10 shows the sequences of plastic hinge formation in the two composite frames during the testing. Comparisons between the test results and the analytical results calculated by the PK software [11] are presented in Table 4. It can be observed that the tested sequences are in accordance with the results calculated by PK.

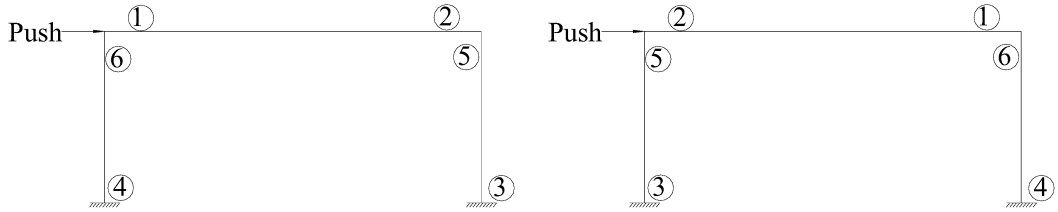

Frame with common composite beams

Frame with externally prestressed composite beams

Figure 10. Sequences of plastic hinge formation in the two frames

Table 4. Lateral loads corresponding to hinge formation

Locations of plastic hinges	Syf-1		Syf-2	
	Experimental values (kN)	Analytical values by PK (kN)	Experimental values(kN)	Analytical values by PK (kN)
Hinging at the beam ends	212	226	194	186
Hinging at the column ends	475	317	501	305
Failure loads	542	417	577	409

The sequences of plastic hinge formation in the two frames are quite similar. Both frames first develop hinge at beam ends and then at root and top of columns. This sequence of hinge formation is in accordance with the strong-column weak-beam criterion, which requires that the flexural strength of columns must be larger than that of the beams. Both frames fail by crushing of concrete at column roots and have been designed to achieve the strong-column weak-beam requirements. This kind of failure mechanism provides the frames with better ductility and larger energy dissipation capacity.

4.5 Deformation restoring capacity

In this paper, residual deformation ratio, which is defined as Δ_r/Δ_u, is used as a key index for evaluating deformation restoring capacity of beam specimens. Here, Δ_r is the residual displacement after unloading and Δ_u is equal to the maximum displacement for skeleton curves without descending part or equal to the displacement corresponding to 85% of the maximum loads in descending part of the skeleton curves. Residual deformation and residual deformation ratios of the two composite frames are presented in Table 5.

Table 5. Residual deformation of the two composite frames

Specimens	Syf-1	Syf-2
Residual deformation Δ_r (mm)	46.55	35.90
Maximum deformation Δ_e (mm)	72.30	63.94
Residual deformation ratio Δ_e/Δ_r	0.64	0.56

As shown in the table, residual deformations and residual deformation ratios of specimen sfy-2 are higher than that of sfy-1, which indicates that frames with externally prestressed composite beams

have larger deformation restoring capacities than that with common composite beams.

4.6 Ductility

Ductility coefficient μ is defined as

$$\mu = \frac{\Delta_u}{\Delta_y} \quad (4)$$

where Δ_u is the maximum lateral drift, Δ_y is the displacement corresponding to yielding of frames. The displacements and ductility coefficients of the two frames during testing are listed in Table 6.

As shown in Table 6, ductility coefficients of the two frames are quite close to each other. Failure of the two frames mainly occurs at column ends and beam-column joints. Therefore, the composite beams are not decisive factors to failure of the two frames and the prestressing applied in composite beams has little effect on seismic performance of the frames.

Table 6. Ductility coefficients of the two composite frames

Specimens		Syf-1		Syf-2	
Loading direction (show in Figure 3)		←	→	←	→
Cracking displacement	Δ_{cr} (1/100mm)	208	200	80	88
	Δ_{cr}/H	1/793	1/825	1/2062.5	1/1875
Yield displacement	Δ_y (1/100mm)	2386	2380	2410	2408
	Δ_y/H	1/69	1/69	1/68	1/69
Ultimate displacement	Δ_u (1/100mm)	7220	7230	6418	6394
	Δ_u/H	1/23	1/23	1/26	1/26
Ductility coefficient (μ)	Δ_u/Δ_y	3.04	3.04	2.66	2.64

4.7 Energy dissipations

The energy dissipated during a single load cycle is calculated using the Trapezoid Rule to determine the area within lateral load (P) versus lateral drift (Δ) curve. The amount of energy dissipated in the two composite frames is depicted in Figure 11. The following conclusions could be drawn from this figure:

(1) At the early period of loading, the loading paths are nearly linear and little amount of energy has been dissipated in the two frames.

(2) The energy dissipation capacity of the two frames increases with increasing displacements. However, the dissipated energy keeps on decreasing in the three load cycles with identical lateral displacements due to cumulated damage during testing.

(3) The energy dissipation curves of the two frames are very close to each other at initial loading stages.

(4) When the lateral drifts are equal to or higher than $6\Delta_y$, more energy has been dissipated in syf-2 in comparison with that in syf-1.

(5) The amount of energy dissipated in sfy-1 remains as a constant during the loading cycles

with lateral drifts of $12\Delta_y$ and $14\Delta_y$. However, no similar phenomenon occurs in syf-2. The reason is that larger slippage is observed between steel beam and concrete slab in syf-1, which affects the energy dissipation capacity of frames with common composite beams.

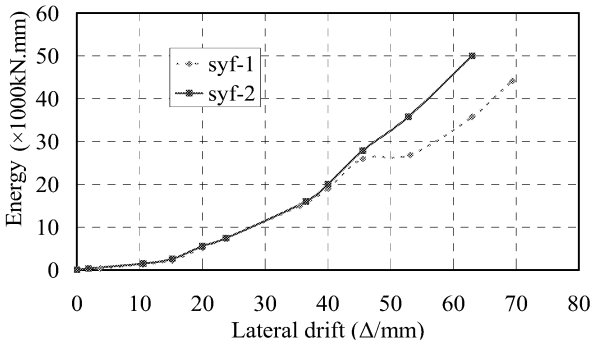

Figure 11. Energy dissipation

4.8 Hysteresis analysis

A modified program based on the FEM theory (Xue & Zhang [12]), simulating the hysteretic behavior of the composite frames, is proposed in the paper. Note that both the nonprestressed and prestressed composite beam elements are incorporated in this program.

The material nonlinearity, geometric nonlinearity and prestressing are main factors that affecting the inelastic response of composite frames with externally prestressed composite beams. The above factors are considered in the proposed program, which is proven to be a better way for full-range analysis of the prestressed composite frames. As shown in Figure 12, each frame is discretized into 20 elements, 5 for a column and 10 for a composite beam. The layered-section approach is employed for element analyses. As shown in Figure 13, the composite beam section is discreted into twenty-three slices: five for concrete, fourteen for steel beams, one for prestressed tendons in steel beams, one for unbonded prestressing tendons in concrete slabs and two for top and bottom longitudinal steel bars in concrete slabs.

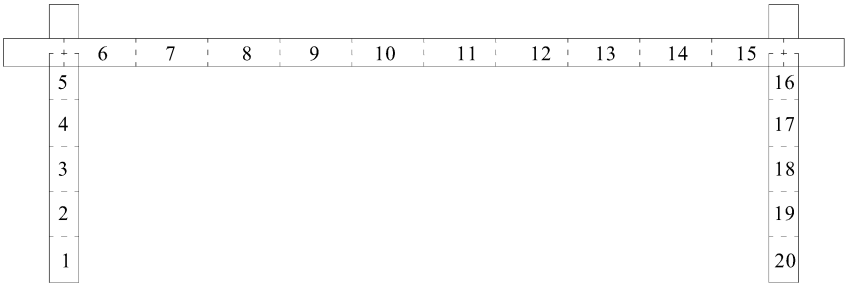

Figure 12. Element discretization for frames

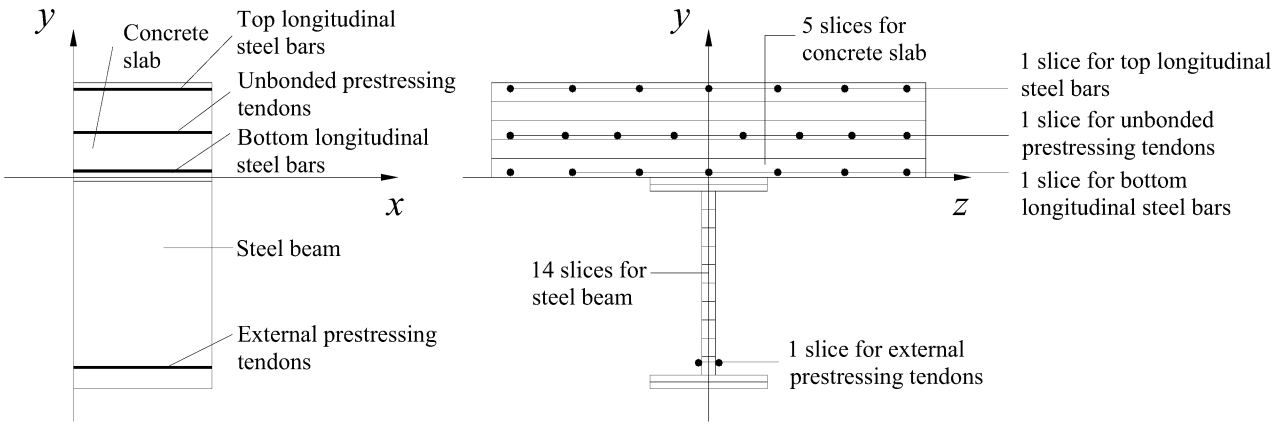

Figure 13. Discretization for composite beam sections

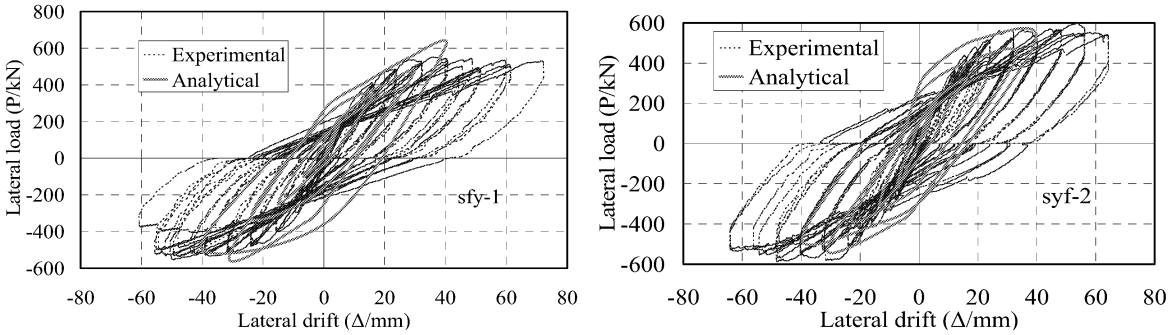

Figure 14. Comparisons of experimental and analytical P-Δ curves for the two frames

Comparison of lateral loads versus lateral drifts curves between experimental and analytical results are shown in Figure 14. By comparing experimental and analytical results of hysteresis curves for the two frames, the following conclusions can be drawn with:

(1) At the early period of the loading, the experimental and the analytical curves are in good agreement.

(2) At the last period of loading, the experimental and the analytical curves are not in good agreement with each other. Deviations of the two curves become larger with increasing displacements. However, their experimental and analytical ultimate loads are similar.

5. CONCLUSIONS

From the studies described in this paper, we can draw the following conclusions:

(1) During testing, plastic hinges first form at beam ends and finally at top and bottom of columns. Failure patterns of the two frames are dominated by crushing and spalling of concrete at top and bottom of columns. More serious failure occurs at bottom of columns. The beam sideway mechanism indicates that the seismic performance of the frames has been significantly improved by the composite beams.

(2) Hysteresis curves for the two frames are relatively full during cyclic loading. Shape of hysteresis loops for the two frames is quite similar, indicating that prestressing applied in composite beams has little influence on seismic behavior of frames.

(3) Displacement ductility coefficients of the two frames are quite close to each other. Tests also show that frames with prestressed composite beams have better deformation restoring capacities.

(4) The amount of energy dissipated in the two frames during the early period of the testing is nearly the same. However, more energy has been dissipated in the frame with externally prestressed composite beams in comparison to that with common composite beams. This can be due to the slippage between the steel beams and the concrete slabs in the frame with common composite beams.

(5) A modified program is proposed and employed for hysteresis analysis of the two composite beams.

(6) Based on investigation of failure patterns, hysteresis curves, ductility and energy dissipation capacity of the two frames, conclusions could be drawn that seismic performance of the two frames could be significantly improved by the composite beams.

ACKNOWLEDGEMENTS

Support for this research by the Shanghai Development Foundation of Science and Technology under Grant No. 992012044 and the "Shu Guang" project supported by Shanghai Municipal Education Commission and Shanghai Education Development Foundation.

REFERENCES

[1] Kennedy, J.B. and Grace, N.F., "Prestressed Continuous Composite Bridges under Dynamic Load", J. Struct. Div., ASCE, 1990, 116(6), pp.1660-1678.

[2] Kocsis, P., "Guidelines for Flexural Design of Prestressed Composite Beams", J. Struct. Div., ASCE, 1990, 117(11), pp.3548-3549.

[3] Ayyub, B.M., Sohn, Y.G. and Saadatmanesh, H., "Prestressed Composite Girders. II : analytical study for negative moment", J. Struct. Div., ASCE, 1992, 118(10), pp.2763-2783.

[4] Li, W.L., Albrecht, P. and Saadatmanesh, H., "Strengthening of Composite Steel-Concrete Bridges", J. Struct. Div., ASCE, 1995, 121(12), pp.1842-1849.

[5] Nie, J.G. and Shen, J.M., "Experimental and Analysis of Actual Shear Capacity of Shear Connectors in Composite Steel-Concrete Beams", Journal of Building Structure, 1996, 117(2), pp.3-9. (in Chinese)

[6] Asta, A.D and Dezi L., "Nonlinear Behavior of Externally Prestressed Composite Beams: analytical model", J. Struct. Div., ASCE, 1998, 124(5), pp.588-597.

[7] Nie, J.G., Yu, Z.L. and Ye, Q.H., "Seismic behavior of composite steel-concrete beams", Journal of Tsinghua University, 1998, 8(10), pp.35~37. (in Chinese)

[8] Xue, W.C., Li, K. and Li, J., "Experimental Studies of Steel-Concrete Composite Beams under Low Reversed Cyclic Loading", Journal of Earthquake Engineering and Engineering Vibration, 2002, 22(6), pp.65-70. (in Chinese)

[9] Thermou, G.E., Elnashai, A.S., Plumier, A. and Doneux, C., "Seismic design and performance of composite frames", Elsevier Ltd, Journal of Construction Steel Research, 2004, 60(1), pp.31-57.

[10] Bursi, O.S., Sun F.F. and Postal, S., "Nonlinear analysis of steel-concrete composite frames with full and partial shear connection subjected to seismic loads", Elsevier Ltd, Journal of Construction Steel Research, 2005, 61(1), pp.67-92.

[11] www.pkpm.com.cn

[12] Xue, W.C. and Zhang, Z.T,. "Method and Application in Nonlinear Full-Range Analysis of Reinforced Concrete", Journal of Computational Mechanics, 1999, 16(3), pp.334-342. (in Chinese)

OPTIMIZATION OF GROOVE DESIGN IN THICK PLATES WELDING

Jia Liwei, Zhou Hongbin and Zhang Mingli

Civil Engineering and Mechanics Institute , YANSHAN University，
Qinhuangdao, Hebei province,P.R.China,066004
Tel: 0335-8067926
Fax: 0335-8057101
Email : joanajia@sohu.com

ABSTRACT: Groove design affects thick plates' residual stress distribution seriously. So optimization of groove design in thick plates' welding is an important work. In order to do this work better we use finite element method to quantitatively evaluate the effects of groove design. Groove design plays a very important role in residual stress distribution. Although we may butt weld two thick plates together by several kinds of groove design, the final residual stress distribution will be different.

In this paper we use three kinds of groove design to butt weld two same thick plates together. Thickness of the plate is 25mm. Finite element method has been employed to evaluate the final residual stress distribution. Utilizing of ANSYS code is efficient when we try to find the residual stress distributions by finite element method. Some functions of ANSYS such as "couple field" and "element birth and death" are adopted. Temperature related thermophysical material properties are considered. Some necessary measurements should be used to prevent convergence problems in this nonlinear analysis procedure.

The results suggest clearly that different groove design induces different residual stress distribution. We should take care of groove design before welding. Also numerical analysis of residual stress can help us to estimate residual stress distribution efficiently. At last we give some suggestions about thick plates groove design.
Keywords: residual stress(RS), finite element method(FEM), thick plate, groove design(GD), weld

INTRODUCTION

When steel structures are welded, RS is induced by the non-uniform temperature distribution. We have find GD has obvious effects on RS distribution especially in the through thickness dimension. But it is hard to measure the stress in through thickness dimension. FEM can help us knowing it better. We use a butt weld between two thick plates as an example. There are some forerunners in the early 1970s such as Kamichika[6] and Friedman[2].From1990, numerical simulation of weld process boomed. Goldak[4], Fricke[3],and Buchmayr ,Ping Dong [10]etc. have developed the process to a advanced level than before.[5]It has been accepted that FEM is more flexible than experiment methods. It is also accurate enough.

We choose a 25mm-thickness plate model because 25mm is relatively common thick in welding. Meanwhile 25mm thickness can not only present characteristics of thick plates welding but also save computing time than thicker plates such as 30mm. We make an assumption that the model is symmetric. Radiation and convection are considered. But we ignore the effects of phase transformation as they have relatively small effects on the final stress result. Three kinds of GD in this paper are: double Y, double V and single Y. Both first welded sides and second welded sides are in single pass in order to save computation sources. Checks have been implicated after thermal analysis to ensure the validity of thermal field. In order to make the RS comparisons equitable we try to make total heat input of each sample is same.

After FEM analysis we get all kinds of stresses, including longitudinal (Lon) stress, transverse (Tran) stress and perpendicular (Per) stress, in the specimen detailedly. RS' comparisons have been made between different types of GD. RS comparisons are shown clearly. From these results we can make an optimization of GD in thick plates welding.

FINITE ELEMENT MODEL

Geometry and Mesh

GD samples are shown in Figure 1.

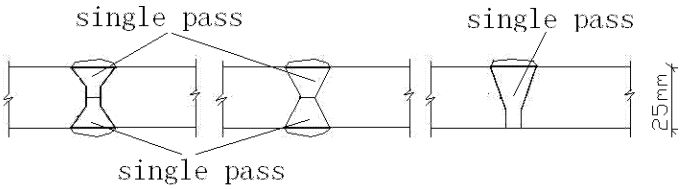

Figure 1: Three types of GD used to butt two plates together

It is accepted that temperature distribution is symmetrical about the weld center area. We also assume that the sample is constrained symmetrically about the weld center area. Using of symmetric model is reasonable. So only half of the model is analyzed. It is should be noticed that the real constrains of the sample should be symmetrical otherwise the half model should not be employed. In thermal analysis adiabatic condition can be used to describe symmetric area. In mechanical analysis ANSYS offer special symmetric boundary conditions. Magnitude of RS is distinctly higher in weld zone and heat affected (HAC) zone. In this example total extent of weld zone and HAC zone on either side of the weld is about 10mm~20mm. Division of the mesh in the weld zone and HAC zone should be fine enough to ensure convergence of the analysis. Of course the longer the distance from the weld zone the coarser the division can be allowable [9]. The FEM geometry and the mesh are shown in Figure 2.

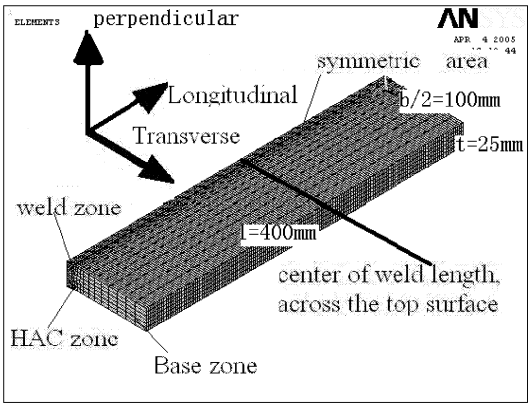

Figure 2: Geometry and the Mesh

Properties of Material

Materials in weld zone experience transient heating and cooling in a short time. Fig 3 shows temperature variation of point1.

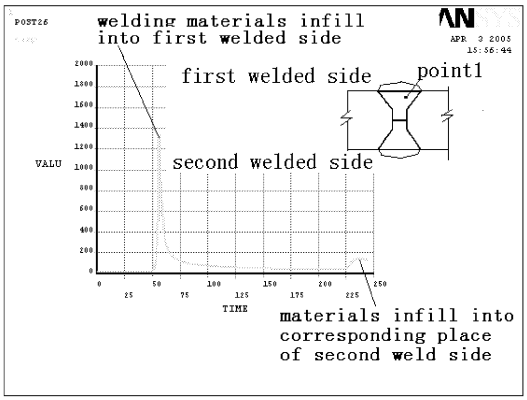

Fig3 Temperature Variation of Point1

Temperature rises instantaneously to the maximum value as soon as the welding materials infilling into this place. Then temperature reduces instantaneously to a lower level. When materials infilling into corresponding place of the second weld side, temperature of point1 rises. The stress release is usually approximated by specifying temperature dependent material properties [13].So properties of material are all temperature dependent. However, thermophysical material properties in high temperature are difficult to find. Thermophysical material properties used in this paper are according to David etc [1], except coefficient of convection is same as [8]. Von-Mises yield criterion and associate flow rule with kinematics' hardening were assumed to consider the Bauschinger effect. Materials in weld zone are evenly matched with the base material.

Other key techniques

This analysis involves heat analysis and mechanical analysis. A nonlinear transient thermal analysis is carried out as the first solving step. A stress analysis then developed. The results of thermal analysis are applied to the model as loading.

Function of element birth and death is used. All elements in weld zone of the FEM model are dead because materials in weld zone do not exist before welding. Activation of elements in the model simulates accumulating of materials in weld zone.

Time interval of every step and substep must be minimized otherwise the solution will not convergence. Maximum time interval of one substep should be less than 0.1s when heat source is moving on the weldment. It can be prolonged when cooling. [9]

RESULTS AND DISCUSSION

In thermal analysis a temperature field is obtained, and it is used as a thermal loading in the subsequent stress analysis. Distribution should be relatively stable and the isotherm obtained from thermal analysis should be in accordance with [11] and [12]. Fig4 shows an isotherm of a stochastic time.

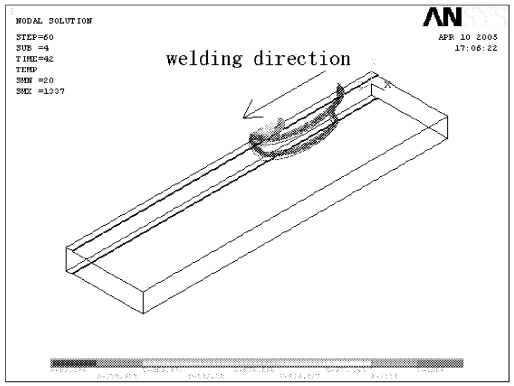

Fig4 .An Isotherm of a Stochastic Time

RS results proposed in this paper have the same trend line as provided by Hill, Michael R [5]. So it can be concluded that the FEM results are acceptable. Both surface RS and through thickness RS are shown in Fig.5.

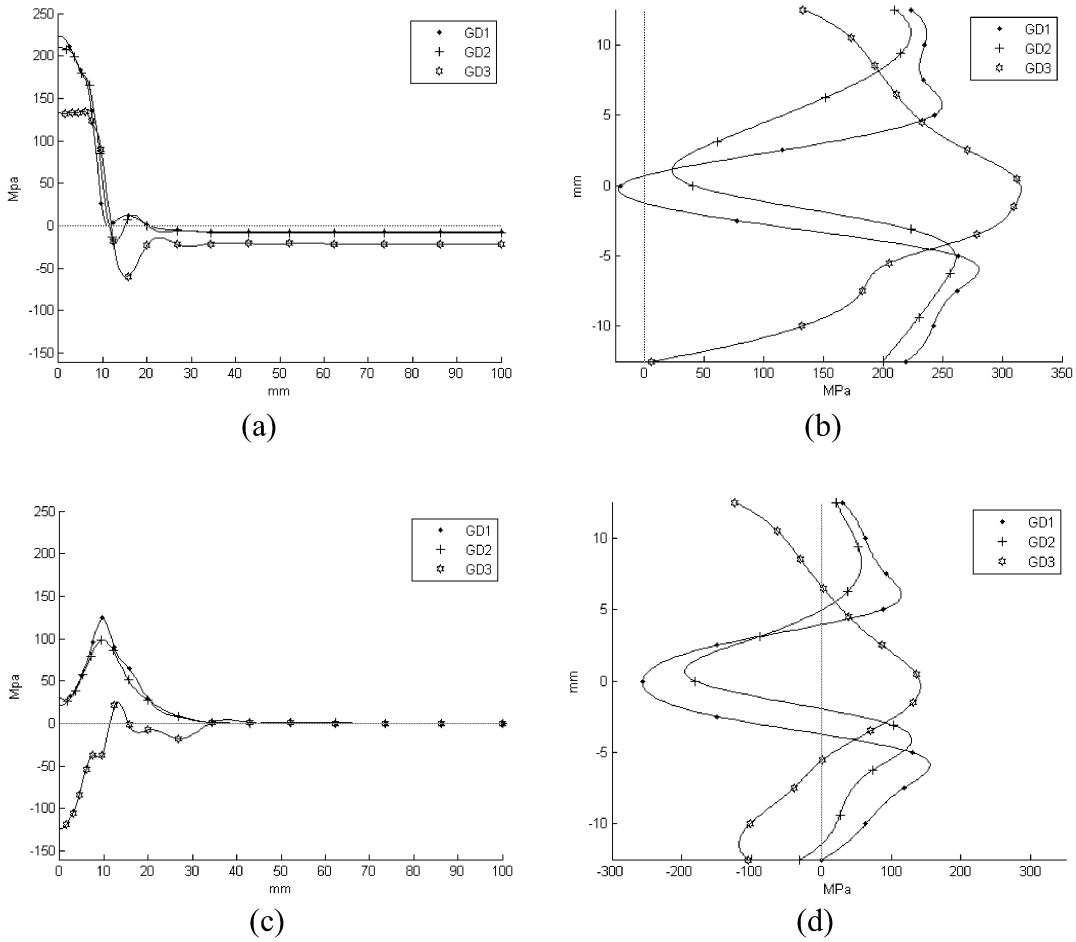

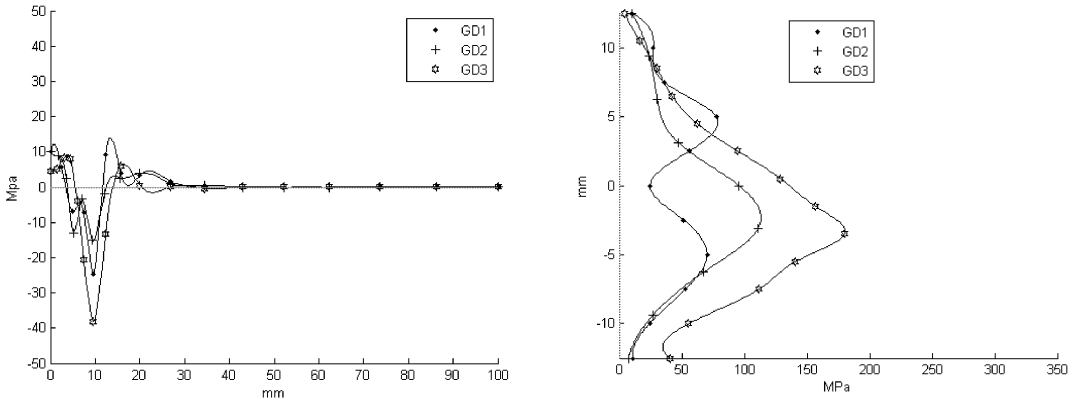

(e) (f)

Fig. 5 RS distribution

(a) Lon RS at the centre of the weld length, across the top surface

(b) Lon RS at the centre of the weld length, through the thickness

(c) Tran RS at the centre of the weld length, across the top surface

(d) Tran RS at the centre of the weld length, through the thickness

(e) Per RS at the centre of the weld length, across the top surface

(f) Per RS at the centre of the weld length, through the thickness

Fig5 shows that Lon stress is higher than other kinds of RS. It may be occurred in steel structure welding that a branch of stress even over yield stress [7] as it shows in Fig5.b.

Stresses across the top surface of GD1 and GD2 have similar trend lines. But Tran RS of GD3 in weld center is compressive which is different with GD1and GD2.

As far as Lon and Tran stresses through thickness are concerned, differences are remarkable. Lon and Tran stresses of GD1 and GD2 through thickness are large on the surface .And they reduce to a lower value even become to be compressive inside thickness. But there are obviously differences if we talk stresses quantitatively. GD1 has a thoroughly contradict trend line with GD1 and GD2.

Compared with the other kinds of RS ， Per stress is lowering. But there are some special requirements for thick plates' sustainable ability. The reason is thick plates' through thickness material properties are worse than thinner plates. So Per RS should be considered in thick plates welding. It is clearly that Per RS of GD3 is higher than Per RS of GD1 and GD2.Also stress gradient of GD2 and GD3 are hardener than GD1.

CONCLUSION

It is of fundamental importance for accurate and reliable structural integrity assessments of components and structures. While compressive RS may bring about some benefit to whole welding structure, tensile RS may induce some disadvantage to components. In this paper we investigate the GD effects on RS distribution.

There are many kinds of GD can be used to butt two same plates together. We should consider characteristic of loads and RS distribution simultaneously. It is better that stresses induced by loads and RS can offset each other. Multi-pass is better than single-pass for stress gradient can be reduced by it.

GD plays an important role in thick plate's RS distribution. It is better to simulate distribution of RS before welding and choose a suitable GD. We should take suitable GD in different engineering conditions.

REFERENCES

[1] David,Atteridge,M.Becker,K.Khan,L.Meekisho,B.Tahmasebi,andL.Zhang,"Finite element modeling of residual stresses in electroslag butt welds", http://ntl.bts.gov/ sec508/finite.pdf ,2000,pp.52-55

[2] Friedman, E., 1975, ''Thermomechanical Analysis of the Welding ProcessUsing the Finite Element Method,'' ASME J. Pressure Vessel Technol., 97,Aug., pp. 206–213.

[3] Fricke, S., Keim, E., and Schmidt, J., 1998, "Numeric Determination of Residual Weld Stresses," Proceedings, ICES'98, October 7–9, Atlanta.

[4] Goldak, J, et al., 1998, "Progress and Pacing Trends in Computational WeldMechanics," Proceedings, ICES'98, October 7–9, Atlanta, Atluri, S. N., ed.

[5] Hill, Michael R. and Nelson, Drew V,"Determining residual stress through the thickness of a welded plate", Proceedings of the 1996 ASME Pressure Vessels and Piping Conference. ASME, New York,1996,vol 327, pp.29-36

[6] Kamichika, R., Yada, T., and Okamoto, A., 1974, "Internal Stresses in ThickPlates Weld-Overlaid with Austenitic Stainless Steel ~Report 2!," Trans. Jpn.Welding Soc., 5, No. 1, Apr.

[7] LiGuoQiang,"DuoGaoCengJianZHuGangJieGouSHeJi",ZHongGuoJianZHuGongYe press,2004,pp.35

[8] Li Jiang,"SanWeiHanJieReYingLiHeCanYuYingLiYanHuaXuNiFenXiJiSHuYanJiu", Dissertation for the Master Degree in Engineering GuangXi university,2002,pp.66-75

[9] Li Ying min.Cui Baoxia and Su Shifang,"Ji Suan Ji Zai Cai Liao Jia Gong Ling Yu Zhong De Ying Yong ",China Machine Press,2001,pp.74

[10] P.Dong and F.W.Brust."Welding residual stresses and effects on fracture in pressure vessel and piping components: a millennium review and beyond" Journal of Pressure Vessel Technology. 2000 ,vol122:3,pp329-338

[11] WangJianHua,"Han Jie Shu Zhi Mo Ni Ji Shu Ji Ying Yong" ,Shanghai Jiao Tong University Press ,2003,pp.156

[12] ZhangWenyue,"Han Jie Chuan Re Xue.", China Machine Press,1987,pp.11-17

[13] Zhang, X. Richard and Xu,Xianfan,"Finite element analysis of pulsed laser bending:The effect of melting and solidification.". Journal of Applied Mechanics, Transactions ASME, 2004,vol.71:,3,pp.321-326

MODELING OF THE SEISMIC RESPONSE OF CONCENTRICALLY BRACED STEEL FRAMES USING THE OPENSEES ANALYSIS ENVIRONMENT

[1]Antonio Agüero, [2]Carmen Izvernari and Robert Tremblay

[1]Departamento de mecánica de los medios continuos y teoría de estructuras
ETS de ingenieros de Caminos, Canales y Puertos, Universidad Politécnica de Valencia
Campus Vera s/n, 46020 Valencia, España, Email: anagra@mes.upv.es

[2]Department of Civil, Geological and Mining Engineering
Ecole Polytechnique of Montreal, Montreal (QC) Canada H3C 3A7

ABSTRACT: A study was performed to investigate the possibility of modeling the seismic inelastic cyclic response of steel bracing members using the OpenSees computer program. The study focuses on bracing members made of rectangular and square steel tubes. The efficiency and the accuracy obtained from the force (FBE) and displacement (DBE) based elements are first compared. A co-rotational framework is used to model the nonlinear geometric behavior, and inelasticity is accounted for through fiber discretization of the cross-section together with bi-linear or Giuffré-Menegotto-Pinto hysteretic material response. FBE and DBE models are compared for various combinations of number of elements along the brace length, number of integration points along the element length, number of fibers used to define the cross-section, and amplitude and number of displacement increments. The influence of brace slenderness and displacement protocol on the accuracy of the models is examined. Model predictions are also compared to individual brace and full-scale frame test results. The influence of time step and brace discretization on the dynamic seismic response for a typical braced steel frame is investigated.

Keywords: Displacement based element; Force based element; Braces; Buckling; Yielding; Gusset plate; Frame; Earthquakes; Seismic.

INTRODUCTION

Three types of derivation have been mainly used to study the nonlinear dynamic behavior of three-dimensional structural systems that include beam elements with hysteretic behavior under a predominantly uniaxial state of strain and stress: displacement, flexibility and mixed formulations. Bracing members in braced steel frames are expected to experience several cycles of inelastic buckling and tensile yielding when the structure is subject to strong seismic ground motions (Fig 1). When modeling the behavior of braced frames under seismic loading, the type of brace model and related numerical aspects must therefore be carefully selected such that accurate results can be obtained while minimizing the computation costs.

The Open System for Earthquake Engineering Simulation (OpenSees) (McKenna and Fenves, 2004) is a software framework using finite element methods to develop applications for the simulation of the performance of structural and geotechnical systems subjected to earthquakes. OpenSees is comprised of a set of modules to perform creation of the finite element model, specification of an analysis procedure, selection of quantities to be monitored during the analysis, and the output of results. A large-displacement buckling formulation with a fiber representation of sections incorporated in OpenSees has already been used to reproduce the inelastic cyclic response of steel bracing members (Uriz and Mahin, 2004). The objective of this study is to develop guidelines for modeling the non-linear seismic response of steel braces using this type of formulation. The displacement and force based formulations are compared with consideration of the number of elements, integration points, and fibers on the evaluation of brace response parameters.

The accuracy of the FBE model for different brace slenderness and applied loading protocols is examined. FBE model predictions are then compared to the results of tests performed on 4 individual brace tests. Full-scale tests results are then used to evaluate the brace modeling technique with rotational springs simulating end restraint conditions imposed by the gusset connections. Finally, the accuracy of the proposed brace model is investigated for the dynamic seismic analysis of a single-storey X-braced steel frame.

FORCE BASED ELEMENTS VS DISPLACEMENT BASED ELEMENTS.

In the force based element (mixed formulation), compatibility and equilibrium equations are satisfied in a weak sense. The implementation is based on the Hellinger-Reissner (H-R) variational principle with the weak form of the equilibrium equations: $\iiint \sigma \cdot \delta\varepsilon^T \cdot dV - \delta d^T \cdot F_{EXT} = 0$. The strains $\{\varepsilon\}$ are derived from the displacements $\{d\}$ using $\varepsilon_1 = L \cdot d$, where $\{L\}$ is the differentiating operator, and from the stresses $\{\sigma\}$ using $\sigma = C \cdot \varepsilon_2 \rightarrow \varepsilon_2 = C^{-1} \cdot \sigma$, where C is the material constitutive laws. The weak form of the compatibility equation $\iiint W \cdot (\varepsilon_1 - \varepsilon_2) dV = 0$ is used, where $\{W\}$ is a weight residual function and, hence, the H-R principle leads to: $\iiint \sigma \cdot \delta\varepsilon^T \cdot dV - \delta d^T \cdot F_{EXT} + \iiint W \cdot (\varepsilon_1 - \varepsilon_2) dV = 0$. In the displacement based formulation, equilibrium equations are satisfied in a weak sense, with a displacement field assumed in each element. The strains are derived from the displacements using $\varepsilon_1 = L \cdot d$, and the stresses from the strains with $\sigma = C \cdot \varepsilon_1$. The weak form of the equilibrium equation takes the form: $\iiint \sigma \cdot \delta\varepsilon^T \cdot dV - \delta d^T \cdot F_{EXT} = 0$.

A first parametric study was performed to compare the efficiency of both element formulations. A co-rotational framework was used to model the nonlinear geometric behavior, and spread of inelasticity was accounted for through fiber discretization of the cross-section with bi-linear hysteretic material behavior with isotropic and kinematic strain hardening. In the analyses, an initial sinusoidal out-of-straightness with maximum amplitude of $1/500^{th}$ of the brace length was considered, as prescribed in standards for the fabrication of structural tubing (e.g., ASTM, 2003). The tolerance was set to 10^{-7} and a displacement step size of 0.1 mm was used. The analyses were performed for the brace specimen S2A tested by Tremblay et al. (2003). This brace had a rectangular tubular cross-section (HSS 102x76x4.8) with a steel Young's modulus, E, of 185 GPa and steel yield stress, F_y, of 381 MPa. The slenderness parameter of the brace, $= (P_y/P_{cr})^{0.5}$, was equal to 1.56, where P_y and P_{cr} are the squash load and the elastic buckling load of the brace, respectively. The number of elements along the brace length, n_e, was varied (n_e = 4, 8, 16, 24, and 32), as well as the number of integration points per element, n_i (n_i = 4, 5, and 6). A total of 16 fibers were used for modeling the cross-section, as illustrated in Fig. 2a. Typical hysteresis responses obtained from computation are shown in Fig. 2b.

The computational work was performed with a Pentium 4 with 2.8 GHz and 1.0 Gb RAM. The computation time is given in Fig. 3a as a function of the number of elements and integration points. As shown, the computational effort increases nearly linearly with the number of elements but is not influenced by the number of integration points. For this particular example, it was found that the force based formulation required between 40% and 50% more calculation time than the time needed with the displacement based formulation. In the parametric study, it was observed that the sequence of analyses had an influence on the computational time when using the Tcl programming language. This was not the case when the Python programming language was used to control a

series of OpenSees analyses.

The mean quadratic error on the force developed by the brace element, *MQE,* was determined using $MQE = [\quad (P_i\text{-}P_{ie})^2/n]^{0.5}$, where P_i are the force estimates at every calculation step with a given (n_e, n_i) combination and P_{ie} are the force values determined with $n_e = 32$ and $n_i = 6$, and n is the number of calculation steps. The error *MQE* is expressed as a percentage of the brace yield load, P_y. Figure 3b shows the variation of *MQE* with the parameters n_e and n_i. The numerical results are presented in Table 1. As anticipated, the error decreases with the number of elements. Again, the number of integration points had a limited impact on the quality of the results. The figure clearly shows that a force based formulation leads to more accurate results. Such a convergence is in agreement with previous studies (e.g., Barbato and Conte, 2004).

PARAMETRIC STUDY USING THE FORCE BASED FORMULATION

Influence of modeling parameters

A second parametric study was carried out using the forced based formulation. The influence of brace slenderness was examined by carrying out analyses on three braces with different cross-sections and effective lengths. The properties of the braces are given in Table 2. All members were tubular steel shapes with square cross-sections made of ASTM A500 grade C steel with F_y = 345 MPa and E = 200 GPa.

The initial out-of-straightness conditions considered in the previous study were also specified in this second series of analyses. However, the uniaxial Giuffré-Menegotto-Pinto (GMP) steel material with kinematic and isotropic hardening was used to simulate Bauschinger effect under cyclic loading. The properties specified for this model were based on the load-deformation response measured on the core of buckling restrained bracing members subjected to quasi-static cyclic testing (Tremblay et al., 2004). In the GMP model, the transition between elastic to plastic response was characterized by the following parameters: $R_0 = 25$, $cR_1 = 0.925$, $cR_2 = 0.15$, the isotropic hardening parameters were: $a_1 = a_3 = 0.00001$, $a_2 = a_4 = 0.00002$; and the kinematic hardening parameter, b, was set equal to 0.01.

In Fig. 4, the experimental measurements are compared to the analytical predictions from the bi-linear model used in the previous study and the GMP model. As shown, the second model better reflects the cyclic hysteretic behavior of steel material. Figure 5 compares the response obtained using the bilinear and the GMP hysteretic brace model. When compared to typical measured response (see Fig. 1), the later provides a more realistic representation of actual brace behavior with smoother transitions between elastic and inelastic stages.

The test loading protocol proposed for buckling restrained braces (AISC, 2005) was applied in the study: 6 cycles at a brace axial deformation, δ, equal to δ_y, 4 cycles at $\delta = 0.5\ \delta_m$, 4 cycles at $\delta = 1.0\ \delta_m$, and 2 cycles at $\delta = 2.0\ \delta_m$, where δ_y is the axial deformation at yield and δ_m is the brace deformation at design storey drift, $\delta_m = 3.2\ \delta_y$. The modeling parameters that were varied included the number of elements along the brace length (n_e = 4, 8, 16 and 32) and the number of fibers used to define the cross-section, n_f = 8, 12 and 16. Prior to performing the study, preliminary analyses were carried out on the intermediate slenderness brace ($\lambda = 1.0$) with n_i = 3 and 4 (number of integration points per element). No significant differences could be observed for the *MQE* and the total energy dissipated by the brace that were computed with these two n_i values. Therefore the number of integration points was set equal to 3.

A total of 8 response parameters describing the brace hysteresis response were examined: 1) the buckling load at first occurrence of buckling, P_{u0}; 2) the buckling load in the first cycle at $\delta = 1.0\ \delta_m$, P_{u1}; 3) the energy dissipated up to and including the 4th cycle at $\delta = 1.0\ \delta_m$, E_{h1}; 4) the energy dissipated at the end of the test loading protocol, E_{h2}; 5) the brace deformation when developing P_y in the first cycle at $\delta = 1.0\ \delta_m$, δ_{y1}; 6) the compressive resistance at peak negative deformation in the first cycle at $\delta = 1.0\ \delta_m$, P_1; 7) the brace out-of-plane deformation at peak negative deformation in the first cycle at $\delta = 1.0\ \delta_m$, Δ_1; and 8) the brace out-of- plane deformation at peak negative deformation in the first cycle at $\delta = 2.0\ \delta_m$, Δ_2.

The variation of the 8 brace response parameters as a function of n_e and n_f is presented for each brace slenderness in Fig. 6. For each brace slenderness, the results have been divided by the values obtained with the highest level of discretization, i.e. using $n_e = 32$ and $n_f = 16$. Clear trends can be observed from these plots: the quality of the results is maintained when the number of elements is reduced from 32 to 8, but it degrades significantly if the number of fibers is reduced from 16 to 8. For $n_f = 16$, discretizing the brace members with 8 elements instead of 32 elements resulted in errors of only 1% or less for all parameters except for P_{u1} for $\lambda = 1.0$ in which case the error reached 3%. The same trend is observed for other values of n_f. Conversely, the loss in accuracy can reach up to 10% (δ_{y1} for $\lambda = 1.0$) or 5% (other response parameters or slenderness) when n_f is reduced from 16 to 12 and n_e is kept equal to 32. Much larger errors are observed if n_f is reduced further from 12 to 8. It is noted, however, that the stockiest brace is less sensitive to a reduction in the number of fibers (error less than 3% when n_f is reduced from 16 to 12 and n_e is reduced from 32 to 8).

Influence of loading sequence

The analyses on the three bracing members were redone under two additional loading sequences: the quasi-static cyclic test protocol recommended by the European Convention for Constructional SteelWork (ECCS, 1991) and the brace test displacement history that was developed by Tremblay and Bouatay (2002) for braced steel frames exposed to crustal and sub-crustal earthquakes in western Canada (WC protocol). The response under the AISC loading protocol is also considered for comparison. The three displacement sequences are illustrated in Fig. 7. The history of the energy dissipated, E_H, as a function of the cumulated imposed displacement, $\Sigma\delta$, in each loading protocol is used to evaluate the validity of the modeling assumptions. The stockier ($\lambda = 0.5$) and the most slender ($\lambda = 2.0$) braces are examined. Two different models are considered: a simple but still accurate model as per previous studies with $n_e = 8$, $n_f = 16$, and $n_i = 3$, and a more refined model with $n_e = 32$, $n_f = 16$, and $n_i = 4$. As shown in Fig. 7, the simple model predicts equally well the brace energy dissipation capacity, regardless of the model assumptions and the applied loading history. The total energy dissipation capacity is compared in Table 3. Again, negligible differences are found between the two models.

VALIDATION AGAINST BRACE TEST RESULTS

The force based formulation is used to reproduce the hysteretic response of four rectangular HSS bracing members from different test programs. The properties of the braces are given in Table 4. Specimens S2-A and S1QB were tested by Tremblay et al. (2003) while tests on Specimens 1B and 2 were respectively performed by Shaback and Brown (2003) and by Haddad (2004). The cross-sectional flexural properties, I and r, are those associated with the plane of buckling observed in the tests. The $_y$ values are reference yield deformations as defined in each of the studies. Initial out-of-plane imperfections at mid-length of the braces, v_0, as assumed in the analyses, are also

given in the table.

According to current seismic design practice, brace connections must be detailed to allow ductile rotational response upon brace buckling. For single gusset plate connections, end rotations due to out-of-plane brace buckling can be easily accommodated in the gusset plates by introducing a free hinge length between the brace end and the line of restraint (see Fig. 8a). It is recommended that the length of the free hinge region be equal to two times the gusset plate thickness, t_g (Astaneh et al., 1985). This detail was adopted in the three test programs, as shown in Fig. 8b for the tests by Tremblay et al. (2003), and the length L in Table 4 corresponds to the brace length between hinge center lines.

Such a detail induces rotational restraint at the brace ends, and plastic hinging is anticipated in the gusset plates when large brace out-of-plane deformations develop after brace buckling in compression (see Figs. 8b and 8c). Using the flexural stiffness of the gusset plate assembly, C_g, the brace effective length including end restraint effects can be determined from classical elastic stability theory (Chajes, 1974). Table 5 gives the values of C_g for each of the test specimens as well as the resulting slenderness parameters. For these braces, the parameter K varies from 0.75 to 0.93. In view of the key role of the brace effective slenderness on the cyclic hysteretic response of bracing members, these end condition effects must be properly modeled when reproducing brace test results or predicting the brace response in actual building structures. Three different approaches are presented in the following sub-sections to account for the rotational restraint induced by the gusset plates.

Brace model with effective length KL

In the first modeling approach, a pin-ended brace is used with a length equal to the brace effective length KL (see Fig. 8d). In Fig. 9, the predicted response with n_f = 16, n_i = 3, and n_e = 8 is compared to the test measurements for Specimens S2A and 2. Similar results were obtained for the other two test braces or when using a larger number of elements (n_e greater than 8). Hysteretic responses are compared using two set of parameters for the Giuffré-Menegotto-Pinto material model. The curves on the left hand side were obtained with the same parameters as defined in the previous section, i.e. with R_0 = 25 and both isotropic and kinematic strain hardening properties. In the second comparison, the parameter R_0 was reduced to 20 and isotropic hardening was omitted (a_1 to a_4 = 0.0). It can be seen that using a lower R_0 value with more progressive yielding behavior resulted in a better match with the measured response for the post-buckling resistance upon reloading in compression at large deformations. When isotropic hardening was specified, the predicted yield tensile resistance of the braces was found to increase with the number of cycles, which was not the case for the test specimens. As shown, a material model without isotropic hardening seems to be more appropriate. This modified GMP material model is used in the remaining of the paper.

Although the GMP steel model closely reproduces the transition between tension and compression responses, it must be realized that it has inherent limitations such that it will not be possible to exactly characterize brace cyclic inelastic response. For instance, residual stresses are not included in the model. This leads to a generally stiffer response in the first loading cycles with small deformations, as well as a higher compression load at first occurrence of buckling. Local buckling and brace fracture cannot be reproduced either. Therefore, the predicted response would generally be too optimistic near the end of a test, when degradation in strength and stiffness is typically observed due to local buckling and progressive cracking of the cross-section.

The pin-ended brace model of length KL also has drawbacks that may preclude its use in seismic

building analysis. One of these limits is the fact that the length of the brace model does not correspond to the actual brace length in the structure. In the individual brace analyses carried out herein, the test loading protocol was multiplied by K before it was applied to the numerical model. Therefore, the same elastic and inelastic deformation demand could be imposed in both the test and model braces. This cannot be done in a building analysis. The gaps can be filled with additional beam-column elements with same cross-sectional area and infinite flexural stiffness and strength, but the amount of inelastic deformations imposed on the brace portion of length KL would be overestimated. A second main shortcoming of the KL model is the fact the model will always underestimate the out-of-plane brace deformations due to the shorter brace length, as illustrated for Braces S2A and 2 in Fig. 9c. This affects the brace post-buckling compression capacity as well as its resistance upon straightening the brace in tension. Finally, a model based on the effective length cannot capture the energy dissipation that develop at the braces ends through plastic hinge rotations in the gusset plates.

Brace model with end extensions

The problems of the KL model associated with the difference between actual and model brace lengths can be partly overcome by using the model shown in Fig. 8e. In this model, the rotational restraints at the brace ends are included by adding fictitious brace extensions of length L_c at both ends of a brace model having the actual brace length. The out-of-plane displacements at the outer ends of these extensions must be restrained. For simplicity, the flexural stiffness (EI) of the bracing member can be assigned to the extensions. If pinned connections are specified at the outer ends of the extensions, the length L_c can then be taken equal to $3EI/C_g$. The L_c values so computed for the four brace specimens are given in Table 5, and Figure 10 compares the response of Specimen S2A obtained from this model to the test results and the predictions from the KL model. All calculations were carried out with $n_f = 16$, $n_i = 3$, and $n_e = 8$.

As shown, both the KL model and the model with extensions give virtually the same response for this specimen. The use of brace extensions however permits to reproduce adequately the out-of-plane deformations (Fig. 10c). It must also be noted that the energy dissipation in the gusset plates can be included in this model by specifying the plastic moment resistance of the gusset plates for the extension members. In the analysis of actual braced frame structures, however, the modeling of the extensions and the support conditions at the outer ends of the brace extensions can still represent a challenge for the analyst and a more convenient model should be developed for that purpose.

Brace model with rotational springs

In the third option, the flexural restraint at brace ends is incorporated by means of zero-length rotational springs. The simplest models would include linear elastic springs with a stiffness C_g. More sophisticated representation can however be considered to reproduce the hysteretic response of the gusset plates under the successive bending cycles imposed at every brace load reversal. Such a refined modeling is adopted herein in which the rotational springs were given the flexural stiffness and strength of the gusset plates (C_g and M_{pg} in Table 5). In addition, the GMP steel model that was used for the braces was also applied for the gussets.

In this model, the brace length corresponds to the actual brace length and flexural strength is assigned to the gusset plates. In frame analysis, torsional restraint of the brace and gusset plates can also be included when out-of-plane buckling is studied. Brace torsional properties must then be added to the fiber nonlinear beam-column element using the aggregation tool in OpenSees. One limitation of the model is that the flexural strength of the rotational spring does not vary as a

function of the axial load applied by the brace to the gusset plate. Therefore, the spring resistance in the gusset model can be overestimated when high axial loads are transmitted by the gusset, as is the case when tension yielding develops in the braces. Figure 11a shows the predicted M-θ hysteretic response of the upper gusset plate of Specimen S2A. The predicted and measured brace end rotations are also compared for this specimen. Again, n_f = 16, n_i = 3, and n_e = 8 were used in these calculations. Due to its limitations, the model tends to overestimate the end rotations at large brace deformations, as a result of the permanent rotation that gradually develops upon load reversals due to the too high flexural resistance. However, the very good match between test and predicted axial and out-of-plane brace responses in Figs. 11c and 11d suggest that this error has limited impact on brace overall behavior.

Figure 12 compares the predicted hysteretic and out-of-plane responses of the three remaining brace specimens. Again, excellent match is obtained in all cases except for the axial load prediction during the large positive deformation excursion tension for Specimen SQ1B. This difference can be attributed to the methodology used to measure F_y in the tests (2% offset method), as this approach does not capture well progressive yielding including residual stress effects observed in HSS members. The figure also shows that the model can overestimate the peak compression brace resistance at first buckling, likely because residual stresses are not included in the model. Again, degradation of brace tension capacity due to local buckling and material fracture is not captured by the model. Table 6 compares the test and predicted total energy dissipated by the brace up to the point of zero deformation in the last tension half-cycle before fracture. As shown, the models generally underestimate the energy dissipated by the braces, especially for Specimen S1QB due to the error in predicting the measured yield tensile resistance. The results however show that little error is induced when using 8 elements to discretize the braces.

INELASTIC FRAME ANALYSIS

Comparison with test results

The overall response of the test X-braced frame by Tremblay et al. (2003) with Specimen X6-C is compared to that of the model analysis. The frame is shown in Fig. 13a. In the test, true pinned connections were built at the column bases and at the beam-to-column joints such that the applied lateral load was entirely resisted by the braces. The braces were HSS 64x64x4.8 with the following properties: A = 1060 mm^2, r = 23.6 mm, F_y = 397 MPa, E = 189 GPa, KL/r = 89.8, λ = 1.31, and J = 995x10^3 mm^4. At brace intersection, one brace was continuous whereas the other brace was interrupted. However, as shown in the figure, full torsional and flexural continuity was restored between the two brace segments by means of welding and connecting plates. The braces were connected at their ends with gusset plates 300 mm wide by 9.5 mm thick. At the lower brace ends, the gusset plates were connected to the frame columns. At the top ends, the gussets were welded to the beam only. Beam and column properties are given in Fig. 13b. For this frame, the yield storey shear, V_y, is defined as the sum of the horizontal components of the brace tension yield capacity: V_y = 674 kN. The yield story drift, Δ_y, is equal to 12.1 mm.

A general purpose model was developed with rotational springs at beam-to-column joints (C_1), and with springs exhibiting rotational and torsional properties at brace ends (C_2 *and* C_3) and at the connection between the two braces (C_4). For this particular test application, C_1 = 0, C_2 = 29 kN-m/rad (flexure) and 45 kN-m/rad (torsion), and C_3 = 37 kN-m/rad (flexure) and 45 kN-m/rad (torsion). The flexural capacity of springs C_2 and C_3 was set equal to 2.045 kN-m. Springs C_4 was given infinite stiffness and strength in flexure and torsion. As mentioned earlier, the torsional properties of the braces had to be added to the fiber beam-column brace elements to capture their

torsional reponse. The frame was subjected to a symmetrical displacement protocol with stepwise incremental amplitudes. The braces were modeled using the GMP steel material with the properties as defined in the previous section. The parameters n_f = 16 and n_i = 4 were used, and the number of elements in each of the half-brace segment was varied as followed: n_e = 2, 4, 8, and 16. The shape of the initial brace out-of-straightness was set to match the observed buckling mode.

Figures 14a to 14c compare the measured and predicted lateral load-lateral deformation response of the frame as well as the out-of-plane deformation response at mid-length of the lower half-brace segment of the continuous brace and at the brace intersection point. The results shown were obtained using 4 elements for each of the half-brace segments. Excellent agreement is found between the experimental and computed results. Figs. 14d and 14e show the influence of the number of elements on the global hysteretic response and the energy dissipated by the frame, E_H. The cumulated energy dissipation in the test was equal to 26.1 $V_y\Delta_y$. The analysis results are 23.8, 22.7, 22.2, and 22.2 $V_y\Delta_y$ with n_e = 2, 4, 8, and 16, respectively. These results again show that a total of 8 elements per brace would be adequate to properly reproduce the behavior of braces of this type.

Seismic analysis

The response of an actual single-storey X-braced steel frame subjected to an earthquake ground motion is examined to assess the validity of the model for inelastic seismic response analysis. The building plan dimensions are 45 m x 45 m and its height is 3.658 m. The structure is located in Victoria, B.C., Canada, on a stiff soil site. The design was performed according to the provisions of the 2005 National Building Code of Canada (NRCC, 2005) and the CSA-S16-01 Standard for the design of steel structures in Canada (CSA, 2001). Steel with nominal F_y = 345 MPa, E = 200 GPa, and G = 77 GPa is used for all members. For simplicity, the roof diaphragm is assumed infinitely stiff and the total seismic weight (5508 kN) is concentrated at the roof level. A single braced bay, 9.0 m wide, is used on each of the exterior walls and tension-only design was assumed. The bracing members are HSS 102x102x6.4 with the following properties: A = 2170 mm^2, r = 38.6 mm, KL/r = 113, λ = 1.50, J = 5320x10^3 mm^4. The braced bay columns are HSS 152x152x4.8 (A = 2570 mm^2, I = 9.27x10^6 mm^4) and the beams are W460x60 (A = 7590 mm^2, I = 255x10^{6}mm^4). The base of the columns is assumed to be pinned and simple shear connections are used between the beams and the columns. The fundamental period of the structure is 0.55 s if the compression braces are neglected. It reduces to 0.38 s when the contribution of the compression braces is included.

The model in Fig. 13b can be employed for this structure. An expected yield strength F_{ye} = 385 MPa was used for the braces and gusset plates. Spring C_1 was given zero stiffness. Springs C_2 and C_3 both have a flexural stiffness of 173 kN-m/rad and a flexural strength of 5.42 kN-m for out-of-plane bending. They were considered as infinitely stiff for in-plane bending and their torsional stiffness was set equal to 216 kN-m/rad for spring C_2 and 227 kN-m/rad for spring C_3. Spring C_4 was defined as fully rigid in all three rotational axes, assuming the same type of connection as in test frame X6-C. The rigid extensions at the lower and upper brace ends are respectively 353 mm and 843 mm long.

The analysis is carried out under a record from the 1994 **M**7.0 Northridge earthquake (Station Standford University, Component 0°). The record was scaled by 1.43 to match the design spectrum and to account for accidental building eccentricity effects. The brace model was used with n_f = 16, n_i = 4, and different values for n_e: 4, 8, and 16. The tolerance was set to 10^{-3} and the Newton-Raphson with line search algorithm was adopted to improve the convergence. Time step values, Δt, of 0.01 s and 0.001 s were used. In analyses performed with time steps longer than 0.01 s, convergence could not be reached upon first brace buckling. Mass proportional Rayleigh

damping was used with 5% in the first structure mode (T_1 = 0.38 s).

Figures 15a compares the time history of the roof horizontal displacement for the two time steps and n_e = 4 and 16. The time history of the energy dissipated in the system for Δt = 0.01 s is also given in the figure. Figure 15b shows the hysteretic response obtained for n_e = 4 when using Δt = 0.01 and 0.001 s, showing the effect of brace response degradation on the lateral strength and stiffness of the frame under cyclic loading. For Δt = 0.01s, the total energy dissipated by the braces with n_e = 4, 8, and 16 is respectively equal to 6.27, 6.28 and 6.29 $V_y\Delta_y$. For Δt = 0.001 s and n_e = 4, E_H = 6.36 $V_y\Delta_y$. These results clearly indicate that good predictions can be achieved for typical braced frames similar to the one studied herein by using a time step of 0.01 s and 4 elements per half-brace segment.

CONCLUSIONS

Parametric studies were carried out to evaluate the influence of modeling assumptions when simulating the hysteretic response of steel bracing members with the OpenSees finite element computer program. Nonlinear beam-column elements were used with a fiber representation of member cross-sections. The study showed that the number of integration points per element has limited influence on the response and that accurate results could be obtained with three integration points. For a given set of parameters, the force based formulation was found to provide higher accuracy compared to the displacement based formulation. This formulation should therefore be preferred, even if it requires longer computational time. As expected, the errors were found to reduce when increasing the number of elements or the number of fibers. The results indicate that sufficient accuracy could be achieved for typical bracing members if 8 elements per brace member were used together with 16 fibers for cross-section discretization. The use of the Giuffré-Menegotto-Pinto constitutive model was also found to provide a more realistic representation of the brace hysteretic response compared to the simpler bi-linear model. Comparisons between test and predicted results as well as simple dynamic seismic analysis confirm the appropriateness of these modeling assumptions for typical low-storey braced frame applications.

The brace model was found to give realistic predictions of the hysteretic response of braces having different sizes, slenderness ratios or end restraint conditions. This is by far superior to using empirical or semi-empirical models which specific test data are needed to adequately reproduce key response properties. However, the brace modeling considered in this study still has some limitations. For instance, it does not account for residual stress effects on compression strength at first buckling, and local buckling effects and brace fracture cannot be reproduced by the model. It is recommended that future work be devoted to implement local buckling effects as well as brace fracture by means of a damage model, such as the one proposed by Jin and El-Tawil (2003).

ACKNOWLEDGEMENTS

This research was supported by the Natural Sciences and Engineering Research Council of Canada. The authors also wish to acknowledge J. Brad Shaback and Madhar Haddad for providing test data as well as Charles-Philippe Lamarche for his valuable contribution in the analysis of the frame structures.

REFERENCES

[1] AISC. 2005. *ANSI/AISC 341-05, Seismic Provisions for Structural Steel Buildings*. American Institute of Steel Construction. Chicago, Il.

[2] Astaneh-Asl, A., Goel, S.C. and Hanson, R.D. 1985. Cyclic Out-of-Plane Buckling of Double-Angle Bracing. *J. of Struct. Eng., ASCE,* 111, 1135-1153.

[3] ASTM. 2003. *ASTM A500-3, Standard Specification for Cold-Formed Welded and Seamless Carbon Steel Structural Tubing in Rounds and Shapes,* ASTM International, West Conshohocken, PA.

[4] Barbato, M. and Conte, J.P. 2004. Finite Element Response Sensitivity Analysis: a Comparison Between Force-Based and Displacement-Based Frame Element Models. *Computer Methods in Applied Mechanics and Engineering*, 194, 1479-1512.

[5] Chajes, A. 1974. *Principles of Structural Stability Theory*. Prentice-Hall, Inc., Englewood Cliffs, NJ.

[6] CSA. 2001. *CSA-S16-01, Limit States Design of Steel Structures*. Canadian Standards Association, Toronto. ON.

[7] ECCS. 1986. *ECCS – TWG 1.3 Seismic Design Recommended Testing Procedure for Assessing the Behaviour of Structural Steel Elements under Cyclic Loads.* European Convention for Constructional Steelwork, Technical Committee - Structural safety and loading, Brussels, Belgium.

[8] Jin, J. and El-Tawil, S. 2003. Inelastic Cyclic Model for Steel Braces. *J. of Eng. Mech., ASCE*, 129, 5, 548-557.

[9] Haddad. M. 2004. Ph.D. Thesis. Dept. of Civil Eng., Univ. of Calgary, Calgary, AL.

[10] McKenna, F. and Fenves, G.L. 2004. *Open System for Earthquake Engineering Simulation (OpenSees)*. Pacific Earthquake Engineering Research Center (PEER), University of California, Berkeley, CA. (http://opensees.berkeley.edu/index.html)

[11] NRCC. 2005. *National Building Code of Canada, 12th ed.*, National Research Council of Canada, Ottawa, ON.

[12] Shaback, J.B. and Brown, T. 2003. Behaviour of square hollow structural steel braces with end connections under reversed cyclic axial loading. Can. J. Civ. Eng., 30, 745–753.

[13] Tremblay, R., Poncet, L., Bolduc, P., Neville, R., and DeVall, R. 2004. Testing and Design of Buckling Restrained Braces for Canadian Application. *Proc. 13th World Conference on Earthquake Eng.*, Vancouver, BC, Paper no. 2893.

[14] Tremblay, R., Archambault, M.-A., and Filiatrault. A. 2003. Seismic Performance of Concentrically Braced Steel Frames made with Rectangular Hollow Bracing Members. *J. of Struct. Eng., ASCE,* **129:12**, 1626-1636.

[15] Tremblay, R. and Bouatay, N. 2002. Loading Protocols for the Seismic Testing of Ductile Bracing Members in Concentrically Braced Steel Frames. *Proc. 12th European Conf. on Earthquake Eng.*, London, UK, Paper No. 480.

[16] Uriz, P. and Mahin, S. A. 2004. Seismic performance Assessment of Concentrically braced steel Frames. *Proc. 13th World Conference on Earthquake Eng.*, Vancouver, BC, Paper No. 1639.

TABLE 1 Mean quadratic error values (% P_y)

n_e	Displacement based elements			Force based elements		
	$n_i = 4$	$n_i = 5$	$n_i = 6$	$n_i = 4$	$n_i = 5$	$n_i = 6$
4	20.1	20.1	20.0	12.5	12.5	12.4
8	4.80	4.95	4.86	2.22	2.12	2.10
16	1.32	1.29	1.27	0.68	0.74	0.65
24	0.61	0.61	0.61	0.19	0.15	0.14
32	0.02	0.04	0.00	0.05	0.05	0.00

TABLE 2 Brace properties

Shape	A (mm^2)	$I_x = I_y$ (10^6 mm^4)	r (mm)	KL (mm)	KL/r ( )	λ ( )
305x305x16	16100	222	118	4460	37.8	0.5
203x203x9.5	6490	40.3	78.9	5964	75.6	1.0
102x102x6.4	2110	3.16	38.7	5855	151.3	2.0

TABLE 3 Total E_H ($/P_y\delta_y$)

Brace λ	Model	Loading protocol		
		AISC	ECCS	WC
0.5	Simple	52.77	57.19	54.03
	Refined	52.38	56.78	53.67
2.0	Simple	12.50	13.30	9.07
	Refined	12.43	13.23	9.04

TABLE 4 Test brace properties

No.	Shape	A (mm^2)	I ($10^6 mm^4$)	r (mm)	L (mm)	E (GPa)	F_y (MPa)	δ_y (mm)	v_o (mm)
S2A	102x76x4.8	1550	2.18	37.5	4614	185	381	7.79	4.6
S1QB	127x76x4.8	1790	3.78	45.9	4614	198	395	7.93	4.6
1B	127x127x8	3620	8.36	48.0	3401	191	421	8.30	3.0
2	152x152x8	4430	15.1	58.4	4900	190	467	10.5	3.0

TABLE 5 Test brace connection and slenderness properties

No.	C_g (kN-m/rad)	K ( )	KL (mm)	KL/r	λ	L_c (mm)	M_{pg} (kN-m)
S2A	63 (75)[(1)]	0.88	4051	108	1.56	19200 (16132)	3.68
S1QB	62 (75) [(1)]	0.93	4277	93.2	1.32	36210 (29940)	3.68
1B	1150	0.75	2545	52.6	0.79	4165	10.9
2	1290	0.76	3727	63.4	1.01	6672	12.1

[(1)]Value for the upper brace end, value in brackets for the lower brace end.

TABLE 6 Total E_H ($/P_y\delta_y$)

Case	Brace Specimen			
	S2A	S1QB	1B	2
Test	40.1	18.2	27.4	12.0
$n_e = 8$	40.5	14.5	23.4	8.57
$n_e = 16$	40.3	14.4	23.3	8.46
$n_e = 32$	40.2	14.4	23.3	8.45

Figure Captions

Fig. 1: Typical hysteretic response of steel bracing members (adapted from Tremblay et al., 2003).

Fig. 2: a) Fiber discretization; b) Typical hysteretic responses from computation.

Fig. 3: Influence of the element formulation, n_e and n_i on: a) Computational time; b) Mean quadratic error, *MQE*.

Fig. 4: Steel material models: a) Bi-linear model; b) Giuffré-Menegotto-Pinto model.

Fig. 5: Comparison of the predicted response obtained from the Giuffré-Menegotto-Pinto and bi-linear steel models for: a) $\lambda = 0.5$; b) $\lambda = 1.0$ ($n_e = 8$ and $n_f = 16$, $n_i = 3$).

Fig. 6: Influence of n_e and n_f on brace response parameters for: a) $\lambda = 2.0$; b) $\lambda = 1.0$; and c) $\lambda = 0.5$.

Fig. 7: Influence of test displacement protocol on brace energy dissipation: a) AISC displacement protocol; b) ECCS displacement protocol; and c) WC displacement protocol.

Fig. 8: Brace end connections: a) Typical brace connection; b) Plastic hinge in gusset plate upon brace buckling; c) Brace and gusset plate responses upon brace buckling; d) Brace model with length = *KL*; e) Brace model with extended brace segments; f) Brace model with zero-length end rotational springs.

Fig. 9: Comparison between test and pin-ended model with length *KL*: a) Hysteretic response with $R_0 = 25$, $a_1 = a_3 = 0.00001$, and $a_2 = a_4 = 0.00002$; b) Hysteretic response with $R_0 = 20$ and a_1 to $a_4 = 0.0$; c) Out-of-plane response at brace mid-length with $R_0 = 20$ and a1 to a4 = 0.0.

Fig. 10: Response of Specimen S2A using the brace model with end extensions: a) Comparison between test and predicted hysteretic responses; b) Comparison of the hysteretic responses predicted by the KL and the extension brace models; c) Comparison between test and predicted out-of-plane responses at brace mid-length.

Fig. 11: Validation of the response of Specimen S2A from the model with rotational end springs (n_f = 6, n_i = 3, n_e = 8): a) Upper gusset plate moment-rotation hysteresis;b) Comparison of test and predicted upper gusset plate rotation; c) Comparison of test and predicted brace hysteretic axial response; and d) Comparison of test and predicted brace out-of-plane response.

Fig. 12: Comparison between test and predicted brace hysteretic axial and out-of-plane responses for: a) Specimen S1QB; b) Specimen 1B; and c) Specimen 2.

Fig. 13: Full scale frame test: a) Test Setup for Specimen X6-C (adapted from Tremblay et al., 2003); b) Frame model.

Fig. 14: Response of test frame X6-C: a) Comparison between test and predicted (n_e = 4) lateral load-lateral deformation hysteretic responses; b) Out-of-plane deformation response at the lower half-brace segment; c) Out-of-plane deformation response at the brace intersection point; d) Influence of n_e on the lateral load-lateral deformation response prediction; and e) Influence of n_e on the energy dissipation prediction.

Fig. 15: Seismic response of a single-storey X-braced steel frame building: a) Time history of roof displacement and dissipated energy; b) Influence of time step on base shear-roof displacement hysteretic response.

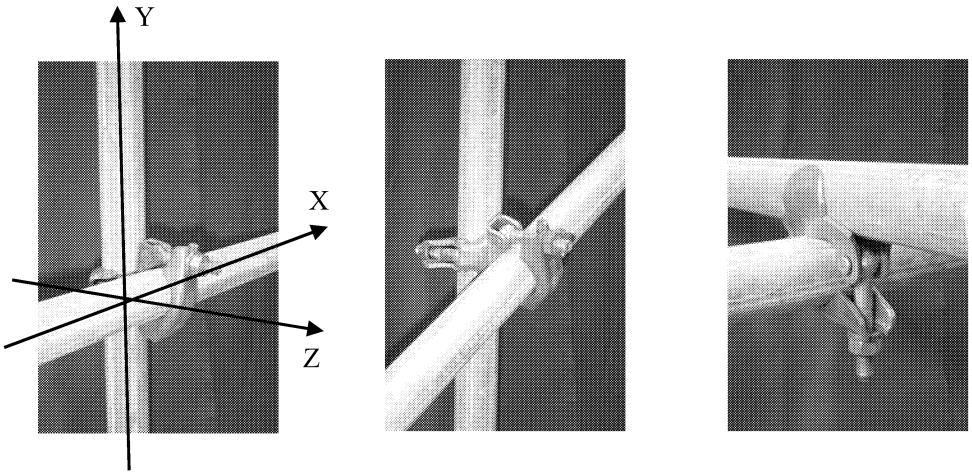

(a) right-angle coupler (b) Swivel coupler (c) Putlog coupler

Figure 1. Three types of scaffolding coupler

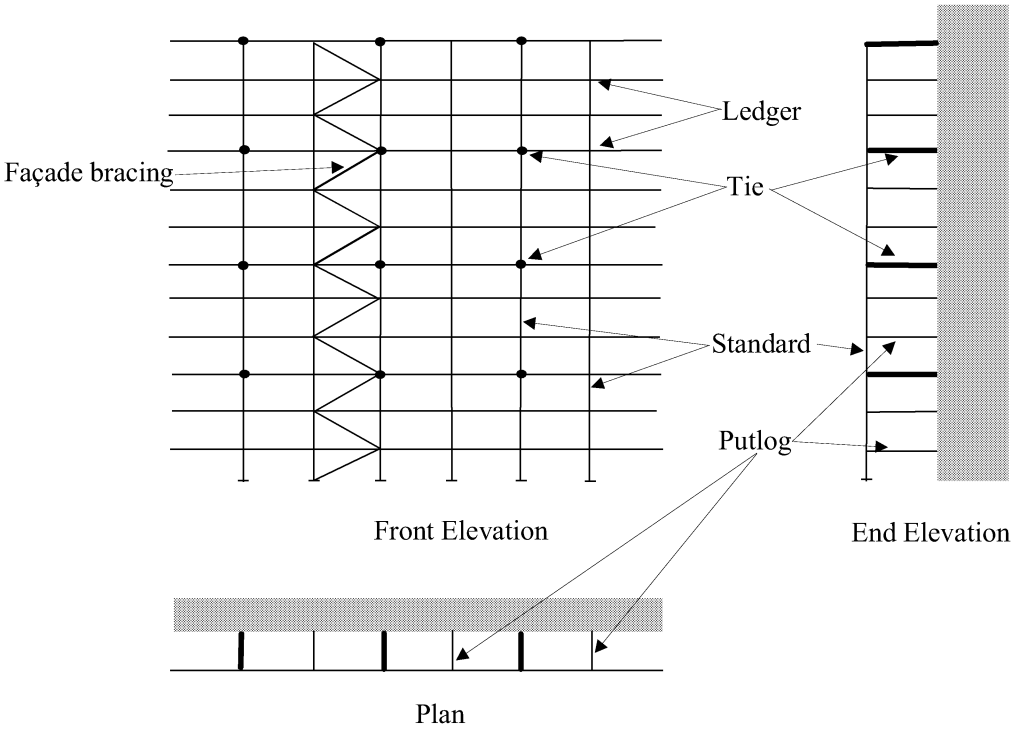

Figure 2. Typical Putlog Scaffold

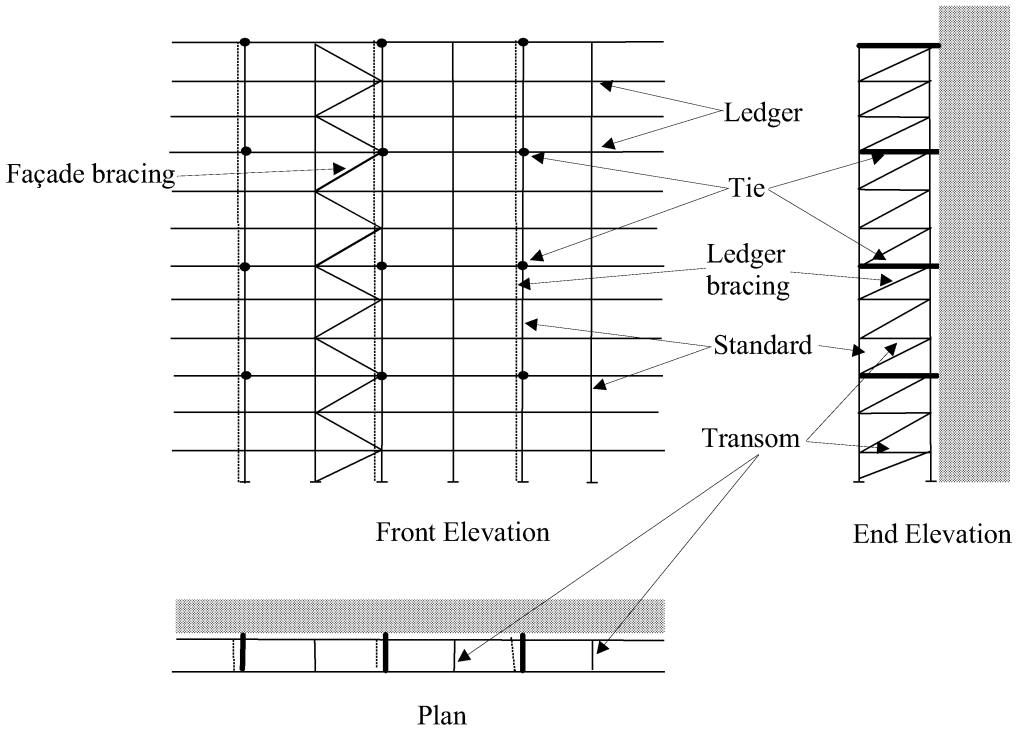

Figure 3. Typical Independent Tied Scaffold

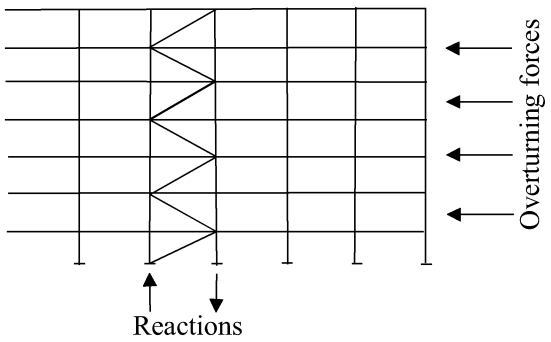

Figure 4. Bracing action under side loads

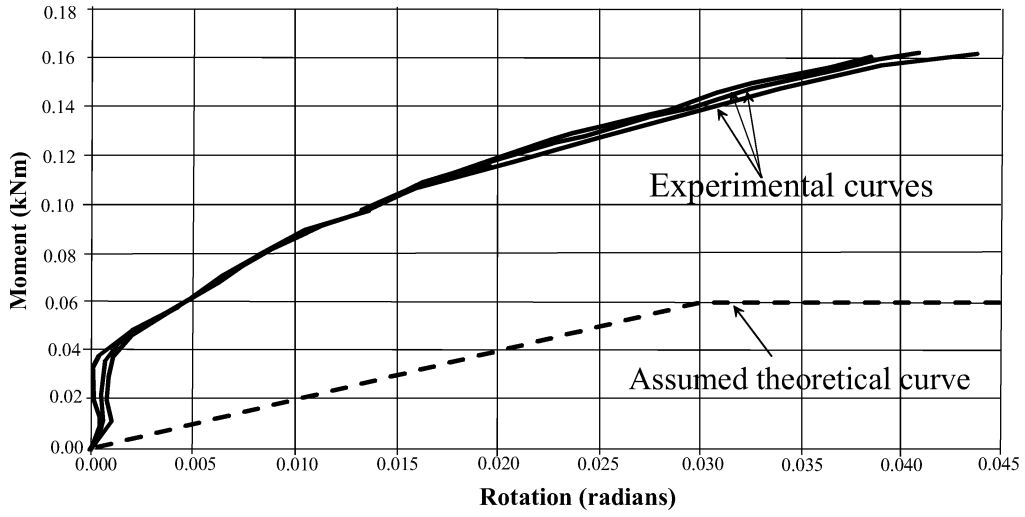

Figure 5. Moment-Rotation Characteristics for a Putlog Coupler

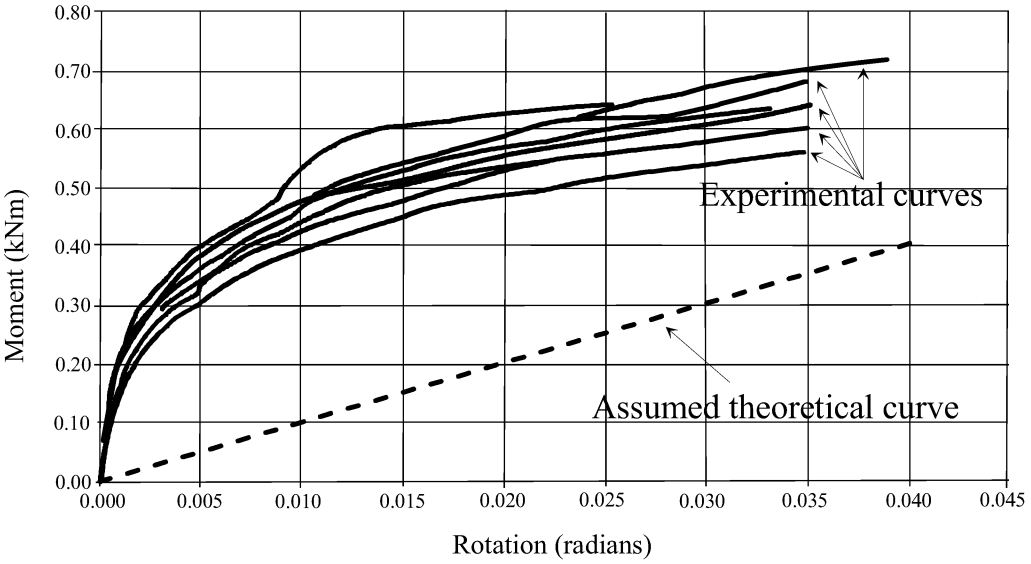

Figure 6. Moment–Rotation Characteristics for a Right Angle Coupler

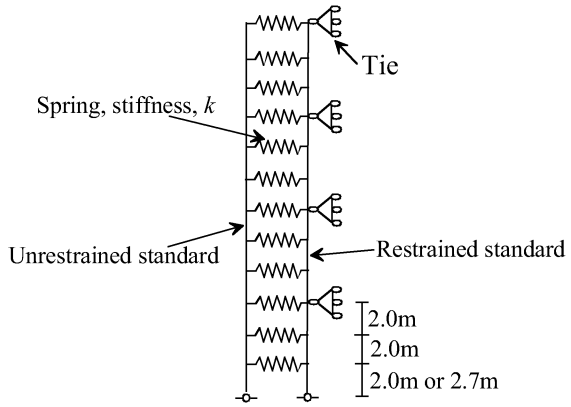

Figure 7. Two column Putlog model for buckling normal to the facade

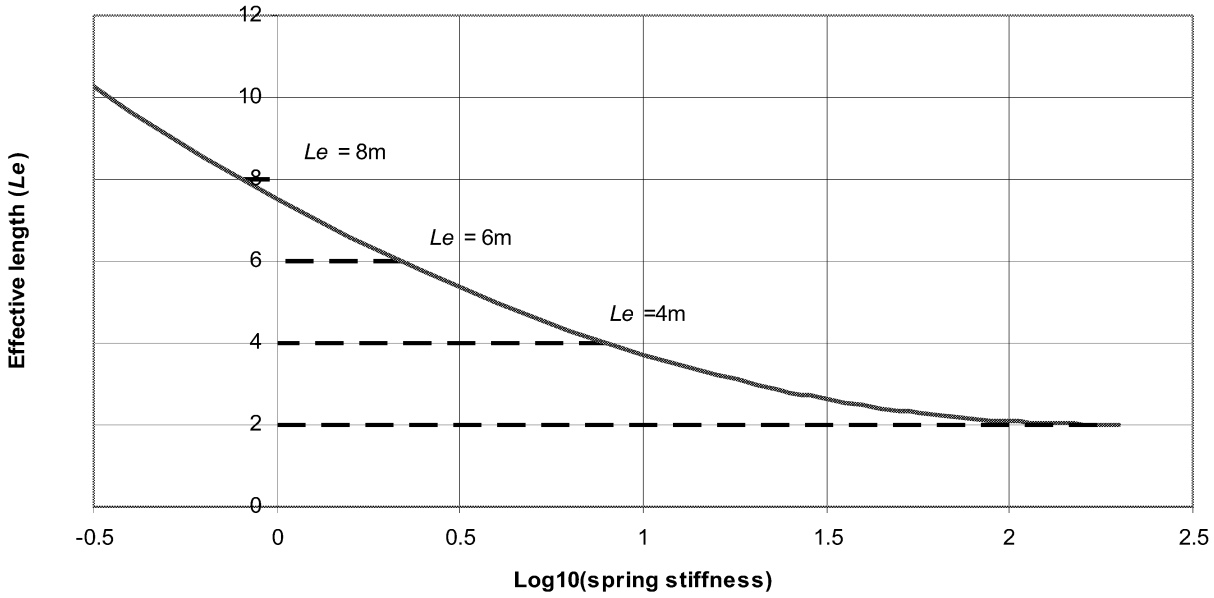

Figure 8. Variation of effective length with spring stiffness

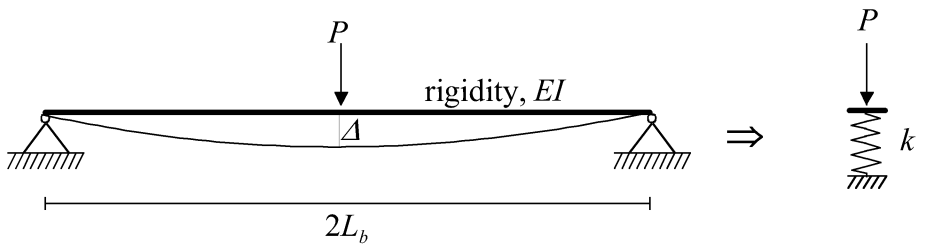

Figure 9. Derivation of stiffness for 'pinned' ledgers

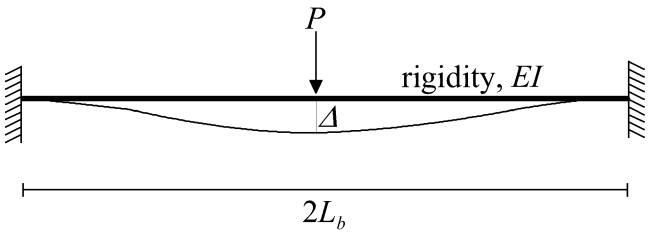

Figure 10. Derivation of stiffness for 'fixed' ledgers

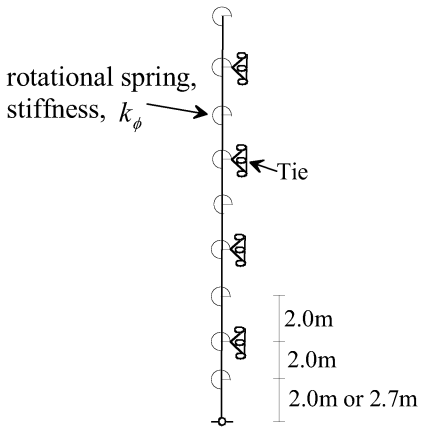

Figure 11. Single column model for the rear face of a tied scaffold

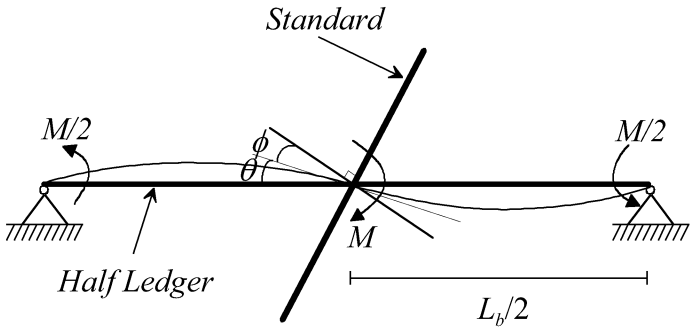

Figure 12. Derivation of rotation stiffness for standard-ledger connection in double curvature

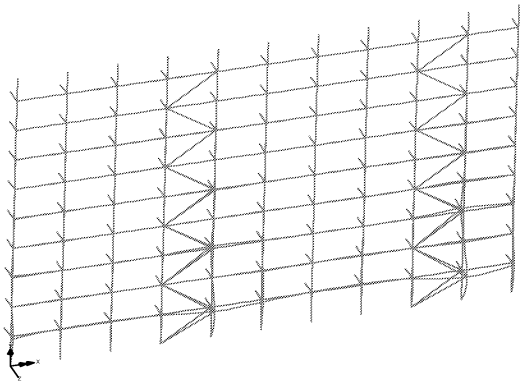

(a) Buckling of leeward braced standard normal to the facade for a Putlog scaffold

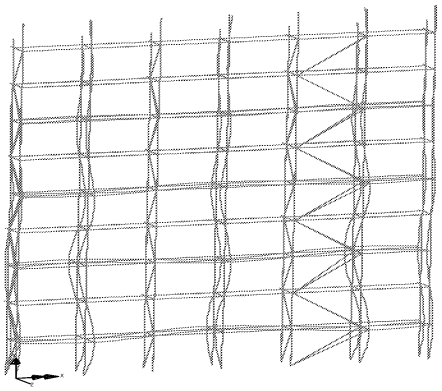

(b) Buckling of independent tied scaffold normal to the façade

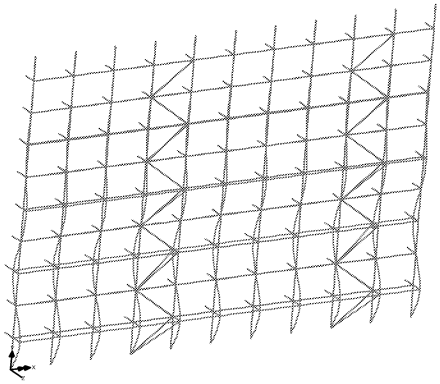

(c) Uniform buckling of Putlog scaffold normal to the facade

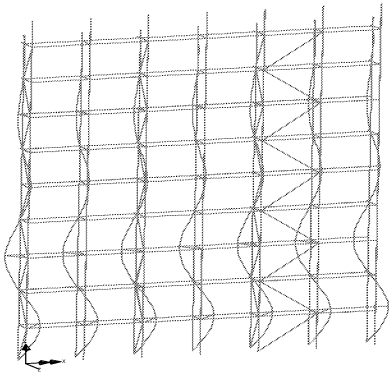

(d) Buckling of tied scaffold parallel to the facade (only the rear face buckles)

Figure 13. Examples of buckling modes

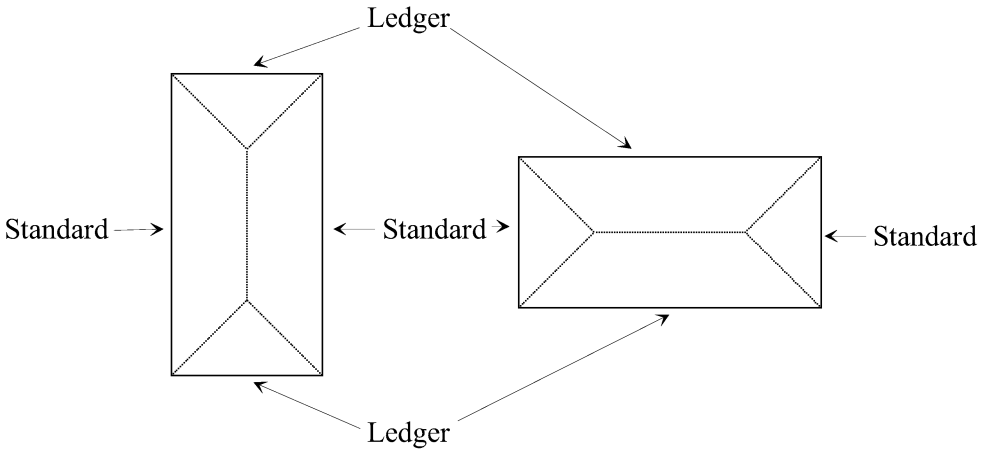

Figure 14. Wind load distribution patterns

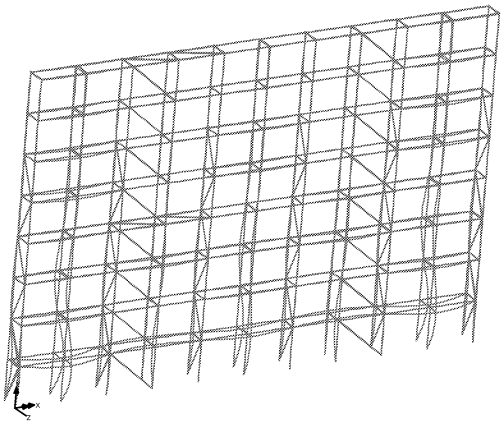

(a) tied scaffold buckling normal to facade

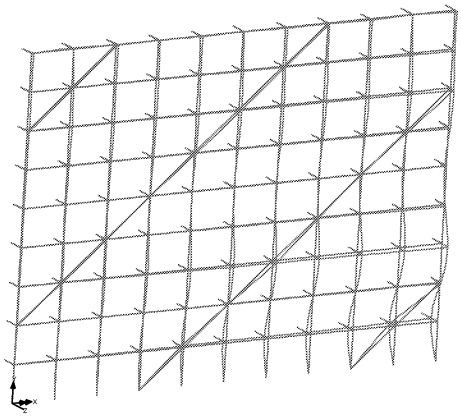

(b) Putlog scaffold buckling normal to facade

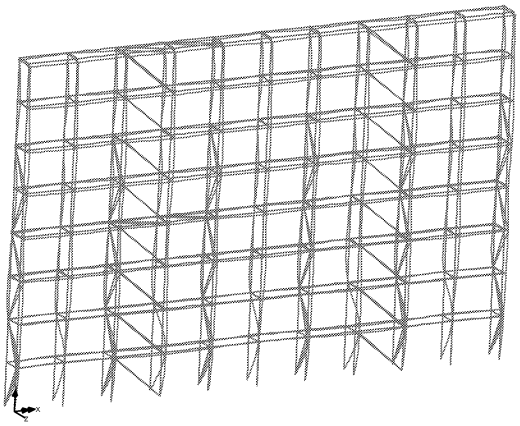

(c) tied scaffold with rear face buckling parallel to facade

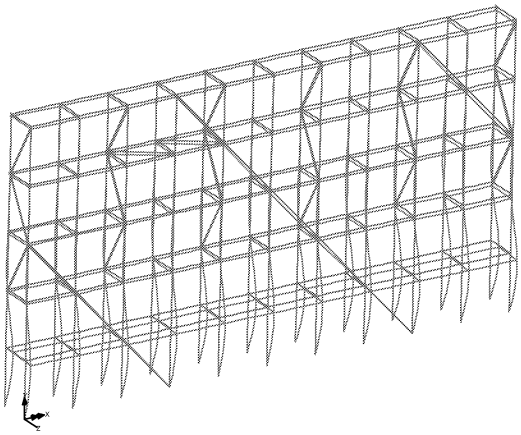

(d) tied scaffold buckling normal to facade with no ledger bracing in bottom two lifts

Figure 15. Examples of ultimate failure modes

Table 1. Effective lengths for Putlog scaffolds found from the two-dimensional model

	Tie Interval	Span = 2.7m	Span = 2.1m	Span = 1.8m
Simply Supported Ledgers	2m	3.94	3.17	2.77
	4m	4.06	4.00	4.00
	6m	6.00	6.00	6.00
	8m	8.00	8.00	8.00
Fixed Ended Ledgers	2m	2.64	2.18	2.02
	4m	4.00	4.00	4.00
	6m	6.00	6.00	6.00
	8m	8.00	8.00	8.00

Table 2. Tie Patterns

Case	Tie position above base (m)								
1	2.7	4.7	6.7	8.7	10.7	12.7	14.7	16.7	18.7
2	2.7		6.7		10.7		14.7		18.7
3	2.7			8.7			14.7		18.7
4	2.7				10.7				18.7
5	2.0	4.0	6.0	8.0	10.0	12.0	14.0	16.0	18.0
6		4.0		8.0		12.0		16.0	18.0
7			6.0			12.0			18.0
8				8.0				16.0	18.0
9	2.0		6.0		10.0		14.0		18.0
10	2.0			8.0			14.0		18.0
11	2.0				10.0				18.0

Table 3. Effective lengths of Putlog scaffolds for different bay widths
buckling normal to the façade determined by the three-dimensional analysis

Case	1.8m	2.1m	2.7m
1	2.83	3.17	3.94
2	3.91	3.92	3.99
3	5.03	5.04	5.06
4	7.24	7.24	7.26
5	2.77	3.16	3.94
6	3.90	3.91	4.03
7	6.00	6.00	6.00
8	7.20	7.21	7.25
9	3.90	3.91	3.99
10	4.99	4.99	5.02
11	7.39	7.20	7.35

Table 4. Effective lengths of independent tied scaffold with full ledger bracing

	Parallel to façade			Normal to facade		
Case	1.8m	2.1m	2.7m	1.8m	2.1m	2.7m
1	2.39	2.29	2.29	2.83	3.17	3.94
2	3.42	3.42	3.43	2.85	3.19	3.95
3	4.16	4.16	4.18	2.87	3.21	3.95
4	5.03	5.04	5.01	2.90	3.27	4.01
5	1.90	1.90	1.90	2.77	3.16	3.94
6	3.56	3.56	3.56	2.78	3.18	3.95
7	4.81	4.81	4.83	2.90	3.25	3.98
8	5.55	5.57	5.57	3.29	3.18	3.96
9	3.40	3.41	3.41	2.84	3.19	3.95
10	4.12	4.13	4.13	2.86	3.21	3.95
11	5.00	5.02	5.04	2.90	3.26	4.01

Table 5. Effective lengths of independent tied scaffold with partial ledger bracing

		Parallel			Normal		
Description	Case	1.8m	2.1m	2.7m	1.8m	2.1m	2.7m
No bottom brace	2	3.46	3.47	3.47	3.21	3.37	3.57
	9	3.45	3.45	3.45	3.20	3.36	3.56
No brace in bottom two	2	3.46	3.47	3.47	3.21	3.38	3.57
levels	9	3.45	3.45	3.45	3.20	3.36	3.56
No brace in second and third	2	3.42	3.42	3.42	3.26	3.40	3.58
levels from bottom	9	3.40	3.41	3.41	3.22	3.37	3.56
No ledger brace	2	3.41	3.42	3.43	3.70	3.74	3.81
	6	3.56	3.56	3.56	3.75	3.77	3.81
	9	3.40	3.40	3.41	3.69	3.73	3.81

Table 6. Weights of scaffold components

Component	Weight
Coupler	1.8 kg
Ledger, standard, putlog, guard-rail	4.37 kg/m
Toe board	5.36 kg/m

Table 7. Table of loads

Class	Load intensity (kN/m²)	Reduction factor	No. of Boards	Bay width (m)
1	0.75	0.00	3	2.7
2	1.50	0.25	4	2.4
3	2.00	0.25	5	2.1
4	3.00	0.50	5	1.8

Table 8. Scaffolds Analysed

Scaffold type	Ref. No.	Class	Sheeted or not	Boarded or not	Ledger bracing	Wind Storm param. **S**	T or C	Dist. to Sea	No of levels	Facade bracing
Putlog	1	1	not	yes	N/A	20	T	100	6	2 bays in 5
Putlog	2	2	not	not	N/A	24	C	0.1	9	5 bays in 5
Independent	3	2	not	yes	part	20	T	10	8	1 bay in 5
Independent	4	3	debris	not	full	24	C	10	17	2 bays in 5
Independent	5	4	sheeted	yes	part	28	T	0.1	5	5 bays in 5
Putlog	6	1	not	not	N/A	28	T	10	6	2 bays in 5
Independent	7	3 cant	not	yes	part	40	T	0.1	8	1 bay in 5
Independent	8	4 cant	not	not	full	40	C	100	17	5 bays in 5
Independent	9	1	debris	yes	full	32	T	0.1	8	2 bays in 5
Independent	10	4	sheeted	not	part	32	T	100	5	5 bays in 5

Table 9. Results of analyses

Ref. No.	Load case giving maximum limit state	Max k at T_λ =1	Max T_λ	Mode
1	Service wind, normal to facade	0.696	6.360	Buckling normal to facade
2	Service wind, normal to facade	0.375	2.130	Buckling normal to facade
3	Service wind, normal to facade	0.730	1.845	Buckling normal to facade
4	Service wind, parallel to façade	0.458	1.947	Buckling parallel to facade
5	Out-of-service wind, parallel to facade	1.006	2.641	Buckling normal to facade
6	Out-of-service wind, normal to façade	0.549	3.000	Not buckled, maximum increments exceeded
7	Out-of-service wind, parallel to facade	0.984	1.575	Not buckled, convergence failure
8	Out-of-service wind, parallel to façade	1.072	2.407	Not buckled, excessive bending in ledger
9	Out-of-service wind, parallel to facade	0.975	3.000	Not buckled, maximum increments exceeded
10	Out-of-service wind, parallel to facade	0.730	3.000	Not buckled, maximum increments exceeded

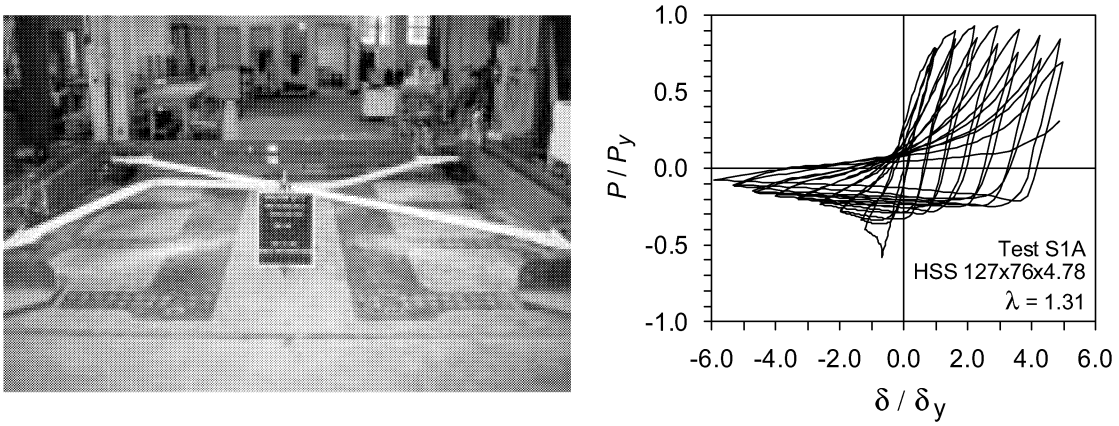

Fig. 1 Agüero et al.

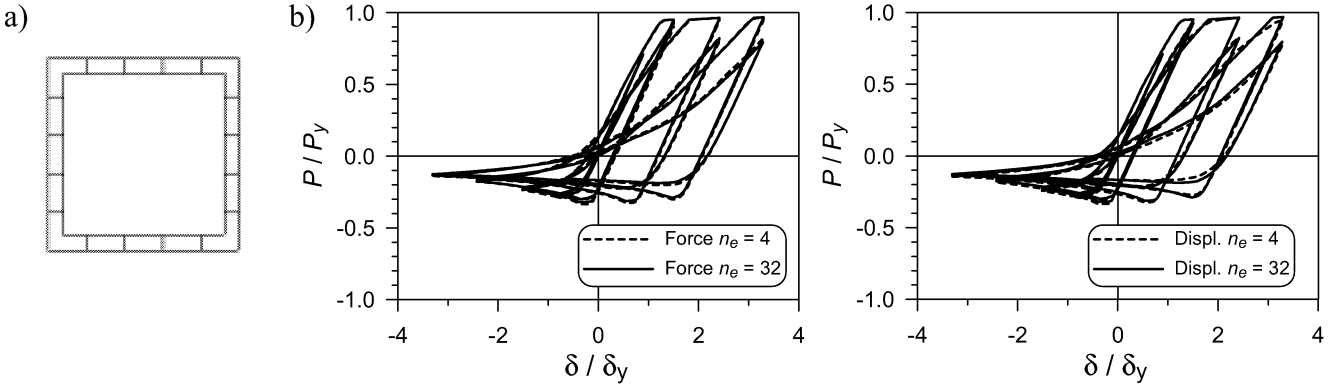

Fig. 2 Agüero et al.

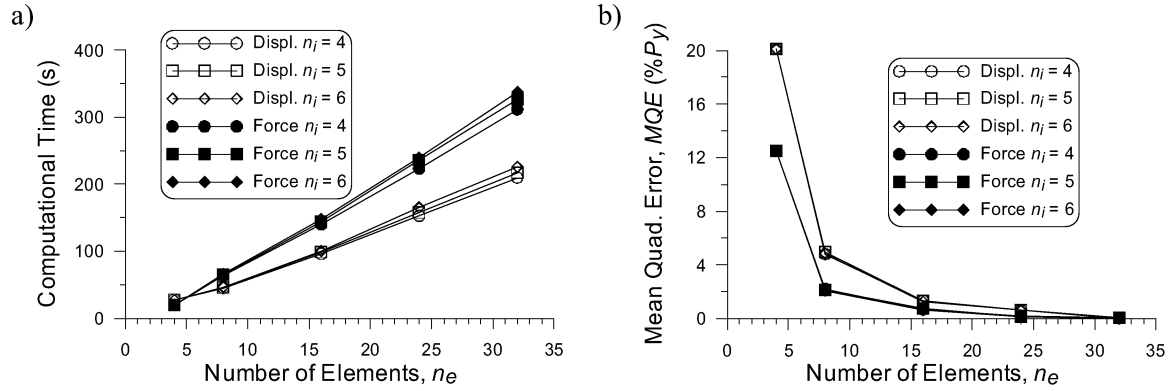

Fig. 3 Agüero et al.

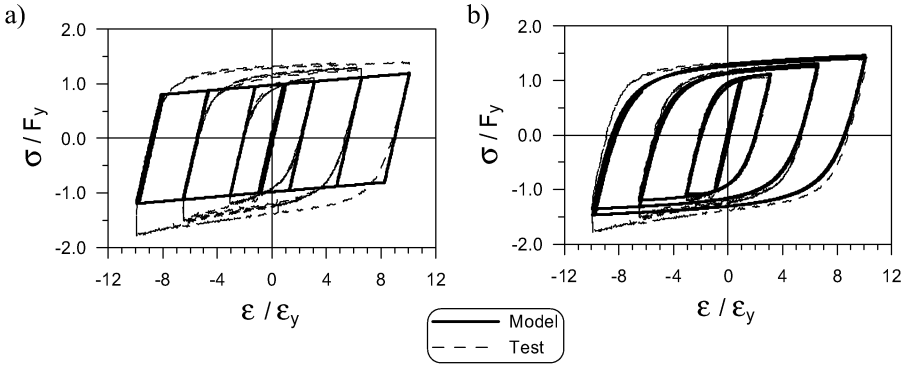

Fig. 4 Agüero et al.

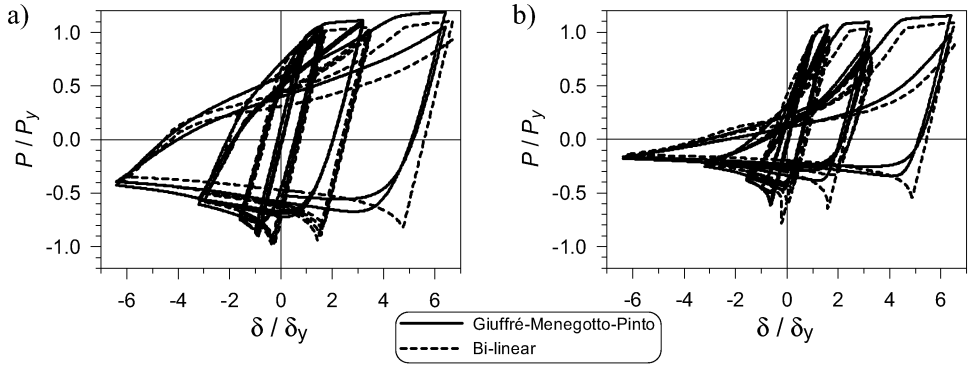

Fig. 5 Agüero et al.

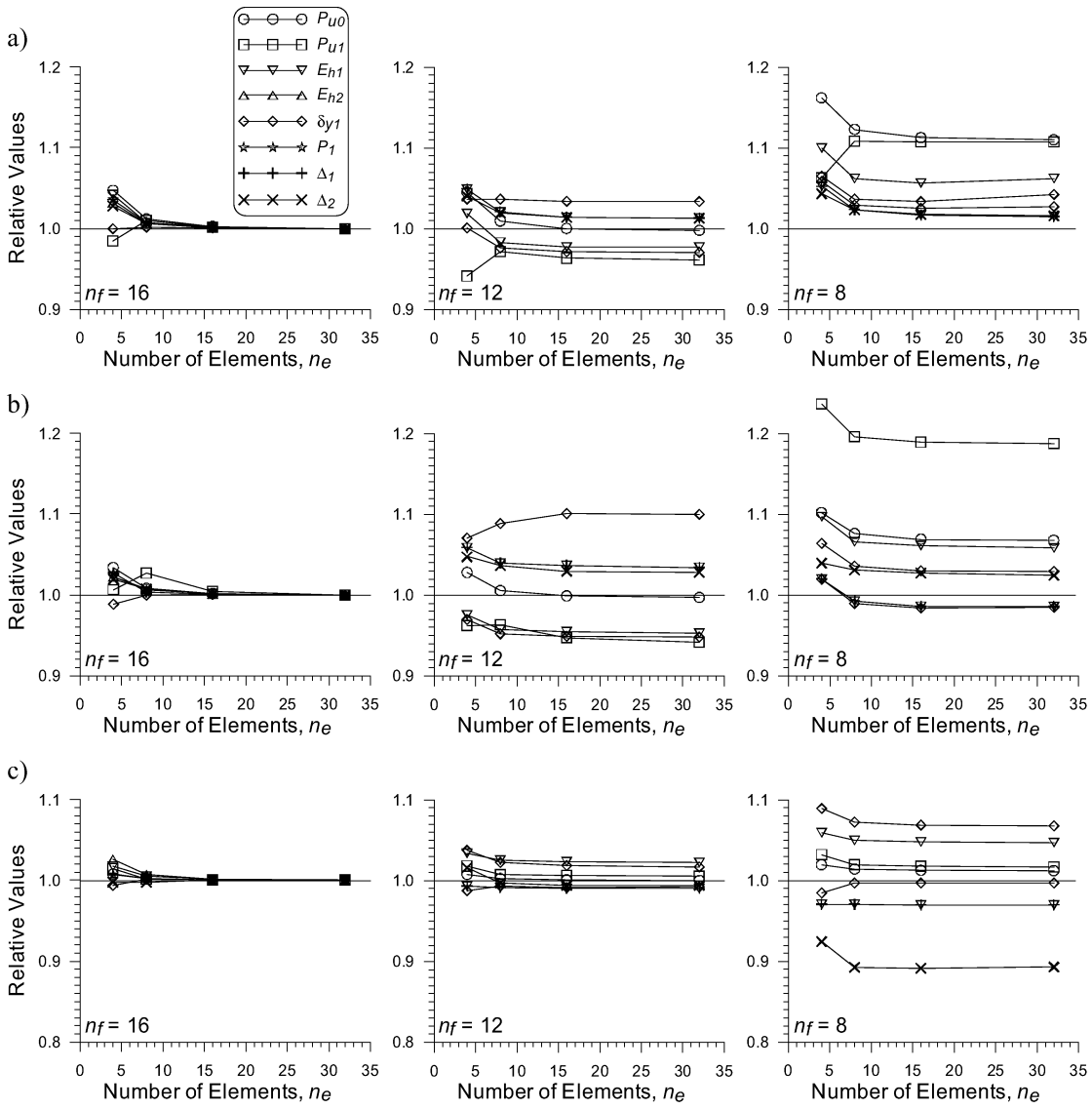

Fig. 6 Agüero et al.

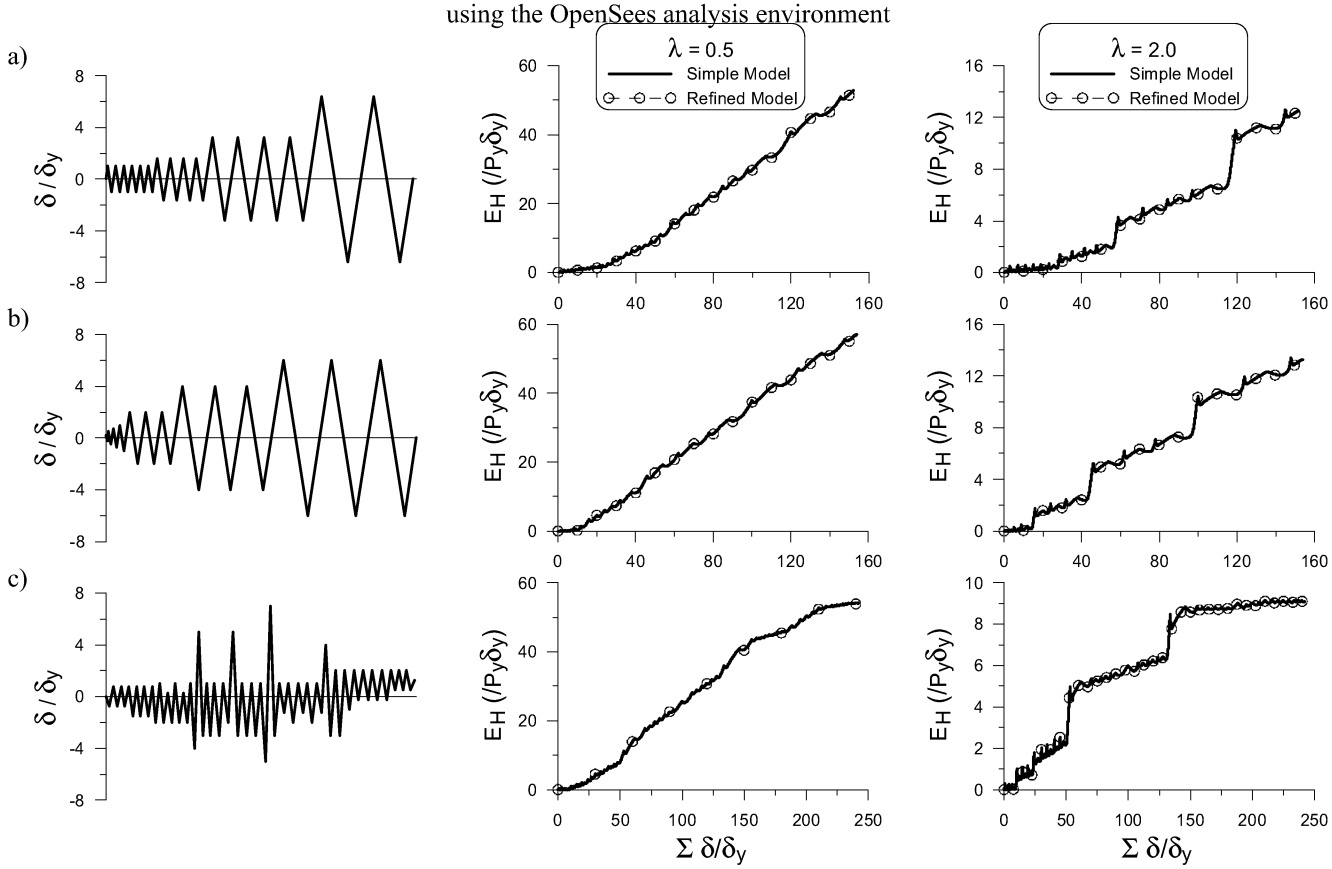

Fig. 7 Agüero et al.

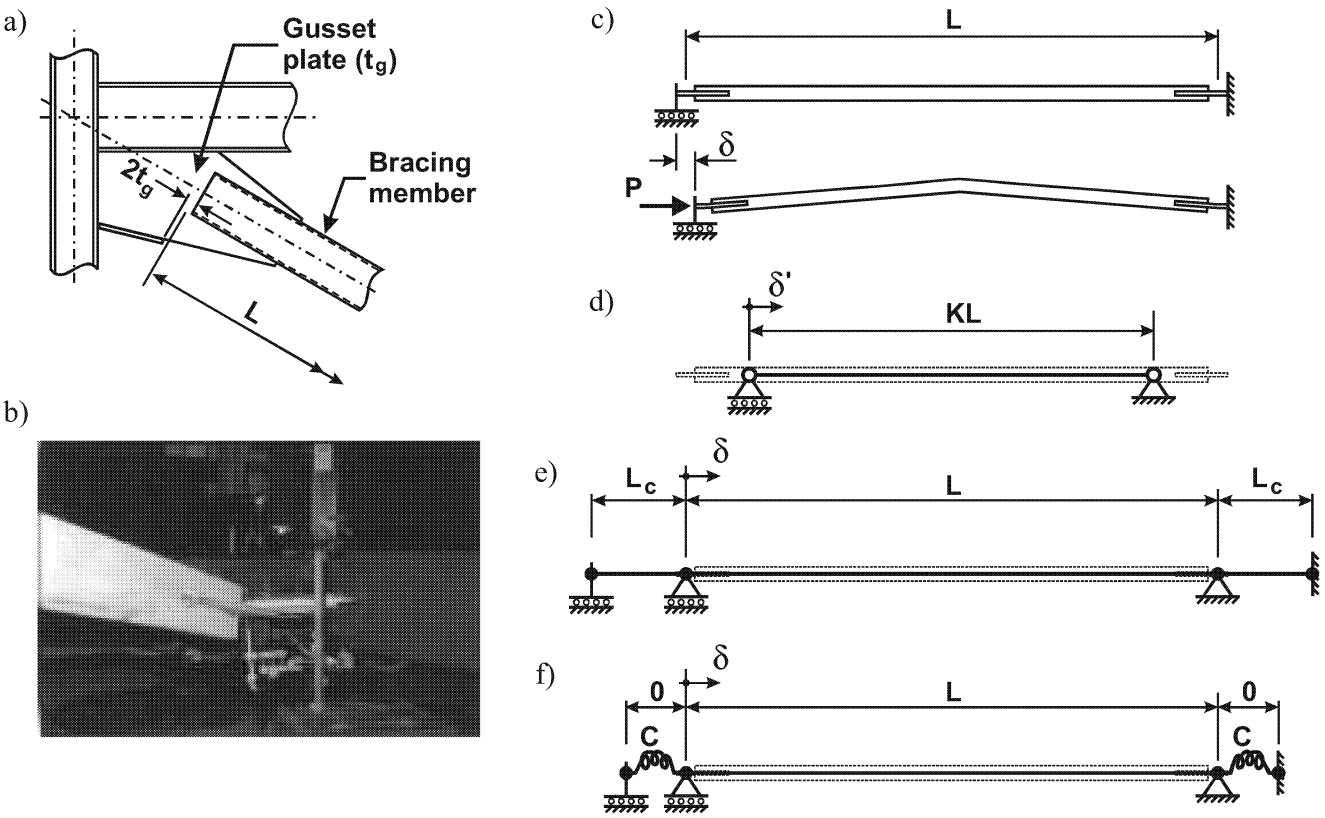

Fig. 8 Agüero et al.

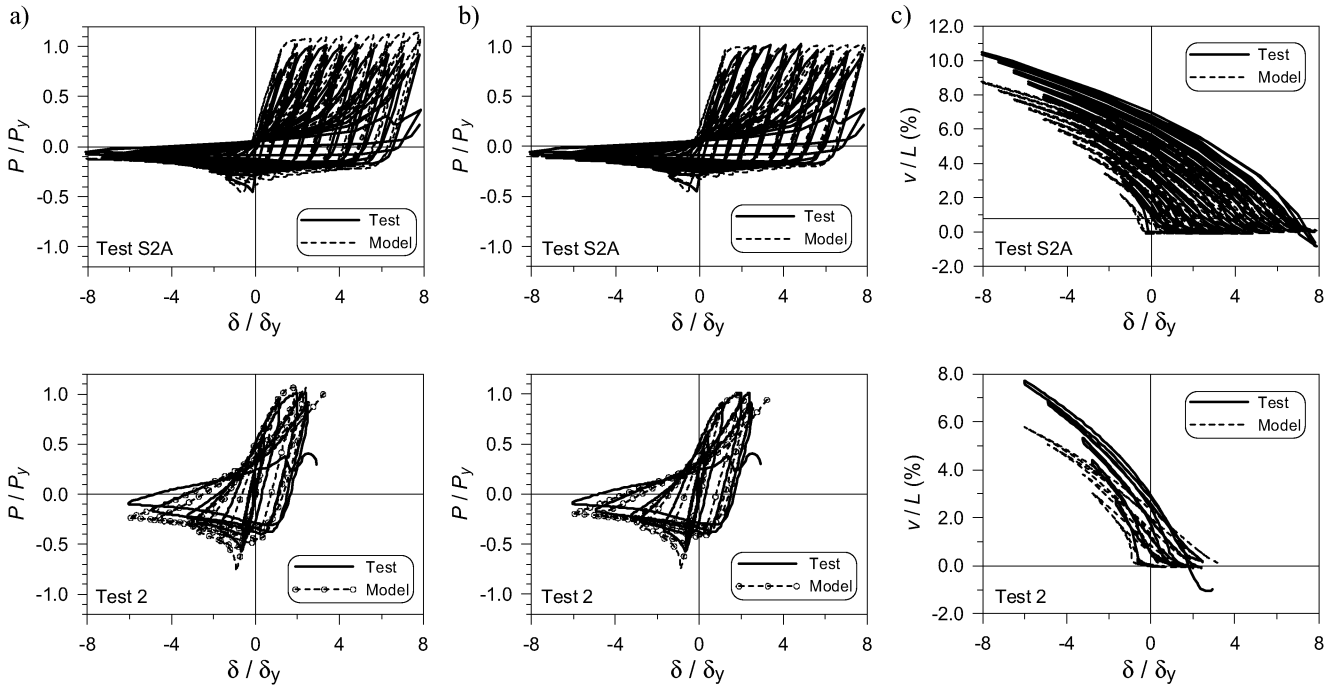

Fig. 9 Agüero et al.

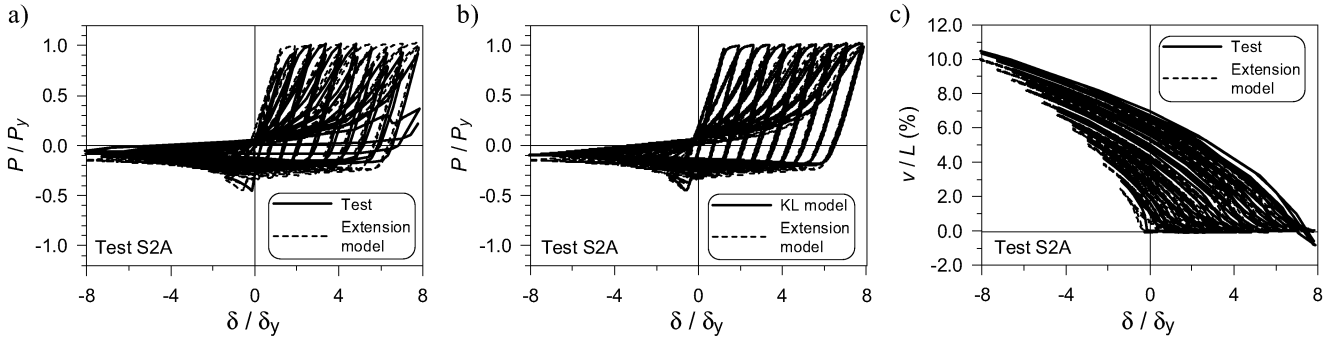

Fig. 10 Agüero et al.

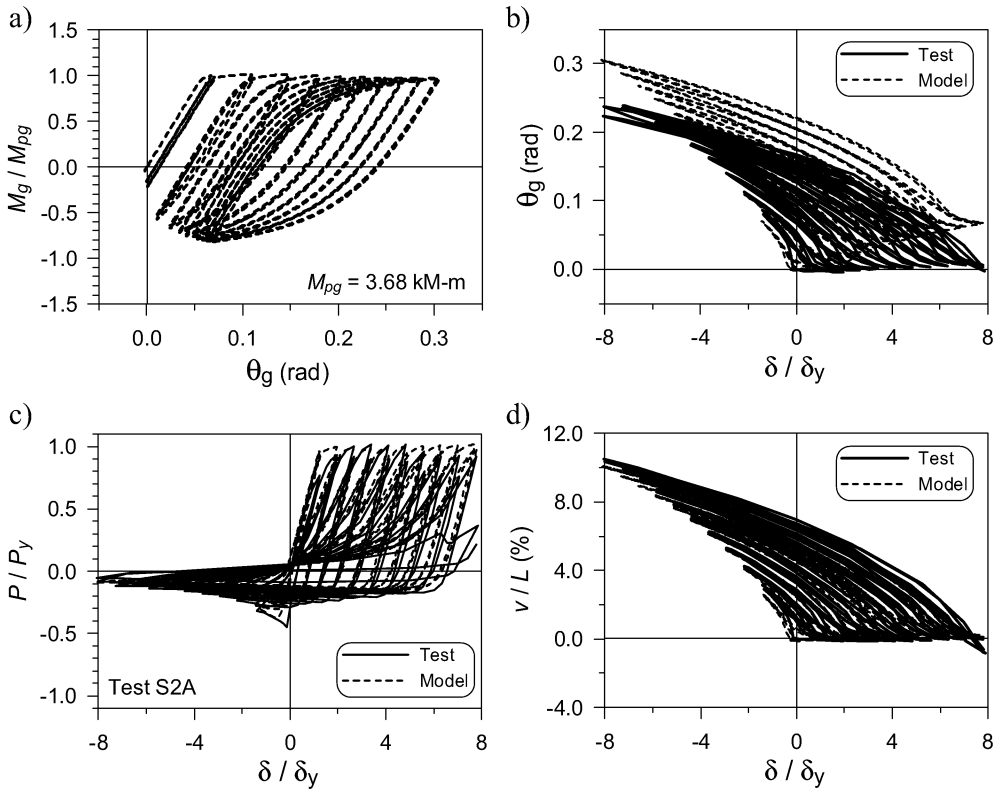

Fig. 11 Agüero et al.

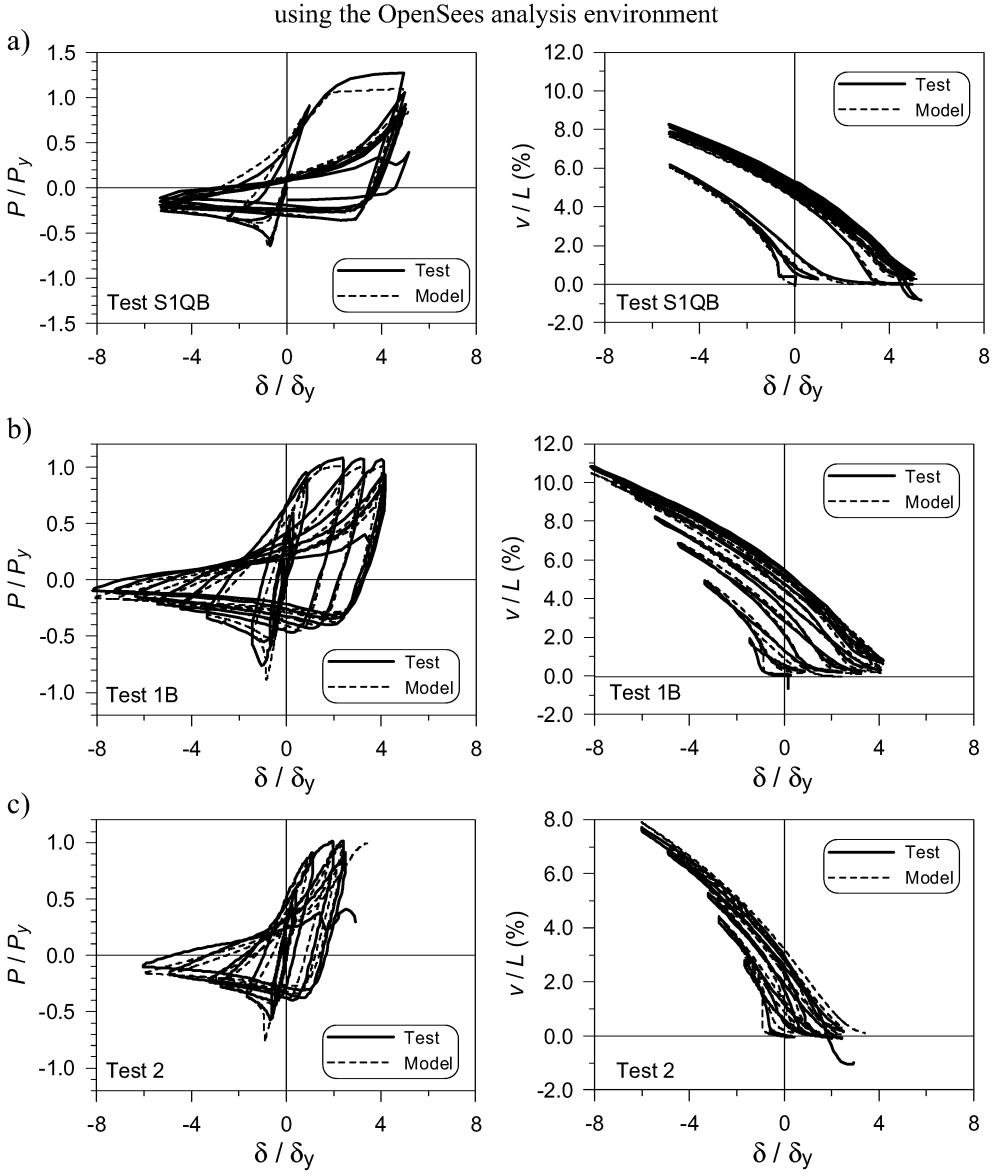

Fig. 12 Agüero et al.

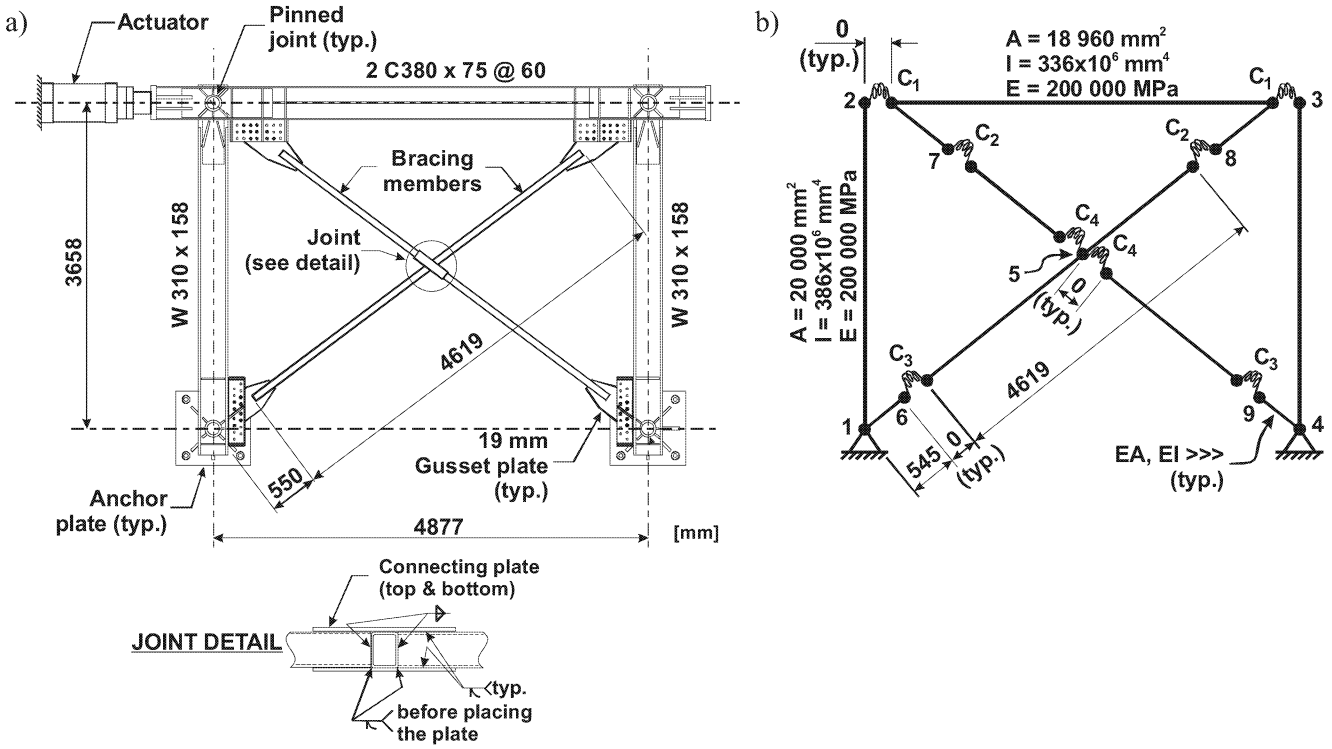

Fig. 13 Agüero et al.

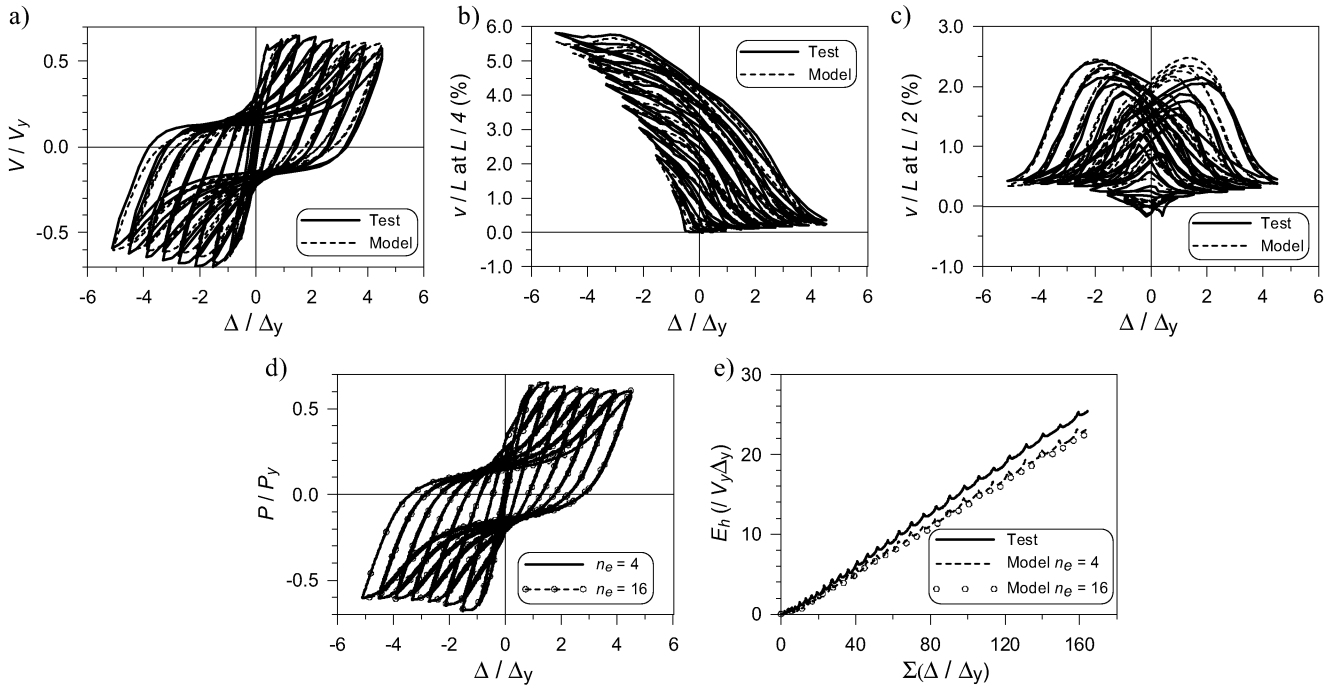

Fig. 14 Agüero et al.

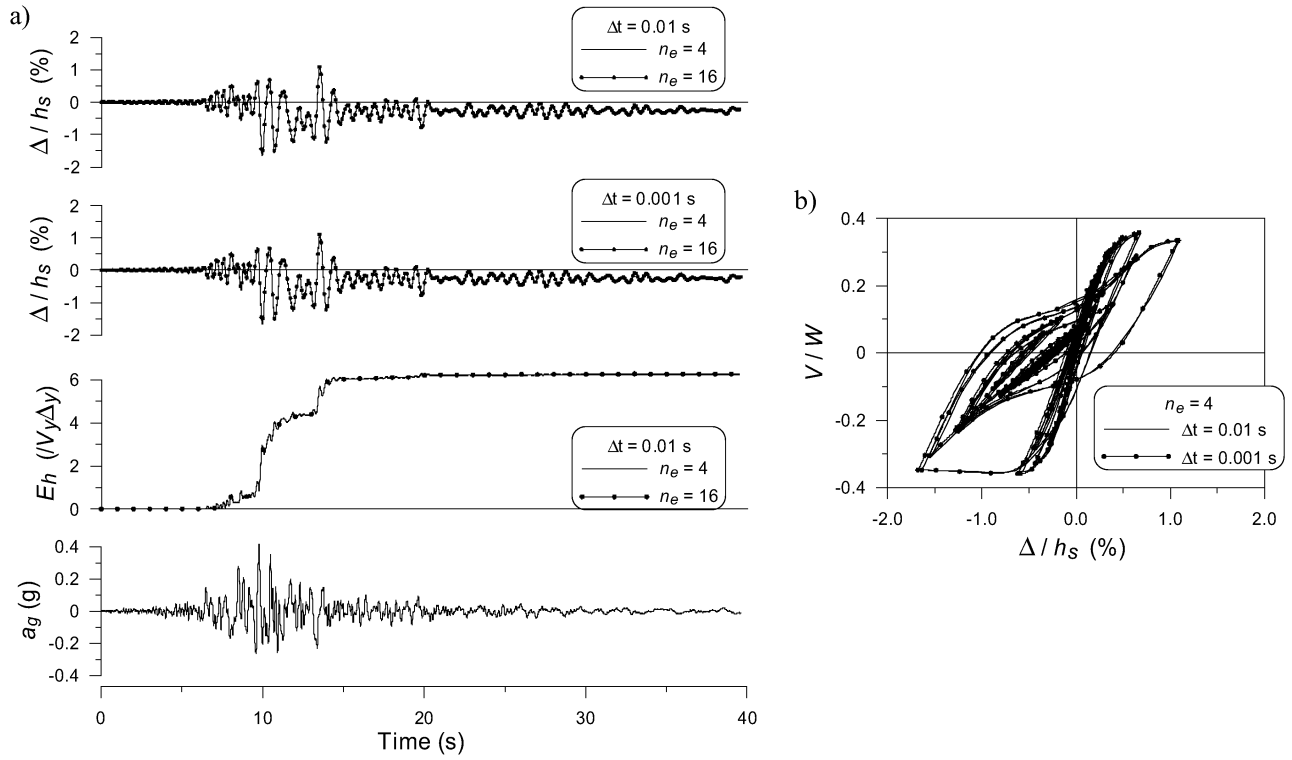

Fig. 15 Agüero et al.

ULTIMATE CAPACITY OF SLENDER STEEL REINFORCED CONCRETE COMPOSITE COLUMNS

G. T. Zhao[1.2], Y. H. Li [1], B. Li [2], G. Xue[2], Z. Han[2] and F. B. Cao[2]

[1]*Department of Civil Engineering, Shanghai University. Shanghai, 200072, China*
[2]*School of Architecture & Civil Engineering, Inner Mongolia University of Science & Technology. Baotou, Inner Mongolia, 014010, China*

ABSTRACT: An experimental study on the behavior of steel reinforced concrete columns and results of a nonlinear numerical analysis are presented. Eight slender steel reinforced concrete composite columns with rectangular section were tested under axial and eccentric loading conditions. Details of the experimental investigation including description of the test columns, testing arrangements, failure modes and mechanism, strain characteristics, load-deformation responses were put forward. Effects of various geometric and material parameters such as concrete strength, slenderness of columns and eccentricity of the applied axial load were studied. The load bearing capacity is reduced with increased slenderness ratio and eccentricity. Significant gains in load capacity are obtained with increased concrete strength for column subjected to axial load, but the capacity is not strongly influenced by the strength of concrete for column subjected to eccentric load. Then this paper presents a numerical method for the analysis of pin–ended slender columns, producing axial force or axial force combined with symmetrical single-curvature bending. This method is applicable for determining the material failure load or buckling failure load of a slender steel reinforced concrete composite column. In this method both material and geometric nonlinearities are taken into account. The results of numerical analysis by proposed method correlate well with the results of the tests.

Keywords: Steel reinforced concrete, Slender column, Capacity, Test, Nonlinear analysis

INTRODUCTION

Steel reinforced concrete （SRC）structures have become a very practical and effective structural system for high rise buildings all over the world ,especially in earthquake area .They provide the required stiffness to limit the story drift of the building to an acceptable limit of lateral displacement, to resist the lateral seismic and wind loads very effectively. The introduction of shaped steel has made it possible to design more slender columns. However, although they can reduce column size, the columns become less ductile due to the brittleness of high-strength concrete. Furthermore, the capacity of slender column is strongly influenced by the second order displacement. Therefore, the structural performance of slender steel reinforced concrete composite columns have recently become a major concern for design engineers.

Many aspects, such as effect of slenderness, amount of shaped steel, ductility, compressive axial force ratio, and eccentricity of the applied load, have to be investigated in order to better understand the structural behavior of the columns. Some researchers, for example Morino et al.(1984), Mirza and Skrabek (1991), Lakshmi and Shanmugam (2000), have studied short steel reinforced concrete composite columns of normal and high-strength concrete subject to axial load. Only a few have studied full-scale composite columns under eccentrically applied axial loading, for example Mirza and Tikka (1999), Mirza and Lacroix (2003). However, the behavior of slender steel reinforced concrete composite columns is not yet fully understood.

ACI318-95 and Chinese standard JGJ138-2001 (Technical specification for steel reinforced concrete composite structures) permit a moment magnifier approach for design of slender

composite columns. This approach is strongly influenced by the effective flexural stiffness of the column that varies due to cracking, creep, nonlinearity of the concrete stress-strain curve, slenderness of column, and eccentricity of the applied axial load. This is expected because the ACI and JGJ138 equations were developed for reinforced concrete columns subjected to high axial loads but were modified, without any further investigation, for use in steel reinforced concrete column designs. So this paper describes experimental and theoretical investigations on the behavior of 8 slender steel reinforced concrete composite columns under axial and eccentric loading conditions. Details of the experimental investigation including description of the test columns, testing arrangements, failure modes and mechanism, strain characteristics, load-deformation responses and effects of various geometric and material parameters are presented. In this study, the three parameters varied were the concrete strength, slenderness of columns and eccentricity of the applied axial load. Then this paper presents a numerical method for the analysis of pin–ended slender columns, producing axial force or axial force combined with symmetrical single-curvature bending; this method is applicable for determining the material failure load or buckling failure load of a slender steel reinforced concrete composite column. In the method, both material and geometric nonlinearties are taken into account. In addition, the mechanical properties, such as the compressive concrete and steel strength, the modulus of elasticity, were measured in the experimental investigation. These material properties were incorporated into a model in which the material model for concrete was based on nonlinear fracture mechanics. This model was, in turn, used in a nonlinear numerical program in order to predict the responses of the slender concrete columns. Observations of the failure mechanisms during the tests and the results of the analysis, as well as some reasons for the failure of the columns under axial and eccentric compressive loading, are presented. The predicted failure loads correlate well with the experimental values.

EXPERIMENTAL PROGRAM

Geometry and Configuration

The objectives of the studies were to research the structural behavior of long, slender steel reinforced concrete composite columns subjected axial and eccentric axial loading. The test series consisted of 8 slender columns, with compressive cube (150mm) strength of concrete from 43.3Mpa to 67.0Mpa, and steel shape I10 encased in concrete. The geometric properties of steel shape were shown in Fig.1. The lengths of the columns were 2.8m, 3.2m, 3.5m, or 4.1m, with rectangular cross sections as shown in Fig.2. The thickness of the concrete cover, measured to the outer edge of the stirrup, was 15mm, and measured to the outer edge of the shaped steel flange, was 40mm, for all of the columns. The stirrup spacing was 150 mm; its diameter was 6 mm. The longitudinal reinforcing bar's diameter was 12 mm. The length-to-width ratios, defined as the ratio of the column length, L, to the cross-section dimension, b (applied axial load), or h (subjected eccentric axial loading), were 18, 22 or 26. The eccentricity of applied loading was from 0 to 60mm.The parameters varied in the tests reported here were the concrete strength, eccentricity, and the slenderness of the columns. Table 1 shows the parameters of the test columns.

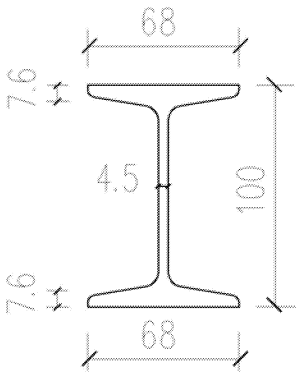

Fig.1 Geometric properties of steel shape

Material properties

The concrete mixes, designed with a target compressive cube (150mm) strength of 40Mpa, 50Mpa or 60Mpa, were produced at the structural engineering laboratory at Inner Mongolia University of Science and Technology. Superplasticizer was used in the concrete mixes to obtain high strength and work ability. The strengths of hardened concrete at 28 days are given in Table 1. The test series consisted of 8 slender columns, with compressive cube (150mm) strength of concrete from 43.3Mpa to 67.0Mpa. The column specimens were cast horizontally in steel forms. The concrete was thoroughly vibrated by means of an internal vibrator. The columns were demolded after approximately seven days and cured under laboratory conditions until tested. The mechanical properties of the shaped steel and longitudinal reinforcement bar are presented in Table 2.

TABLE 1
Details of test columns

No.	Section dimension h×b(mm)	Concrete strength f_{cu}(MPa)	Eccentricity (mm)	Length (mm)	Structural steel ratio %	Ratio of length to width
A1	180×160	65.6	0	2800	5	18
A2	180×160	59.8	0	2800	5	18
A3	180×160	55.7	0	3500	5	22
A4	180×160	50.7	0	3500	5	22
A5	180×160	53.8	0	4100	5	26
A6	180×160	67.0	0	4100	5	26
E1	180×160	43.3	30	3200	5	18
E2	180×160	46.6	40	3200	5	18

TABLE 2
Mechanical properties of structural steel and reinforcement bar

Type	$f_y(MPa)$	$f_u(MPa)$	E(Mpa)
Structural steel	379	507	2.058×10^5
Reinforcement bar	358	471	2.24×10^5

Test setup

The columns were hinged at the ends and were applied with a concentric or an eccentric axial load at both ends. A curved plate of steel and a steel circular bar formed the hinge. The buckling length of the simply supported column is the distance between the bearings at each support. All of the tests were carried out in a universal testing machine with a capacity of 5000KN. The load, which was determined by measurements from a calibrated oil pressure gauge, was increased at a constant rate without interruption. When the load approached the calculated maximum load, the oil pressure gauge was used to indicate how the deformation should be increased in order to capture the post-peak curve.

The deflection in the bending direction was measured by displacement gauge at five locations in

order to determine the deflected shape of the column (Fig.3). Another dial gauge was used to check for possible biaxial bending in the perpendicular direction. The vertical displacement of the lower movable plate of the column-testing machine was measured in relation to the laboratory floor by a displacement transducer. For each specimen, 60-mm-long strain gauges were attached to the concrete on each side of the column at mid-height, 6-mm-long strain gauges were attached to reinforcement bars and each flange or web of the shaped steel at mid-height. To ensure that the failure would occur in the instrumented region of the columns, the ends of the test specimens were further confined with stirrups spaced apart 50 mm.

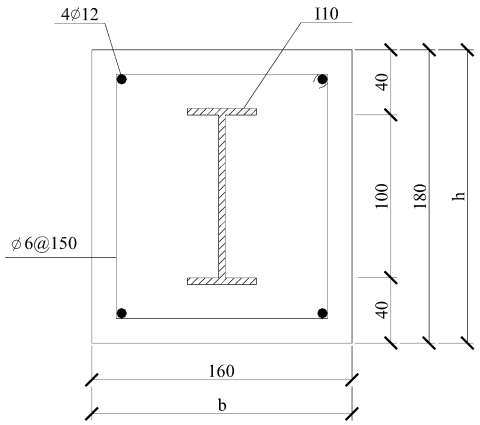

Fig. 2. Geometry and Details of Configurations

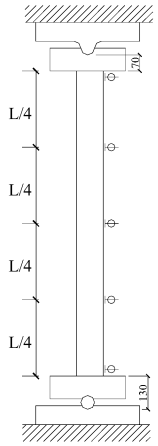

Fig.3. Test setting

Test results

All concentrically loaded columns failed due to spalling of the concrete cover at the mid-height for test specimens ; spalling of concrete cover and tensile cracks were not observed until reaching the maximum load. The columns exhibited a rather sudden and explosive type of failure, especially for columns with a length-to-width ratio of 26. For the columns subjected to an eccentric load, tensile cracks were observed at about 90% the maximum load. The failure is due to concrete spalling at the mid-height. The column failure location was within 500mm from the column mid-height. Furthermore, horizontal bending cracks developed on the tension face. On the compressed side, vertical cracks extending about 2.5 times the column width were observed at maximum load. The loss of the protecting cover combined with a high load level finally led to buckling of the flange of steel shape at the end of the test（Fig.4）

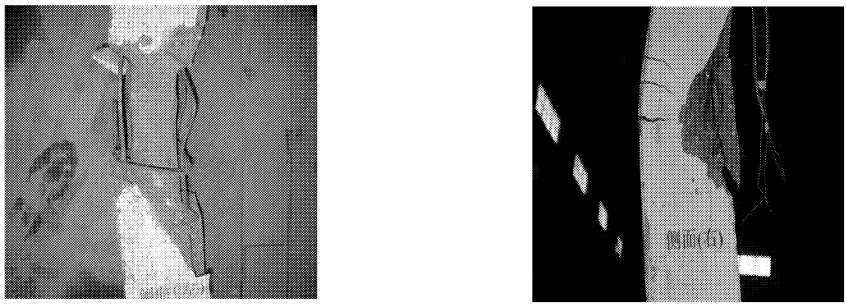

Fig.4. Buckling of the flange of steel shape and crack of column

In Fig.5, the measured load versus mid-height deflection relations are shown. In the ascending branches, the mid-height deflection of the columns were linearly increasing with load until reaching 90% of the maximum load. When the load is about 90% of the maximum load, the mid-height deflections increased rapidly. This implies that the flexural stiffness of columns started to be reduced. The load-carrying capacities was decreased with an increase of the slenderness. As can be observed from the Figure 5, the load-deflection curves are approximately the same for columns with same slenderness ratio at the initial stage.

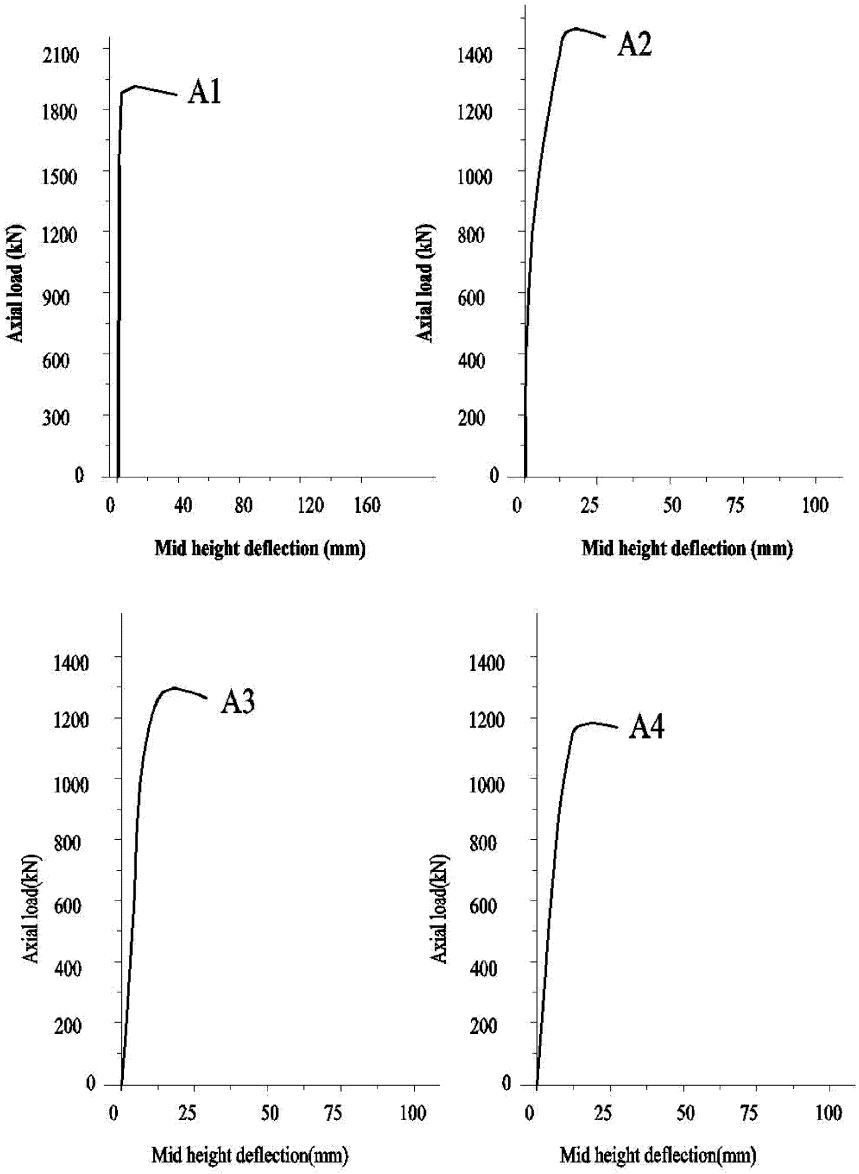

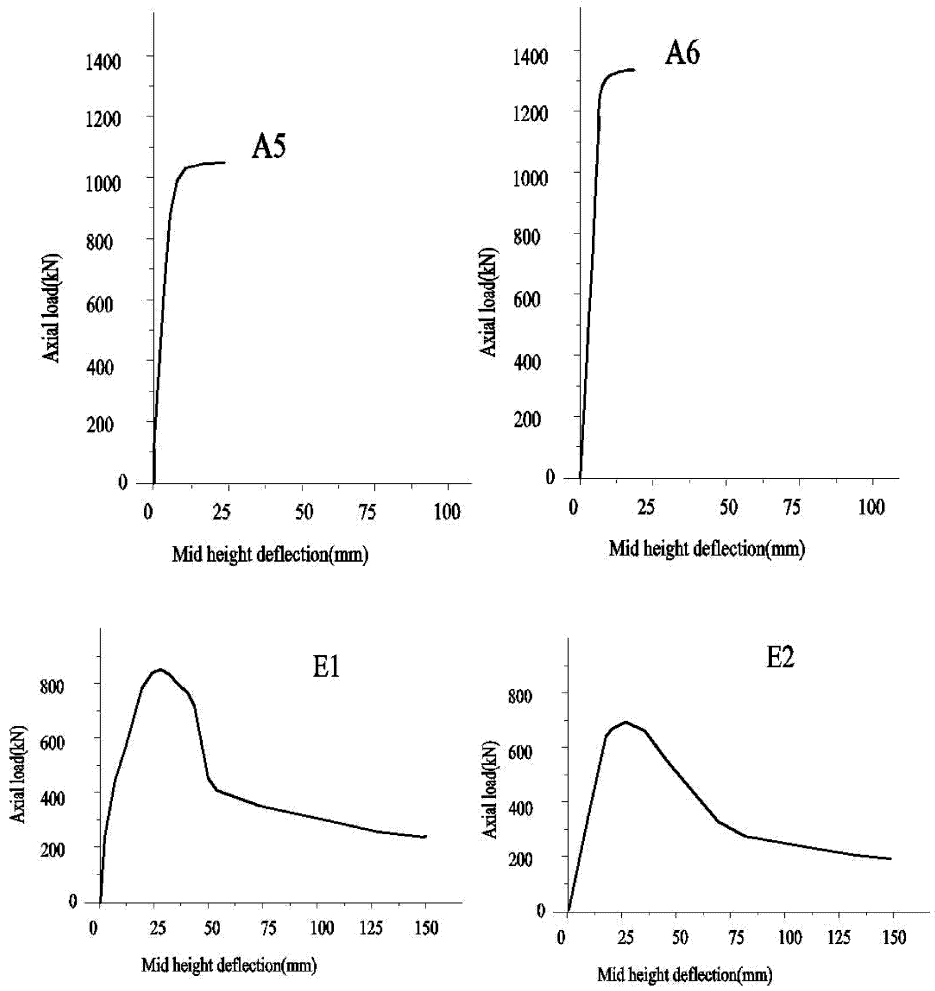

Fig. 5. The measured load versus mid-height deflection relation

Numerical Analysis of the composite columns

For computations of strength, the following assumptions were used: (1) the strain in the cross section was proportional to the distance from the neutral axis, (2) there was no slip between the structural steel or reinforcing bars and the surrounding concrete, (3) the concrete and steel stresses were calculated as functions of the strains, (4) the effects of residual stresses in structural steel section(Fig. 6) were included, (5) the concrete confinement provided by lateral ties and structural steel section flanges was considered. The composite steel-concrete cross section was assumed to consist of four different materials, each represented by a different stress-strain curve. These materials include the unconfined concrete outside the transverse tie reinforcement, the partially confined concrete with the transverse ties, the longitudinal reinforcement, and the structural steel section as indicated in Fig .7.

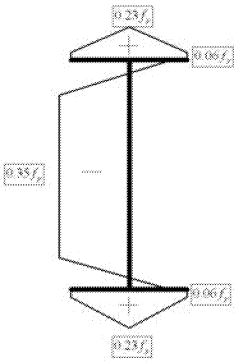

Fig.6. Residual stresses in structural steel section

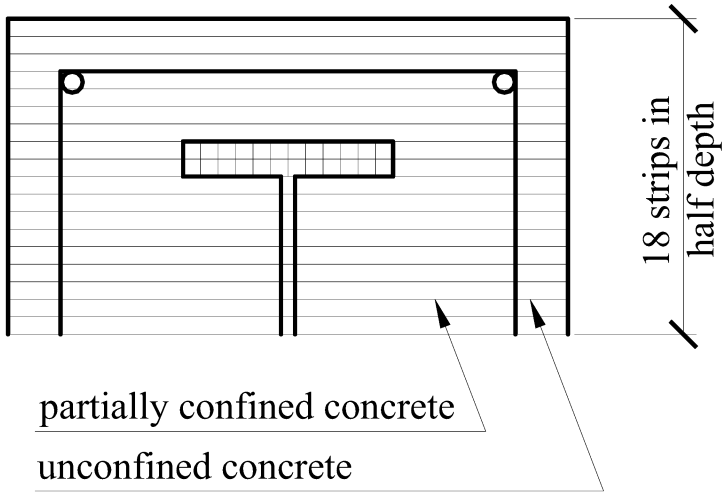

Fig. 7. Discretization of composite one-half cross section for computing strength

Fig. 8. Modeling of a composite column

The modeling of a composite steel-concrete column subjected to symmetrical single curvature bending is illustrated in Fig.8. For the purpose of analysis, the symmetry about the mid-length permitted the use of an equivalent column that was one-half the length of the original column. A column was loaded by introducing a small-applied axial load and a small bending moment at the top node, reflecting the end eccentricity used in the physical test of the column specimen. The applied axial load and bending moment were then increased in increments of constant proportions, using a second-order analysis procedure, until failure occurred. For the analysis of columns subjected to pure axial load, an imperfection was added to the initially straight element model in order to ensure a smooth transition from column stability to column instability.

The failure strength of a column was defined as the peak strength reached on the load-deflection response curve when the column was subjected to pure axial force or axial force combined with bending moment. Thus, this analysis can be applied to short up to very long steel reinforced concrete composite columns, which may fail in material failure or buckling failure.

The elastic-perfectly plastic stress-strain curves defined by measured values of yield strength and modulus of elasticity were used for structural steel section and reinforcing steel bars. The descriptions of both the unconfined and the partially confined concretes in compression outside and inside the lateral ties, respectively, were taken from Park et al (1982).

Analysis and discussion of results

The analytical method described above was applied to investigate the behavior of pin-ended rectangular slender steel reinforced concrete composite columns; the different ratios of length-to-depth, concrete strengths, and eccentricities of applied loading were analyzed. The analytical values are compared with the corresponding experimental results in order to assess the accuracy of the proposed method.

Comparisons of tested and computed strength

The tested strengths and the calculate strengths by non-linear analysis method are presented in Table 3. A comparison of tested and computed response is shown in Fig.9. The calculated values in all cases are close to the corresponding experimental results. The mean value of the ratio of experimental load P_{test} to calculated load P_{calc} is 1.13, it's standard deviation is 0.05. Therefore it can be concluded that the proposed method provides an accurate solution.

TABLE 3

Comparison of tested and computed strengths

No.	A1	A2	A3	A4	A5	A6	E1	E2
$P_{test}(kN)$	1900	1457	1270	1183	1040	1330	820	678
$P_{calc}(kN)$	1633	1341	1067	993	863	1233	739	647
P_{test}/P_{calc}	1.16	1.09	1.19	1.19	1.20	1.08	1.11	1.05

Load-deflection response

To enable a comparative study of the influence of different eccentricity ratios, length-to-depth ratios and concrete strengths on columns behavior, three different eccentricity ratios, length-to-depth ratios and concrete strengths were chosen. Fig .10(a) presents the relation between axial and mid height deformation obtained by

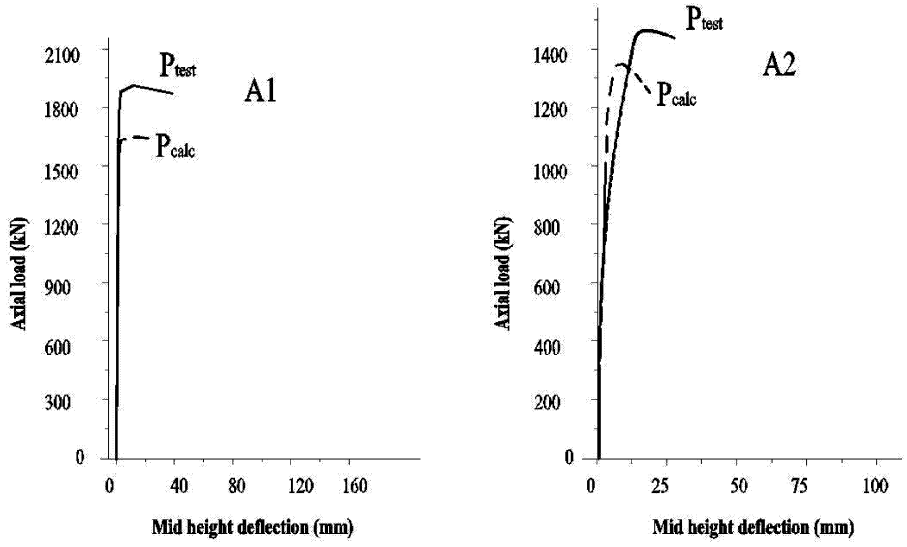

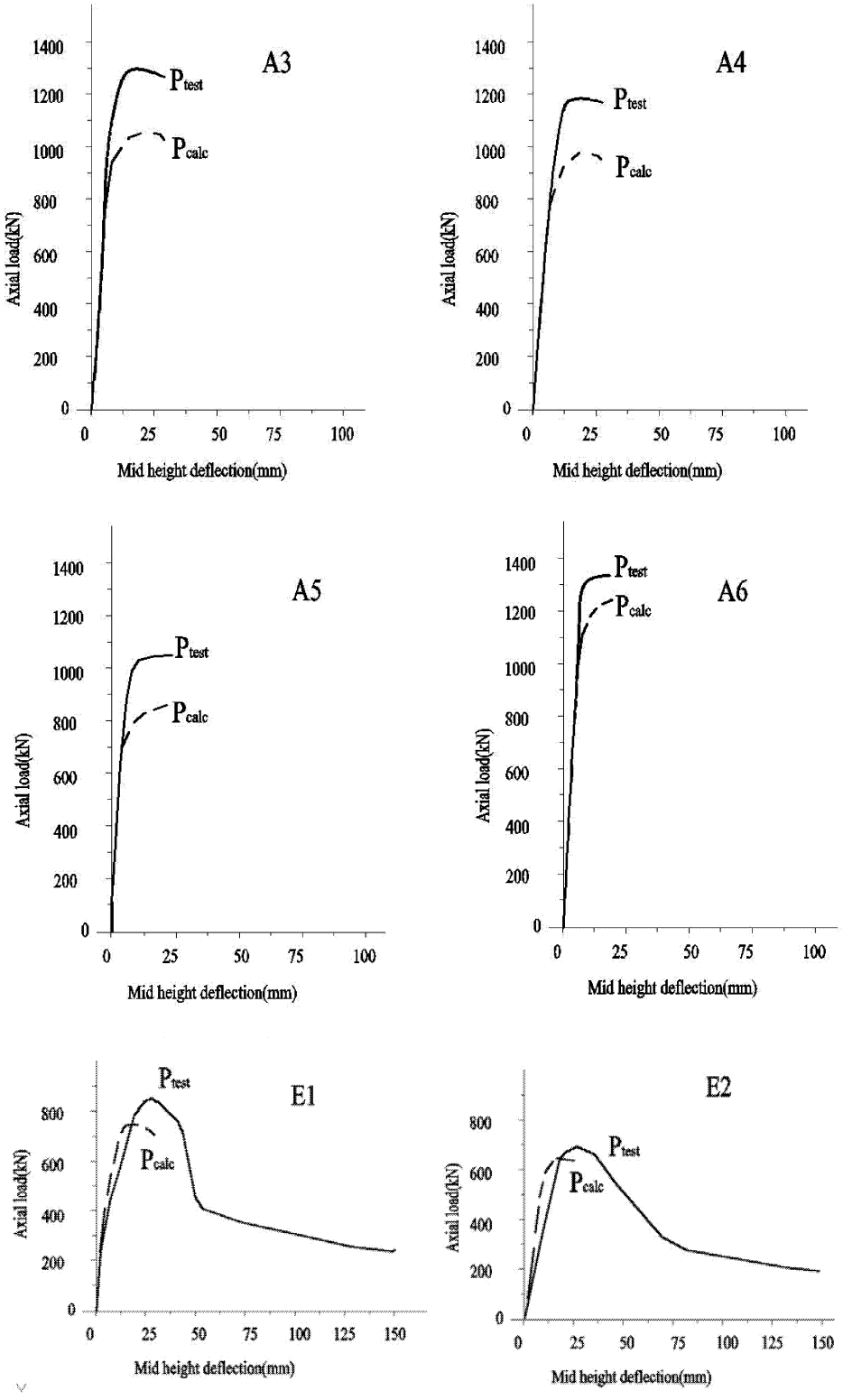

Fig. 9. Comparison of tested and computed relation of axial and mid height deformation

the proposed analytical method for the columns subjected to different initial load eccentricities, the eccentricity varies from e/h=0.1 to 0.3 about the major axis. These columns of length 3.6m pinned at the ends are subjected to single curvature bending. It is clear that column capacity is strongly affected by the amount of eccentricity. Fig.10 (b) shows the results of the simulations for three length-to-depth ratios columns subjected to an initial eccentricity of 18mm. When the

length-to-depth ratio increases, the load bearing capacity is decreased. Fig.10(c) shows the relations between the load and the mid-height deflection for three different concrete strength columns subjected to an initial eccentricity of 18mm. The advantage of using a higher compressive concrete strength is not obvious. Comprehensive parametric studies show that the two main parameters that influenced the force-deflection response are column slenderness and eccentricity of the applied load. It can be seen from the Figure 5 that the load-deflection response remains very stiff even up to the ultimate load in the case of columns subjected to axial load. As the eccentricity increases the load-carrying capacity drops significantly and the initially stiffness decreases.

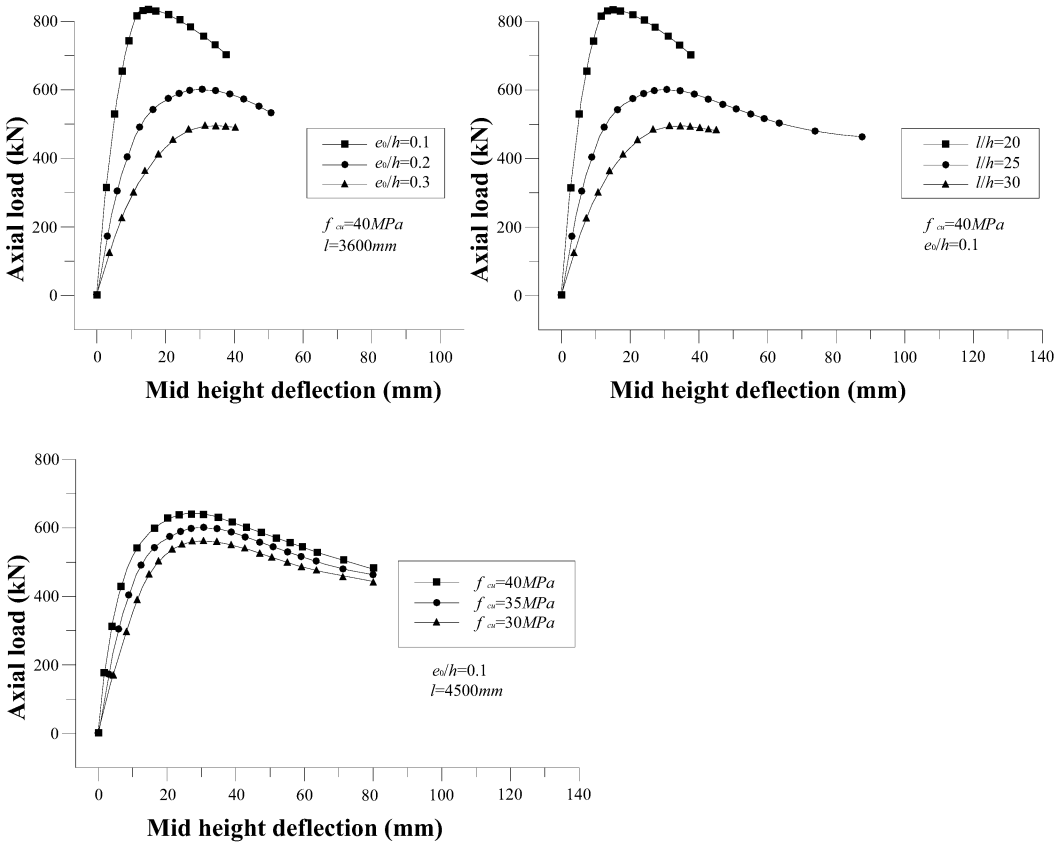

Fig.10. Computed relation of axial and mid height deflection

Conclusions

The influence of different eccentricity ratios, length-to-width ratios and concrete strengths on slender steel reinforced concrete column strength was studied. The results of tests and the numerical analysis on the columns presented here allow the following conclusions to be drawned. The buckling capacity is reduced with the slenderness ratio increase. For the eccentrically loaded columns, load carrying capacity is found to drop significantly with an increase of eccentricity, but that is not strongly influenced by the concrete strength. For column subjected to axial load, the buckling capacity is increased with an increase of concrete strength. An analytical method to compute the ultimate strength of slender steel reinforced concrete composite columns has been proposed. Comparison of ultimate strength, which was obtained by using the proposed method with the corresponding experimental results for column, has proven the accuracy of the described method.

ACKNOWLEDGMENTS

Financial support for this research was provided by Natural Science Foundation of Inner Mongolia, China (Grant No.20020802-0212).

REFERENCE

[1] ACI committee 318, "Building code requirements for structural concrete (ACI 318-95) and commentary (ACI 318R-95)," American Concrete Institute, Farmington Hills, Mich, 1995, PP.369.
[2] China standard, "Technical specification for steel reinforced concrete composite structures(JGJ138-2001)", China Architecture & Building Press, Beijing ,2002, PP. 29.
[3] Morino, S., Matsui, C. and Watanabe, H., "Strength of biaxial loaded SRC columns." Composite and Mixed Construction, ASCE, New York, 1984, PP. 241-253.
[4] Mirza, S. A. and Skrabek, B.W., "Reliability of short composite beam-column strength interaction." Journal of Structural Engineering ASCE, No.8, Aug. 1991, PP. 2320-2334.
[5] Lakshmi, B. and shanmugam, N. E., (2000), "Behavior of steel-concrete composite columns", Pro. 6th ASCCS Int. Conf. on Steel and Concrete Composite Structures, Association for International Cooperation and Research in Steel-Concrete Composite Structures (ASCCS), Los Angeles, PP. 449-456.
[6] Mirza, S. A. and Tikka, T. K.,(1999), "Flexural stiffness of composite columns subjected to major axial bending", ACI Structural Journal, V.96, No.1 January-February, 1999, PP. 19-28.
[7] Mirza, S. A. and Lacroix, E. A., (2003), "Finite element analysis of composite steel-concrete columns", Symposium on The Art and Science of Structural Concrete Design, 2003, PP. 185-205.
[8] Park, R., Priestley, M. J. N. and Gill, W. D.,(1982), "Ductility of square confined concrete columns", Journal of the Structural Division, ASCE, V.108,No.ST4, PP. 929-950.
[9] Wang, Y. C., (1999), "Tests on slender composite columns", Journal of Construction Steel Research, 49, PP. 25-41.

Gentian Zhao, is a professor of civil engineering at Inner Mongolia University of Science & Technology and Shanghai University, China. He specializes in research of steel structures and composite steel-concrete structures. E-mail address:zhaogt@tom.com

Address: School of Architecture & Civil Engineering,
Inner Mongolia University of Science & Technology.
Baotou, Inner Mongolia, 014010, China
Tel: 0086-472-2140842
Fax: 0086-472-2134843
Email: zhaogt@tom.com